

DOMAIN-BOUNDARY ELEMENT METHOD FOR ELASTODYNAMICS OF
FUNCTIONALLY GRADED THICK-WALLED CYLINDERS AND ANNULAR
COATINGS

A THESIS SUBMITTED TO
THE GRADUATE SCHOOL OF NATURAL AND APPLIED SCIENCES
OF
MIDDLE EAST TECHNICAL UNIVERSITY

BY

ABDELRAHIM ABEIDI

IN PARTIAL FULFILLMENT OF THE REQUIREMENTS
FOR
THE DEGREE OF DOCTOR OF PHILOSOPHY
IN
MECHANICAL ENGINEERING

DECEMBER 2022

Approval of the thesis:

**DOMAIN-BOUNDARY ELEMENT METHOD FOR ELASTODYNAMICS
OF FUNCTIONALLY GRADED THICK-WALLED CYLINDERS AND
ANNULAR COATINGS**

submitted by **Abdelrahim Abeidi** in partial fulfillment of the requirements for the degree of
Doctor of Philosophy in Mechanical Engineering, Middle East Technical University by,

Prof. Dr. Halil Kalıpçılar
Dean, Graduate School of **Natural and Applied Sciences**

Prof. Dr. M. A. Sahir Arıkan
Head of the Department, **Mechanical Engineering**

Prof. Dr. Serkan Dağ
Supervisor, **Mechanical Engineering Dept., METU**

Examining Committee Members:

Prof. Dr. F. Suat Kadioğlu
Mechanical Engineering Dept., METU

Prof. Dr. Serkan Dağ
Mechanical Engineering Dept., METU

Prof. Dr. Recep Güneş
Mechanical Engineering Dept., Erciyes University

Assoc. Prof. Dr. Hüsnü Dal
Mechanical Engineering Dept., METU

Assoc. Prof. Dr. Tunç Apatay
Mechanical Engineering Dept., Gazi University

Date: 16.12.2022

I hereby declare that all information in this document has been obtained and presented in accordance with academic rules and ethical conduct. I also declare that, as required by these rules and conduct, I have fully cited and referenced all material and results that are not original to this work.

Name, Last name : Abdelrahim Abeidi

Signature :

ABSTRACT

DOMAIN-BOUNDARY ELEMENT METHOD FOR ELASTODYNAMICS OF FUNCTIONALLY GRADED THICK-WALLED CYLINDERS AND ANNULAR COATINGS

Abeidi, Abdelrahim
Doctor of Philosophy, Mechanical Engineering
Supervisor : Prof. Dr. Serkan Dağ

December 2022, 111 pages

In this thesis, a new computational technique using domain boundary element method (D-BEM) will be developed to perform the elastodynamic analysis of functionally graded thick-walled cylinders and annular coatings. The thick-walled cylinder material properties are varying along the radial direction according to a power distribution law of volume fraction; hence, the cylinder can withstand pressure shock types of loadings. These mechanical loads are described by uniform dynamic pressures at the inner and outer edges. Therefore, the FGM thick-walled cylinder is subjected to axisymmetric external loading in plane strain condition. The domain boundary element method will be implemented to solve the integral equations achieved by using the static fundamental solution to write the governing differential equation in the residual form. However, since the problem is dynamic, time dependent, isoparametric quadrilateral elements will be proposed to discretize the domain. The integral equations will be computed for each element and a system of time dependent ordinary differential equations will result. The time response is obtained by using Houbolt method of time marching scheme to solve the system of ordinary differential equations. Therefore, the proposed D-BEM method is verified by considering various researches, which study the elastodynamics of FGM thick-walled cylinders subjected to different mechanical loadings on the inner surface, such as: mechanical shock and exponential loadings. Furthermore, the FGM thick-walled cylinder elastodynamic response has been studied

using the D-BEM in plane stress and plane strain conditions. An internal and external ramp dynamic pressure and an internal exponential dynamic pressure are considered in the study of the composite thick-walled cylinders and annular coatings. The radial displacement response, radial and hoop stresses are calculated at different material property gradation values. Moreover, for the pressure shock loadings selected, the spatial radial displacement, spatial radial and hoop stresses are studied.

Keywords: Thick-Walled Cylinder, Annular Coatings, FGM, Elastodynamic, D-BEM.

ÖZ

FONKSİYONEL OLARAK DERECELENDİRİLMİŞ KALIN DUVARLI SİLİNDİRLERİN VE DAİRESEL KAPLAMALARIN ELASTODİNAMİK İÇİN ALAN SINIR ELEMAN YÖNETEMİNİ

Abeidi, Abdelrahim
Doktora, Makina Mühendisliği
Tez Yöneticisi: Prof. Dr. Serkan Dağ

Aralık 2022, 111 sayfa

Bu tezde, fonksiyonel olarak derecelendirilmiş kalın duvarlı silindirlerin ve dairesel kaplamaların elastodinamik analizini gerçekleştirmek için alan sınır eleman yöntemini (D-BEM) kullanan yeni bir hesaplama tekniği geliştirilecektir. Kalın duvarlı silindir malzeme özellikleri, hacim fraksiyonunun bir güç dağıtım yasasına göre radyal yön boyunca değişmektedir; dolayısıyla silindir, basınç şoklu yükleme türlerine dayanabilir. Bu mekanik yükler, iç ve dış kenarlardaki üniform dinamik basınçlarla tanımlanır. Bu nedenle, FGM kalın duvarlı silindir, düzlem gerinme durumunda eksenel simetrik dış yüklemeye maruz kalır. Alan sınır eleman yöntemi, ana diferansiyel denklemi artık formda yazmak için statik temel çözüm kullanılarak elde edilen integral denklemleri çözmek için uygulanacaktır. Ancak problem dinamik olduğundan, zamana bağlı olduğundan, alanı ayrıklaştırmak için izoparametrik dörtgen elemanlar önerilecektir. Her eleman için integral denklemler hesaplanacak ve zamana bağlı adi diferansiyel denklemler sistemi ortaya çıkacaktır. Zaman yanıtı, adi diferansiyel denklemler sistemini çözmek için Houbolt zaman yürüyüşü şeması yöntemi kullanılarak elde edilir. Bu nedenle, önerilen D-BEM yöntemi, iç yüzeyde mekanik şok ve üstel yüklemeleri gibi farklı mekanik yüklere maruz kalan FGM kalın duvarlı silindirlerin elastodinamiğini inceleyen çeşitli araştırmalar dikkate alınarak doğrulanmıştır. Ayrıca, FGM kalın duvarlı silindir elastodinamik tepkisi, düzlem gerilme ve düzlem gerinim koşullarında D-BEM kullanılarak incelenmiştir. Kompozit

kalın duvarlı silindirler ve dairesel kaplamaların çalışmasında bir iç ve dış rampa dinamik basıncı ve bir iç üstel dinamik basınç göz önünde bulundurulmuştur. Radyal yer değiştirme tepkisi, radyal ve teğetsel gerilmeleri, farklı malzeme özelliği derecelendirme değerlerinde hesaplanır. Ayrıca, seçilen basınç şoku yükleri için, uzaysal radyal yer değiştirme, uzaysal radyal ve teğetsel gerilmeleri incelenmiştir.

Anahtar Kelimeler: Kalın Duvarlı Silindir, Halka Kaplamalar, FGM, Elastodinamik, D-BEM.

To my wife Aisha, sweetie Sedal and my family

ACKNOWLEDGMENTS

I would like to express my sincere gratitude to my supervisor Prof. Dr. Serkan Dağ for his guidance, patience, assistance and continuous support through the course of my PhD study and research. I would also like to thank my thesis committee: Prof. Dr. Recep Güneş, Assoc. Prof. Dr. Hüsnü Dal, and Assoc. Prof. Dr. Tunç Apatay for their encouragement, insightful comments and suggestions, thank you all.

To all relatives and friends who in one way or another share their support, thank you. A special thanks to my sisters Niruz and Esra and her husband Wakil for their caring and support. I appreciate their effort of coming along the way to attend my thesis jury with my lovely little nephews Hassan and Muhammed.

Finally, to my caring, and supportive wife, Aisha: my deepest gratitude. Your encouragement at the rough times are much appreciated. My heartfelt thanks.

TABLE OF CONTENTS

ABSTRACT	v
ÖZ	vii
ACKNOWLEDGMENTS	x
TABLE OF CONTENTS	xi
LIST OF TABLES	xiii
LIST OF FIGURES	xiv
CHAPTERS	
1. INTRODUCTION	1
1.1 FGM thick-walled cylinders.....	1
1.2 Boundary Element Method	4
1.3 Review of the Literature	7
2. RESEARCH METHODOLOGY	15
2.1 Statement of the Problem	15
2.1.1 Elastodynamic Formulation	16
2.1.1.1 Boundary and Initial Conditions	20
3. D-BEM FORMULATION	21
3.1 Fundamental Solution.....	21
3.2 The Integral Equation	25
3.3 Numerical Procedure	28
3.3.1 Time Marching with the Houbolt Method	37
4. VERIFICATION OF THE METHOD.....	41
4.1 First Comparison	41
4.1.1 Dynamic Loadings	43
4.1.1.1 Ramp Dynamic Loading Results and Comparison	44
4.1.1.2 Exponential Dynamic Loading Results and Comparison.....	48
4.2 Second Comparison.....	49
4.2.1 Formulation of the problem	49
4.2.2 Dynamic loadings.....	51
5. NUMERICAL RESULTS.....	53

5.1	Composite thick-walled cylinder in plane stress condition.	53
5.1.1	Radial displacement response results for plane stress.....	54
5.1.2	Radial and circumferential stresses calculations for plane stress.....	55
5.1.2.1	Radial stress results for plane stress	55
5.1.2.2	Hoop stress results for plane stress	56
5.2	Composite thick-walled cylinder in plane strain condition –First case study	57
5.2.1	Radial displacement response results for plane strain.....	59
5.2.2	Radial and circumferential stresses calculations for plane strain.....	60
5.2.2.1	Radial stress results for plane strain	60
5.2.2.2	Hoop stress results for plane strain	61
5.3	FGM thick-walled cylinder in plane strain condition – Second case study	62
5.3.1	The pressure loading on the inner surface of the cylinder	62
5.3.1.1	Parametric analysis of stress concentration related to circumferential stress	73
5.3.2	The pressure loading on the outer surface of the cylinder	74
5.4	Annular external FGM coating thick-walled cylinder in plane strain condition	79
5.5	Annular internal FGM coating thick-walled cylinder in plane strain condition	86
6.	CONCLUSIONS	95
	REFERENCES.....	99
	APPENDIX	107
	CURRICULUM VITAE	111

LIST OF TABLES

Table 1: Thick-walled cylinder geometry and mechanical properties [24].	42
Table 2: Composite thick-walled cylinder geometry and mechanical properties - plane stress	54
Table 3: Composite thick-walled cylinder geometry and mechanical properties -plane strain.	57
Table 4: $ \sigma_{\theta\theta} _{\max}/\sigma_0$ values for an FGM thick-walled cylinder under internal pressure shock, $r_i = 0.1$ m, $r_o = 0.2$ m, $n_1 = n_2 = n$	73
Table 5: r/r_i values corresponding to largest circumferential stress amplitudes for an FGM thick-walled cylinder under internal pressure shock, $r_i = 0.1$ m, $r_o = 0.2$ m, $n_1 = n_2 = n$	73

LIST OF FIGURES

Figure 1: FGM thick-walled cylinder under pressure shocks.....	16
Figure 2: Two-dimensional element in polar coordinates	17
Figure 3: Dirac delta and Kelvin problem.....	22
Figure 4: Domain and symmetric boundary conditions	28
Figure 5: Domain discretization into quadratic elements	28
Figure 6: Cross-section of the FGM thick-walled cylinder with the boundary conditions. ...	41
Figure 7: The variation of the internal ramp pressure with time proposed.	43
Figure 8: The variation of the internal non-dimensional exponential pressure with non-dimensional time proposed for verification.....	44
Figure 9: Time history of radial displacement at midpoint with $n_1 = n_2 = 0.5$	45
Figure 10: Time history of radial displacement at midpoint with $n_1 = n_2 = 5$	45
Figure 11: Time history of radial displacement at midpoint with $n_1 = 9.29$, $n_2 = 1.86$	46
Figure 12: Time history of radial displacement at midpoint with different material property indices by using D-BEM.	46
Figure 13: Time history of circumferential stress at midpoint with $n_1 = n_2 = 5.0$	47
Figure 14: Time history of non-dimensional radial displacement at midpoint with $n_1 = n_2 = 0.5$	48
Figure 15: Schematic diagram of the boundary conditions and geometry of FGM thick-walled cylinder	49
Figure 16: Comparisons of normalized radial displacements to the results given by Keles and Tütüncü [57] for $\beta = 0$ & 2.0	51
Figure 17: Composite thick-walled hollow cylinder under pressure shock loads	53

Figure 18: Comparison of various time history of radial displacement at different radii with $n_1 = 9.27$ & $n_2 = 1.87$	55
Figure 19: Comparison of radial stress at various points of wall thickness	56
Figure 20: Comparison of hoop stress at various points of wall thickness	56
Figure 21: Comparison of various time history of radial displacement at different radii with $n_1 = 9.27$ & $n_2 = 1.87$	59
Figure 22: Comparison of Radial Stress at Various Points of Wall Thickness.....	60
Figure 23: Comparison of Hoop Stress at Various Points of Wall Thickness.	61
Figure 24: FGM thick-walled hollow cylinder under pressure shock loads	62
Figure 25: Dimensionless radial displacement at the mid-point, $r = (r_i + r_o)/2$, of an FGM cylinder under internal pressure shock.....	63
Figure 26: Dimensionless radial stress at the mid-point, $r = (r_i + r_o)/2$, of an FGM cylinder under internal pressure shock.....	64
Figure 27: Dimensionless tangential stress at the mid-point, $r = (r_i + r_o)/2$, of an FGM cylinder under internal pressure shock.....	64
Figure 28: Dimensionless radial displacement at point, $r_c = r_i + (r_o - r_i)/10$. of an FGM cylinder under internal pressure shock.....	65
Figure 29: Dimensionless radial stress at point, $r_c = r_i + (r_o - r_i)/10$. of an FGM cylinder under internal pressure shock.....	66
Figure 30: Dimensionless tangential stress at point, $r_c = r_i + (r_o - r_i)/10$. of an FGM cylinder under internal pressure shock.....	66
Figure 31: Dimensionless radial displacement response at different r_o/r_i for an FGM cylinder under internal pressure shock at $n_1 = n_2 = -1$	67
Figure 32: Dimensionless radial stress response at different r_o/r_i for an FGM cylinder under internal pressure shock at $n_1 = n_2 = -1$	68
Figure 33: Dimensionless tangential stress response at different r_o/r_i for an FGM cylinder under internal pressure shock at $n_1 = n_2 = -1$	68

Figure 34: Dimensionless radial displacement response at different r_o/r_i for an FGM cylinder under internal pressure shock at $n1 = n2 = 0.5$.	69
Figure 35: Dimensionless radial stress response at different r_o/r_i for an FGM cylinder under internal pressure shock at $n1 = n2 = 0.5$.	70
Figure 36: : Dimensionless tangential stress response at different r_o/r_i for an FGM cylinder under internal pressure shock at $n1 = n2 = 0.5$.	70
Figure 37: Dimensionless spatial radial displacement computed at $t = t_0 = 0.005$ s considering an FGM cylinder under internal pressure shock.	71
Figure 38: Dimensionless spatial radial stress computed at $t = t_0 = 0.005$ s considering an FGM cylinder under internal pressure shock.	72
Figure 39: Dimensionless spatial tangential stress computed at $t = t_0 = 0.005$ s considering an FGM cylinder under internal pressure shock.	72
Figure 40: Dimensionless radial displacement at the mid-point, $r = (r_i + r_o)/2$, of a FGM cylinder under external pressure shock.	75
Figure 41: Dimensionless radial stress at the mid-point, $r = (r_i + r_o)/2$, of a FGM cylinder under external pressure shock.	75
Figure 42: Dimensionless tangential stress at the mid-point, $r = (r_i + r_o)/2$, of a FGM cylinder under external pressure shock.	76
Figure 43: Dimensionless spatial radial displacement computed at $t = t_0 = 0.005$ s considering an FGM cylinder under external pressure shock.	77
Figure 44: Dimensionless spatial radial stress computed at $t = t_0 = 0.005$ s considering an FGM cylinder under external pressure shock.	77
Figure 45: Dimensionless spatial tangential stress computed at $t = t_0 = 0.005$ s considering an FGM cylinder under external pressure shock.	78
Figure 46: Composite thick-walled cylinder under exponential internal pressure.	79
Figure 47: Dimensionless radial displacement at the mid-point, $r = (r_i + r_1)/2$, of the inner homogeneous substrate under internal exponential pressure	80
Figure 48: Dimensionless radial stress at the mid-point, $r = (r_i + r_1)/2$, of the inner homogeneous substrate under internal exponential pressure	81

Figure 49: Dimensionless tangential stress at the mid-point, $r = (r_i + r_1)/2$, of the inner homogeneous substrate under internal exponential pressure	81
Figure 50: Dimensionless radial displacement at the mid-point, $r = (r_o + r_1)/2$, of the FGM outer coating under internal exponential pressure.	82
Figure 51: Dimensionless radial stress at the mid-point, $r = (r_o + r_1)/2$, of the FGM outer coating under internal exponential pressure.....	83
Figure 52: Dimensionless tangential displacement at the mid-point, $r = (r_o + r_1)/2$, of the FGM outer coating under internal exponential pressure.....	83
Figure 53: Dimensionless spatial radial displacement computed at $\gamma t = 10$ considering an external FGM coating under internal exponential pressure.	84
Figure 54: Dimensionless spatial radial stress computed at $\gamma t = 10$ considering an external FGM coating under internal exponential pressure.	85
Figure 55: Dimensionless spatial tangential stress computed at $\gamma t = 10$ considering an external FGM coating under internal exponential pressure.	85
Figure 56: Annular internal FGM thick-walled cylinder under internal pressure.....	86
Figure 57: Dimensionless radial displacement at the mid-point, $r = (r_i + r_1)/2$, of the inner FGM coating under internal exponential pressure	88
Figure 58: Dimensionless radial stress at the mid-point, $r = (r_i + r_1)/2$, of the inner FGM coating under internal exponential pressure.....	88
Figure 59: Dimensionless circumferential stress at the mid-point, $r = (r_i + r_1)/2$, of the inner FGM coating under internal exponential pressure.....	89
Figure 60: Dimensionless radial displacement at the mid-point, $r = (r_1 + r_o)/2$, of the outer homogeneous substrate under internal exponential pressure	90
Figure 61: Dimensionless radial stress at the mid-point, $r = (r_1 + r_o)/2$, of the outer homogeneous substrate under internal exponential pressure	91
Figure 62: Dimensionless circumferential stress at the mid-point, $r = (r_1 + r_o)/2$, of the outer homogeneous substrate under internal exponential pressure	91
Figure 63: Dimensionless spatial radial displacement computed at $\gamma t = 10$ considering an internal FGM coating under internal exponential pressure.....	92

Figure 64: Dimensionless spatial radial stress computed at $\gamma t = 10$ considering an internal FGM coating under internal exponential pressure. 93

Figure 65: Dimensionless spatial circumferential stress computed at $\gamma t = 10$ considering an internal FGM coating under internal exponential pressure. 93

CHAPTER 1

INTRODUCTION

1.1 FGM thick-walled cylinders

In 1980's functionally graded materials (FGM), a new class of multiphase composite materials, have become more attracting to researchers and engineering applications due to their ability to withstand high thermo-mechanical loads like in the aerospace environments. They are inhomogeneous microscopically as well as macroscopically because of the spatial variations of the constituent phases along a particular direction. However, the material properties vary gradually according to a power law distribution of the volume fraction of the material constituents through the geometry. Therefore, it eliminates the problems arise from the use of traditional composite materials such as low bond strength between layers and inharmonious properties; hence, maximize material performance, especially by increasing resistance to interface failure. Moreover, its composition and structure can be enhanced depending on the real conditions of use. Since the initiation of the concept, different kinds of manufacturing technologies have been developed for FGMs. These processes include vapor deposition, electrodeposition, thermal spraying, powder metallurgy, additive manufacturing, and liquid state methods [1-3]. Functionally graded material components have become more used in different industries such as aerospace, automotive, machineries, defense, biotechnology, and energy, because such applications require gradual change in composition over a particular direction within the material [1,4-6].

In the early years, the methods of FGM production were classified according to the composition of components, such as metal/metal, metal/ceramic, and ceramic/polymer, etc. Today, different classifications exist for the FGM production methods by structure (discrete and continuous), state (deposition, solid and liquid), graded type (composition, microstructure and porosity), dimensions (thick and thin), the field of application, feasible form complexity, overall process expenses as well as the energy consumption and the environmental impact [7].

Because of their potential for common usage in different fields of engineering, functionally graded thick-walled cylinders, pressure vessels, and disks have been examined extensively. Research studies related to these applications results in improvements in the system behavior.

Thick-walled cylinders fabricated from functionally graded materials which are specifically mixtures of ceramics and metals with continuous variations of the microstructure constituents are commonly used. For FGM cylinders and disks subjected to dynamic loads that may be utilized in aerospace, nuclear, and other industries, analyzing the response is a critical stage. Disks also are extensively used in many mechanical applications such as in steam and turbo generators rotors, turbo-pumps, turbochargers, ship propellers, turbo-alternators, flywheels in vehicles featuring storage of energy and machine tools, wind generators, centrifugal compressors that is widely used in the process industry today, turbine-driven tankers, and in high temperature aerospace industries.

Today, theoretical, numerical and experimental studies on thick-walled cylinders and disks have been carried out by many researchers due to their increasing importance in mechanical applications. The main focus in research studies of pressure vessels was on mechanical behavior under different types of loading conditions. These studies can be divided into two main groups. In the first group of articles, pressure loads on the cylindrical bodies are assumed to be applied gradually. Therefore, the formulation is based on elastostatics. Thus, the studies regarding static loading include analytical solutions for FGM thick-walled cylinders under internal pressure [8,9] and, asymmetric loads [10], internal functionally graded coatings [11], arbitrary property distributions [12], rotating piezoelectric cylinders [13], and cylinders under thermal stresses [14-18]. Fracture mechanics of functionally graded thick-walled cylinders is examined by the weight function technique [19,20] and finite element analysis [21,22]. On the other hand, the second group of work deals with time-dependent loadings, and thus the formulation here is built on the equations of elastodynamics. However, various analytical solution procedures are proposed for elastodynamic analysis of thick-walled functionally graded cylinders. Fu et al. [23] presented a Laplace transform based procedure for coupled thermoelastic analysis of multi-layered and functionally graded hollow cylinders under general transient thermal and mechanical loadings. Nikkhah et al. [24] developed an analytical solution by using separation of variables and

orthogonal expansion technique. Baba and Keles [25] employed Laplace transform to examine free and forced vibrations of functionally graded hollow cylinders and spheres. Lastly, Zhang et al. [26] outlined a wave function expansion technique for dynamic analysis of FGM cylindrical tubes due to SH-waves. Moreover, computational methods developed for elastodynamics of functionally graded thick-walled cylinders help reveal dynamic response characteristics under different types of loading conditions. Hoseini et al. [27] have used a meshless local Petrov-Galerkin method for coupled governing equations of thermoelasticity of FGM thick-walled cylinders. Dorduncu et al. [28] have applied finite difference method to perform the analysis of elastic wave propagation. Sayyidmousavi et al. [29] have performed the dynamic analysis and optimized the graded porous nanocomposite cylinders by using the meshfree radial point interpolation method. Xu et al. [30] have examined the elastodynamics of FGM thick-walled cylinders with a two-dimensional property variation by applying time-domain spectral element method. Additionally, different elastodynamic cases are solved based on finite elements method are illustrated and studied by Shakeri et al. [31], Asemi et al. [32], and Shahabian et al. [33].

Furthermore, other research works have studied the analysis of stresses and strains for disks and, various important and interesting assumptions have been considered in these studies such as geometry of disks, uniformly distributed static or dynamic types of loading (static, dynamic or concentrated). Moreover, the variation of the angular speed of the disks is considered in some researches, the thermo-elastic analysis, and some elastodynamic analysis have been investigated under different thermal loading and boundary conditions, several analytical and computational methods have been used to perform the analysis. Beside the stress and strain analysis most of these works focus on the effect of the gradient index of the functionally graded material [34].

On the other side, the stress analysis of FGM disks is studied by several researchers, Zenkour [35], Callioglu [36] and Eraslan et al. [37] have developed different analytical elastic analysis of FGM rotating disk with constant angular velocity and thickness. In addition, the elastic solution of a variable geometry FGM disk is found analytically and numerically by Yildirim [38] and Zheng et al. [39], respectively.

1.2 Boundary Element Method

Today, without using the numerical techniques, it would be very difficult to solve practical and complicated engineering problems, as the experimental simulation is very costly as well. These techniques in continuum mechanics are based on the idea of deriving some equations that describe accurately the behavior of a small differential element. The numerical methods in continuum can be classified to three approaches: finite difference method, finite element Method FEM and, boundary element Method BEM.

Finite difference method, FDM, is the simplest of all and easy to program, but it has some drawbacks like the difficulty of changing the difference elements in some regions such as the stress concentration areas. Therefore, it is not popular in the stress analysis problems. On the other hand, finite element method, FEM, is the most widespread method used to analyze structures for decades. It has been valued as the modern computational tool since it can solve many realistic problems. The whole domain needs to be discretized into elements and over each element the behavior is described by the governing differential equation. But for infinite domains, it uses fictitious boundaries and this in turn reduces the accuracy. This domain discretization and infinite domain problems are considered as drawbacks and are the main reason for the invention of boundary element method, BEM. The standard form of the BEM is built on transforming the governing differential equations into surface or boundary integral equations; hence, discretizing the boundary into elements. It has resolved the two disadvantages of the FEM and, also showed an effective accuracy in computing fluxes, stresses, strains and moments. It can also easily deal with concentrated forces either in the domain or on the boundary. However, the main disadvantages of BEM are its mathematics complexity, as it requires the establishment of the integral equations and finding the fundamental solution and also the presence of domain integrals in time dependent and nonlinear problems such as dynamic and plasticity problem. During the last three decades, intensive research work has been performed to overcome the obstacles in using the BEM. Nowadays, there are different approaches in BEM that deal with complicated time dependent problems, linear problems with unknown fundamental solution and nonlinear problems like dual reciprocity DR-BEM, analogue equation method AEM, and domain boundary element method D-BEM. However, all

these approaches include domain integral equation in their formulation, so that it requires domain discretization and time marching scheme to approximate the acceleration, but it uses a smaller number of nodes and elements (fully populated matrices) compared to FEM which in turn uses large number of elements and nodes (sparsely populated matrices).

Moreover, since the BEM gives extreme accuracy results for the field solutions, it is beneficial in the research work to verify the results by comparing both methods FEM and BEM. Different BEM methods are developed to find solutions to the time dependent problems. For some simple problems, the time dependent fundamental solution is existing and the integral equations can be developed and hence the application of the TD-BEM. Additionally, even though the fundamental solution is available in some cases, there is a difficulty in deriving the integral equations [40]. These time dependent problems can also be solved in the transformed domain such as Laplace domain; thus, removing time dependency from the boundary integral equations, and the inverse Laplace transform is applied to get the physical quantities. However, the solution obtained is not efficient compared to the time domain solutions, because the inversion transform is a curve fitting process and it can be unstable if too many transform parameters are used, whereas reducing the transform parameters will cause a poor curve fitting [41]. On the other hand, these problems can be solved using the Dual Reciprocity Method DR-BEM, which was first introduced by Brebbia and Nardini [42], when solving the wave dynamic equation domain-boundary integral equations are obtained, and a technique is developed to convert the domain integrals into boundary integrals in order to solve it with the standard BEM. The method is further developed and the Green's reciprocal identity, i.e., the reciprocity principal, is used to transform all the domain integrals to boundary integrals. However, domain nodes can be included at the points desired, and the solution depends on the type of the approximation functions used. Generally, DR-BEM is not feasible in differential equations with variable coefficients [43]. Another efficient method is the Analogue Equation Method, AEM, it solves linear, nonlinear and also coupled equations. The idea is based on replacing any differential equation with another analogue differential equation of the same order with known fundamental solution and, unknown fictitious sources. It is also applied to a set of coupled differential equations, where the analogue equations may be uncoupled equations [43].

The domain-boundary element method formulation D-BEM, on the other hand, employs the static fundamental solution, Kelvin solution, and keeps the domain integral equations resulted from the inertia terms. Therefore, in order to perform the elastodynamic analysis, the discretization of the whole domain and time marching schemes are required. In the current study, we present a novel computational procedure for elastodynamic analysis of functionally graded thick-walled cylinders and annular coatings subjected to pressure shocks. The procedure proposed is based on the domain-boundary element method (DBEM). Although DBEM has been used to solve dynamic problems involving FGM beams and plates and certain types of homogeneous structures, the formulation and implementation for elastodynamics of functionally graded thick-walled cylinders has not been developed. In this work, we show how the method can be formulated and implemented for FGM and composite thick-walled cylinders subjected to pressure shocks over the internal or outer surfaces. The proposed method can deal with general geometries including an arbitrary number of functionally graded material or homogeneous annular bodies.

The main characteristic of the domain-boundary element method is that it uses a static fundamental solution in a weighted residual form instead of time dependent. Hence, the resulted integral equation contains domain integrals, which require discretization of the domain. In the initial uses of DBEM, Beskos et al. [44,45] have examined a transient dynamic response of homogeneous three-dimensional elastoplastic assemblies. Carrer and Mansur [46] have performed the analysis of homogeneous components by proposing an alternative time marching schemes for D-BEM. Carrer et al. [47] have studied the dynamic analysis of Timoshenko beams by employing a D-BEM. Application of D-BEM for dynamic analysis of continuous beams is illustrated by Carrer et al. [48]. On the other hand, domain-boundary element method has been extended to cover the dynamic problems involving functionally graded material plates and beams. Eshraghi and Dag [49, 50] employed D-BEM to study the forced vibrations of FGM circular plates and beams. Ahmed et al. [51] have studied the elastodynamic analysis of fiber-reinforced laminated plates. Finally, Eshraghi and Dag [52] have applied D-BEM to analyze the FGM micro-beams.

Articles in the present literature cover problems involving FGM beams and plates, and different types of homogeneous components. There are no past studies found on domain-boundary element method for elastodynamics of FGM thick-walled cylinders. This study presents a novel DBEM formulation and application for the elastodynamics

of FGM cylinders and coatings subjected to internal and external pressure shocks. The governing partial differential equation of the studied problem is the wave equation for an inhomogeneous axisymmetric domain, and derived in agreement with plane elastodynamics. Thus, the static fundamental solution is obtained and used in the weighted residual form. The governing equation of motion is then converted to an integral equation by shifting the unknown function to the known one using the by parts integration and the boundary conditions. The domain is then discretized by quadratic cells, and the integral equation is transformed to a system of temporal ordinary differential equations. Houbolt method is employed to numerically solve the system of ODEs and to compute radial displacement and stress components. The proposed procedure is validated by comparisons to analytical solutions found in literature for a functionally graded thick-walled cylinder. The obtained results show the elastodynamic behavior of FGM thick-walled cylinders and annular coatings subjected to ramp and exponential types of pressure shock loadings.

1.3 Review of the Literature

The research work found in literature on thick-walled cylinders is divided into mainly two categories. Firstly, the elastostatic problem, Xin et al. [8] have considered the asymmetric state in studying the problem of FGM thick-walled cylinder, which is subjected to an internal pressure shock. The cylinder consists of two linear elastic materials and, the material properties vary according to a certain volume fraction function. They proposed analytical solution that is performed using a hypergeometric function. Non-dimensional expressions for the radial displacement and stresses are used and, the numerical results obtained are compared with the theoretical. The effect of the volume fraction, Poisson's ratio and Young modulus are studied. Another analytical solution for the elastostatic problem is presented by Dui et al. [9] they developed an approximate analytical solution based on the Mori-Tanaka method. An axisymmetric long FGM thick-walled cylinder in plane strain state is considered and, subjected to internal pressure. The wall of the cylinder consists of two isotropic linear elastic materials with a certain volume fraction function. Since the analytical solution of the boundary value governing differential equation is difficult to find, they used an approximation of both the bulk modulus and shear modulus based on Mori-Tanaka method. The numerical results obtained are compared with the results found by FEM

using ANSYS software. Moreover, two other solutions are obtained by using Voigt upper bound and Reuss lower bound and, comparison of the non-dimensional radial, circumferential and axial stresses and non-dimensional radial displacement is performed for all the methods with FEM by ANSYS. However, Hao Li et al. [10] consider a non-symmetric loading in studying FGM thick-walled cylinder. They derived an analytical solution for the displacements and stresses using the complex function theory of Muskhelishvili (1977). In plane strain state, it is based on the idea of expressing the displacements and stresses in terms of two complex potential, and the analytical solutions are derived by dividing the cylinders into several homogeneous layers. On the other side, Sburlati [11] derived analytical solution for the thick-walled FGM cylinder subjected to internal and external pressure in plane strain condition, whereas two types of the volume fraction law of the elasticity modulus are used; power law and exponential law. Furthermore, another solution is obtained in case of FGM coating on the inner surface. Radial displacement and stresses are calculated with considering constant Poisson's ratio and, the effect of material inhomogeneity on the response of the FGM cylinder. However, an arbitrary elastic property varying exponentially is considered in the research work of Chen [12]. The FGM thick-walled cylinder is divided into layers and a continuum conditions at the interface are used, whereas Poisson's ratio is constant. A numerical solution is performed and non-dimensional results of the displacement and stresses are found and the effect of the material property variation is studied. Hong-Yan Zheng et al. [13] derived analytical solution for a FGPM hollow cylinder rotating with a constant speed around its axis. The mechanical, thermal and electrical properties of the piezoelectric material are varying according to a power law along the wall thickness. Uncoupled heat conduction in steady state condition is considered. Numerical results of the radial displacement, stresses and the distribution of the electric potential under mechanical, electric and, thermal loads are calculated and the effect of the inhomogeneity of the material is studied. Moreover, Shao et al. [14] developed an analytical solution for FGM thick-walled cylinder exposed to thermal and mechanical loads. They employed Laplace technique in their solution and, unsteady heat field and, FGM exponential material law are considered. The study of the transient stresses and radial displacement is performed and the effect of the material index variation is studied. Jabbari et al. [15] presented an analytical solution for the FGM thick-walled cylinder. The material properties varied along the radial direction of the wall thickness according to a power law distribution

and, the steady state condition of the uncoupled heat conduction. The axisymmetric thermal mechanical stresses calculations are made. Shao [16] performed an approximated analytical solution for FGM thick-walled cylinder subjected to axisymmetric thermo-mechanical loading. The material properties are assumed to be independent on temperature but varying along the radial direction. But, it is considered to be homogenous for each layer of approximation and a continuity boundary conditions are considered at each interface. Moreover, Peng et al. [17] performed the thermoelastic analysis of FGM long hollow cylinder with material properties, except Poisson's ratio, varies along the radial direction in power law fraction. The heat conduction equation is uncoupled and steady state. The governing boundary value problem is converted into Fredholm integral equation that is solved numerically. The numerical results are presented and the influence of the material gradient on thermal stresses is investigated. A transient two-dimensional thermoelastic problem have been solved by Keder et al. [18]. The material properties are assumed to be temperature and axial direction dependent except Poisson's ratio which is considered constant. The transient heat state is studied for the FGM thick-walled cylinder to investigate the thermal stresses produced and, the influence of the material inhomogeneity on the thermal and mechanical stresses is examined. Whilst the fracture mechanics of the FGM thick-walled cylinder subjected to transient thermomechanical loading has been studied by Dag et al. [19]. A circumferential internal crack is considered and, the cylinder is pressurized internally and externally. The material and thermal properties varied across the wall thickness. A weight function method is introduced to perform the fracture analysis of this problem. The idea is based on deriving analytical solutions of the transient temperature and stresses distributions of the uncracked cylinder by applying finite Henkel transformation. The numerical results obtained by the weight function method is compared to those generated by finite element method. Further analysis is performed to study the effect of the crack depth, time and material property index. Moreover, Dag et al. [20] studied the thermal loads of a circumferentially cracked FGM thick-walled cylinder. The transient temperature distribution is determined by non-Fourier hyperbolic heat conduction and, the transient temperature and stresses distribution are obtained by converting the governing differential equation into Fredholm integral equation in Laplace domain; thus, an inverse Laplace numerical technique is used to obtain these distributions in time domain. Three-dimensional analysis of FGM hollow cylinder with elliptical surface crack has been investigated by

Nami et al. [21]. The cylinder is subjected to a thermo-mechanical loading and, the material properties vary exponentially. A commercial finite element solver ANSYS is used to examine the problem. Farahpour et al. [22] investigate the stress intensity factor of a longitudinal semi-elliptical crack on the inner surface of FGM cylinder. Ansys software (FEM) is used to perform the analysis.

Secondly, the elastodynamic problem of FGM thick-walled cylinders. Some researchers have developed analytical elastodynamic solutions. Fu et al. [23] have investigated the thermoelastic behavior of FGM hollow cylinder under transient thermal and mechanical loading. The inner and outer surfaces of the cylinder are under thermal load and material properties vary along the thickness. Laplace transform method is used to eliminate the time dependence of the coupled differential equations. Then Laplace inverse technique is performed to return the obtained results in time domain. Finally, the effect of heat conduction, coupling effects, loading types and material property index on the thermal and elastic results is studied. Nikkhah et al. [24] have presented analytical elastodynamic solution to FGM thick hollow cylinder subjected to uniform dynamic pressures at the inner and outer surfaces in the absence of the thermal field. The dynamic radial displacement is divided into quasi-static and dynamic parts. The quasi-static part satisfies the static equilibrium and the boundary tractions, whereas the dynamic part, set of eigenfunctions, satisfies the stress-free boundary conditions. The quasi-static radial displacement is found analytically by solving Euler's equation and, the dynamic radial displacement is found analytically by solving Bessel equation. The radial displacement and stress distributions are calculated for different loading conditions and, the effect of material property index is examined. Baba et al. [25] have investigated the effect of anisotropy on the vibration behavior of composite hollow cylinder under internal dynamic pressure. Analytical solution is performed using Laplace transform and, the obtained results are transformed in the time domain using the modified Durbin numerical inversion. Radial displacement and stress distributions results are found under different values of anisotropy parameter. However, Zhang et al. [26] have developed an analytical solution to the elastodynamic response of the FGM hollow cylinder subjected to elastic waves using wavefunction expansion method. The wave fields in the inhomogeneous cylinder and the homogeneous medium that is described with different governing equations of motion, are obtained in different wavefunction series forms. To illustrate the dynamic response

of the FGM cylinder, the dynamic stress concentration factor (DSCF) is introduced and plotted. Hoseini et al. [27] developed the meshless local Petrov Galerkin (MLPG) method to analyze the coupled thermoelasticity problem according to the Green–Naghdi theory in FGM thick hollow cylinders without considering energy dissipation. The local integral equations are found from the weak form of the equations of motion with considering Heaviside step function. The spatial variation of radial displacement and the temperature are approximated using certain interpolation. A system of ordinary differential equations is obtained after the substitution of spatial approximations into the local integral equations obtained. The system of ODE is solved by using the Newmark finite difference method. The effects of different grading indices on the FGM thick-walled cylinder and on transient behaviors of the temperature as well as the displacement fields are discussed. In the research work of Dorduncu et al. [28] wave propagation in FGM circular cylinder subjected to dynamic load has been investigated. The upper surface of the cylinder is considered to be ceramic alumina and the lower surface is nickel. The through-thickness material properties of the FGM circular cylinder were estimated using the Mori–Tanaka homogenization scheme. The governing equations of motion is discretized by the finite difference method. The effect of the grading exponent is examined and, the calculation of the displacements and stresses are performed. Sayyidmousavi et al. [29] have studied the dynamic response of functionally graded porous polymeric cylinders. Three different types of porosity patterns are examined (symmetric, asymmetric and uniform). The meshless scheme used in the solution is radial point interpolation meshfree method (RPIM). The effect of the volume fraction of reinforcement and porosity patterns distribution have been investigated. In addition, Xu et al. [30] have studied dynamic response of FGM thick hollow. An axisymmetric solid spectral finite element model is proposed for the analysis of wave propagation in the cylinder. The material properties vary along the axial direction of the cylinder. Therefore, the upper part of the cylinder is assumed to be made of pure ceramic, whereas the bottom side is considered to be made of pure metal. The method is verified by comparing with the conventional FEM. The dynamic response of displacement and stresses and their time histories components are obtained for different material properties grading indices. Shakeri et al. [31] have used the finite element modelling to perform the analysis of FGM thick-walled cylinder under the impact loading. They subdivide the cylinder into different layers of sub-cylinders and, each layer is considered isotropic and homogenous. Material properties vary between

layers according to a power law in the radial direction. Continuity conditions are placed at the interface between the layers. The time histories and responses are calculated first in the frequency domain by using fast Fourier transform. In addition, Asemi et al. [32] introduced finite elements method based on Rayleigh-Ritz energy formulation to study the response of FGM thick-walled cylinder under ramp shock pressure. The material property is varying according to a power law except Poisson's ratio which is assumed constant. The response of displacement, stresses, wave propagation and velocities of radial stress wave propagation for various material property exponents have been examined. Shahabian et al. [33] have presented a stochastic dynamic response of FGM thick hollow cylinder with uncertain material properties, random values are generated using Monte Carlo method, subjected to a uniform dynamic internal pressure. The dynamic governing differential equation is solved using Galerkin finite element and Newmark finite difference methods but, no thermal field is applied and the outer surface is traction free.

However, most of the research works on the FGM disks in literature are related to the elastic or coupled and uncoupled thermoelastic analysis with different boundary conditions, and geometries. Researchers have investigated the FGM disks, rotating or stationary, in many different thermal and mechanical fields and provide analytical, semi analytical and numerical solutions with various methods. Ali Kursun et al. [53] have investigated the effect of the gradient index on a stationary FGM constant thickness disk. The thermoelastic analysis is studied considering a uniform constant inner pressure, fixed outer surface of the disk and a linear temperature distribution; hence, an analytical solution is obtained. Bektas et al. [54] have studied a stationary FGM disk, with constant thickness and two different grading indexes, considering the thermal field of uniform and linear temperature distribution. An analytical solution of the thermoelastic problem was developed under constant internal pressure and traction free outer surface and, compared to the results obtained from the finite element commercial software ANSYS. Ootao et al. [55] have studied the transient thermoelastic analysis of a FGM stationary disk with traction free surfaces. Hence, they developed an analytical solution by using Laplace transformation and Bessel functions in both the governing differential equations; the transient thermal and the thermoelastic equations.

The coupled thermoelastic analysis of a FGM stationary disk is studied by Eslami et al. [56], a plane stress assumption is considered and the boundary conditions are specified. The inner surface is considered traction free and subjected to thermal shock, whereas the outer surface is thermally insulated and fixed. However, since there is a time rate change of the thermal boundary condition at the inner surface, a couple is occurred between the elastic and the thermal fields, and they have used Galerkin finite element method after using the Laplace transform to change the time domain into the space domain.

Therefore, by considering the reviewed studies on FGM thick-walled cylinders, no one has used the domain boundary element method, D-BEM, with Houbolt's time marching scheme to perform the elastodynamic analysis. Thus, this new computational technique will be developed to study the dynamic response of the functionally graded material thick-walled cylinders (stationary disks) under different types of loadings. Hence, in this research, the study of the response of time dependent of radial displacement and stresses, spatial radial displacements and stresses; as well as, investigating the effect of the inhomogeneity grading index of material that is varying in the radial direction will be performed.

CHAPTER 2

RESEARCH METHODOLOGY

2.1 Statement of the Problem

In this study, FGM thick-walled cylinder or hollow disk is considered. The thick-walled cylinder has an inner radius, r_i , an outer radius, r_o , and a constant thickness, h , and it has been illustrated in the cylindrical coordinate system (r, θ, z) , as shown in fig. (1). In addition, it is assumed that the cylinder's material consists of two distinct materials at the inner and outer radius, and the material physical properties, $P(r)$, vary along the radial direction with power law distribution of the volume fraction, to describe a functionally graded material, as follows:

$$Pr(r) = Pr_o \left(\frac{r}{r_o} \right)^n \quad (1)$$

Where,

$Pr(r)$, is a generic material property.

Pr_o , property at the outer radius.

n , grading index of the material.

r_o , outer radius of the disk.

Hence, the modulus of elasticity, $E(r)$, the mass density, $\rho(r)$, are varying along the radial direction, whereas the Poisson's ratio is considered constant ($\nu = 0.3$). The constancy of Poisson's ratio is due to the fact that it generally varies between values that are closed to each other; and hence, the effect of this variation is not important when compared to the effect of the other physical material properties [24,32].

Since the geometry is symmetric and according to the applied boundary conditions, the problem is considered axisymmetric.

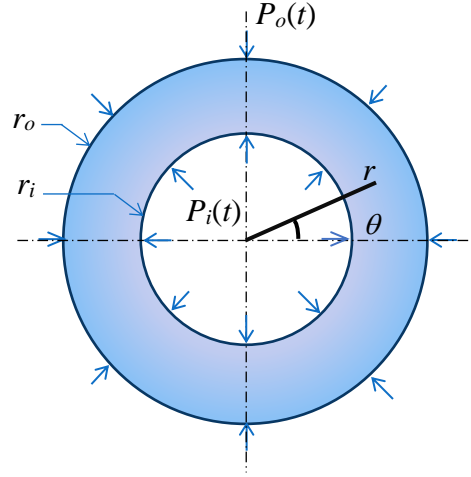


Figure 1: FGM thick-walled cylinder under pressure shocks.

2.1.1 Elastodynamic Formulation

An element of the thick-walled cylinder with all the tractions is illustrated in figure (2). Hence, by ignoring the gravity effect and all parts of the cylinder are not subjected to any centrifugal force; therefore, radial force, f_r , and the circumferential force, f_θ will vanish. On the other hand, an external asymmetric dynamic loading, $P_o(t, \theta)$ and internal axisymmetric loading, $P_i(t)$, are considered on the outer and inner surfaces of the thick-walled cylinder, respectively, as shown in figure (1).

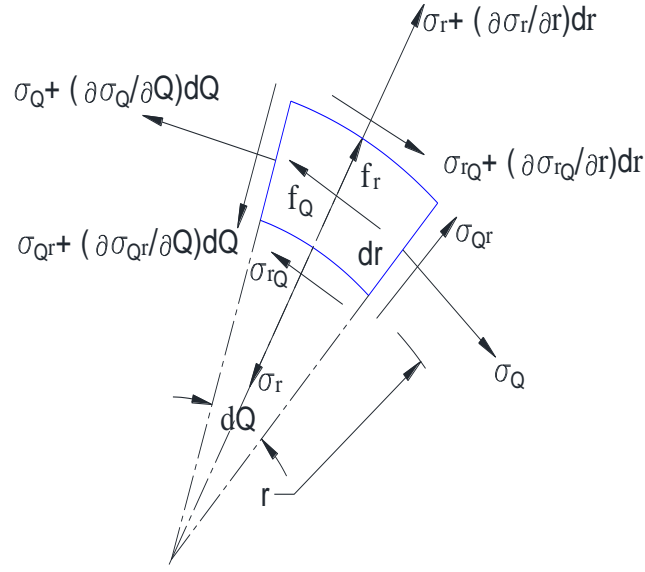


Figure 2: Two-dimensional element in polar coordinates

Therefore, for the element in the plane stress condition, the two-dimensional equilibrium equations can be written as follows:

In the r -direction
$$\sum F = \rho(r) dv \frac{\partial^2 u_r(r, \theta, t)}{\partial t^2} \quad (2)$$

In the θ -direction
$$\sum F = \rho(r) dv \frac{\partial^2 u_\theta(r, \theta, t)}{\partial t^2} \quad (3)$$

Where,

$$dv = h r d\theta dr \quad (4)$$

Substituting the summation of forces in the radial direction, in equation (2):

$$\begin{aligned} & \left(\sigma_{rr} + \frac{\partial \sigma_{rr}}{\partial r} dr \right) (r + dr) h d\theta - \sigma_{rr} r h d\theta - \sigma_{\theta\theta} h dr \sin \frac{d\theta}{2} \\ & - \left(\sigma_{\theta\theta} + \frac{\partial \sigma_{\theta\theta}}{\partial \theta} d\theta \right) h dr \sin \frac{d\theta}{2} + f_r = \rho(r) r h d\theta dr \frac{\partial^2 u_r(r, \theta, t)}{\partial t^2} \end{aligned} \quad (5)$$

Substituting the summation of forces in the circumferential direction, in equation (3)

$$\begin{aligned}
& \left(\sigma_{r\theta} + \frac{\partial \sigma_{r\theta}}{\partial r} dr \right) (r + dr) h d\theta - \sigma_{r\theta} r h d\theta - \sigma_{\theta\theta} h dr \cos \frac{d\theta}{2} \\
& + \left(\sigma_{r\theta} + \frac{\partial \sigma_{r\theta}}{\partial \theta} d\theta \right) h dr \sin \frac{d\theta}{2} + \left(\sigma_{\theta\theta} + \frac{\partial \sigma_{\theta\theta}}{\partial \theta} d\theta \right) h dr \cos \frac{d\theta}{2} \\
& + \sigma_{r\theta} r h \sin \frac{d\theta}{2} + f_\theta = \rho(r) r h d\theta dr \frac{\partial^2 u_\theta(r, \theta, t)}{\partial t^2}
\end{aligned} \tag{6}$$

Simplifying and dividing equations (5 & 6) by elemental volume, dv , the elastodynamic equations of motion are obtained, as follows:

$$\frac{\partial \sigma_{rr}}{\partial r} + \frac{1}{r} \frac{\partial \sigma_{r\theta}}{\partial \theta} + \frac{\sigma_{rr} - \sigma_{\theta\theta}}{r} = \rho(r) \frac{\partial^2 u_r(r, \theta, t)}{\partial t^2} \tag{7}$$

$$\frac{\partial \sigma_{r\theta}}{\partial r} + \frac{1}{r} \frac{\partial \sigma_{\theta\theta}}{\partial \theta} + \frac{2\sigma_{r\theta}}{r} = \rho(r) \frac{\partial^2 u_\theta(r, \theta, t)}{\partial t^2} \tag{8}$$

However, for either plane stress or plane strain condition with axisymmetric geometry and loading, the governing equation of motion is eqn. (7).

The linear constitutive elastic equations for plane stress are as follows:

$$\varepsilon_{rr} = \frac{1}{E(r)} (\sigma_{rr} - \nu \sigma_{\theta\theta}) \tag{9}$$

$$\varepsilon_{\theta\theta} = \frac{1}{E(r)} (\sigma_{\theta\theta} - \nu \sigma_{rr}) \tag{10}$$

The linear relations between the strain and the displacement components in polar coordinates formulation are given by:

$$\varepsilon_{rr} = \frac{\partial u_r(r, t)}{\partial r} \tag{11}$$

$$\varepsilon_{\theta\theta} = \frac{u_r(r, t)}{r} \tag{12}$$

Therefore, the linear constitutive relations in terms of stresses are:

$$\sigma_{rr} = \frac{E(r)}{1-\nu^2} (\varepsilon_{rr} + \nu \varepsilon_{\theta\theta}) \quad (13)$$

$$\sigma_{\theta\theta} = \frac{E(r)}{1-\nu^2} (\varepsilon_{\theta\theta} + \nu \varepsilon_{rr}) \quad (14)$$

Where,

u_r , u_θ , are the radial and the circumferential displacements, respectively.

ε_{rr} and, $\varepsilon_{\theta\theta}$, are the radial and circumferential strains, respectively.

Hence, the problem is axisymmetric and the governing elastodynamic equation of motion for a FGM thick-walled cylinder in displacement formulation can be obtained by substituting linear constitutive equations in terms of stresses and the strain equations into the elastodynamic equation of motion, as follows:

$$\begin{aligned} & \frac{\partial^2 u_r(r,t)}{\partial r^2} + \left(\frac{1}{E(r)} \frac{dE(r)}{dr} + \frac{1}{r} \right) \frac{\partial u_r(r,t)}{\partial r} + \left(\frac{\nu}{E(r)} \frac{dE(r)}{dr} - \frac{1}{r} \right) \frac{u_r(r,t)}{r} \\ &= \frac{\rho(r)(1-\nu^2)}{E(r)} \left(\frac{\partial^2 u_r(r,t)}{\partial t^2} \right) \end{aligned} \quad (15)$$

The elasticity modulus:

$$E(r) = E_o \left(\frac{r}{r_o} \right)^{n_1} \quad (16)$$

The density:

$$\rho(r) = \rho_o \left(\frac{r}{r_o} \right)^{n_2} \quad (17)$$

For the plane strain, we can get the elasticity modulus $\bar{E}(r)$ and Poisson's ratio $\bar{\nu}$ from the plane stress, as follows:

$$\bar{E}(r) = \frac{E(r)}{1-\nu^2} \quad (18)$$

$$\bar{\nu} = \frac{\nu}{1-\nu} \quad (19)$$

Substituting the elasticity modulus and the density in the equation of motion (15), we get:

$$\frac{\partial^2 u_r(r,t)}{\partial r^2} + \frac{n_1+1}{r} \frac{\partial u_r(r,t)}{\partial r} + \frac{\bar{\nu}n_1-1}{r^2} u_r(r,t) = \frac{\rho_o(1-\bar{\nu}^2)}{\bar{E}_o r_o^{(n_2-n_1)}} r^{(n_2-n_1)} \frac{\partial^2 u_r(r,t)}{\partial t^2} \quad (20)$$

2.1.1.1 Boundary and Initial Conditions

Since the problem is axisymmetric, the stress boundary conditions of the composite thick-walled cylinder are expressed as:

$$\sigma_r(r_i, t) = -P_i(t) \quad (21)$$

$$\sigma_r(r_o, t) = -P_o(t) \quad (22)$$

The initial conditions can be written as,

$$u_r(r, 0) = u_{r_o}(r) \quad (23)$$

$$\dot{u}_r(r, 0) = \dot{u}_{r_o}(r) \quad (24)$$

Where, $u_{r_o}(r)$ and $\dot{u}_{r_o}(r)$ are the initial radial displacement, and the initial radial velocity, respectively.

CHAPTER 3

D-BEM FORMULATION

3.1 Fundamental Solution

The idea is to transform the governing partial differential equation into integral equation by employing the weight residual form; whereas the solution is only possible by using the discretization techniques.

In the D-BEM, the static fundamental solution is used and not the time dependent fundamental solution. Therefore, let us consider $u_r^*(r, \xi)$ be the fundamental solution for this case study, and seeking the static fundamental solution that satisfies the governing equation of motion.

However, the fundamental solution, point load (Kelvin solution) physically expresses the displacements produced in a body by a concentrated unit load. Consider the unit concentrated force $F(F_\xi)$, $|F| = 1$ is applied at an interior point, $P(r, \theta)$, in the domain, Ω , and the effect of this force is found at any other point in the domain, $Q(\xi, \theta)$. The density of the body forces produced by the force F at the point $Q(\xi, \theta)$ can be expressed using the delta function $\delta(r - \xi)$, as illustrated in fig. (3). Therefore, the Navier, displacement formulation, linear equation, used to find the static fundamental solution by substituting the fundamental solution, is as follows:

$$\frac{\partial^2 u_r^*(r, \xi)}{\partial r^2} + \frac{n_1 + 1}{r} \frac{\partial u_r^*(r, \xi)}{\partial r} + \frac{\bar{\nu} n_1 - 1}{r^2} u_r^*(r, \xi) = \delta(r - \xi) \quad (25)$$

Where, the delta function is:

$$\delta(r - \xi) = \begin{cases} \infty & r = \xi \\ 0 & r \neq \xi \end{cases} \quad (26)$$

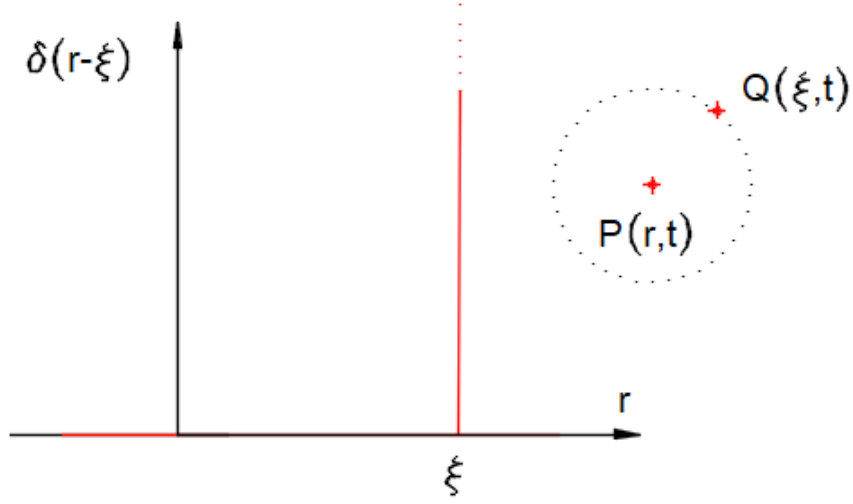


Figure 3: Dirac delta and Kelvin problem

The fundamental solution is expressed as:

$$u_r^*(r, \xi) = H(r - \xi) w(r, \xi) \quad (27)$$

$H(r - \xi)$, is the Heaviside unit step function.

$$H(r - \xi) = \begin{cases} 1 & r > \xi \\ 0 & r < \xi \end{cases} \quad (28)$$

$w(r, \xi)$, is a kernel that satisfies the homogeneous PDE with the conditions:

$$w|_{r=\xi} = \frac{dw}{dr}|_{r=\xi} = \dots = \frac{d^{n-2}w}{dr^{n-2}}|_{r=\xi} = 0 \quad (29)$$

$$\frac{d^{n-1}w}{dr^{n-1}}|_{r=\xi} = 1 \quad (30)$$

So, in the case of the governing equation (25), the resulting conditions are:

$$w|_{r=\xi} = 0, \text{ and } \frac{dw}{dr}|_{r=\xi} = 1 \quad (31)$$

Hence, the fundamental solution $u_r^*(r, \xi)$ at point $Q(\xi, t)$ is the solution of homogenous PDE (25).

Substituting the fundamental solution eqn. (27) in eqn. (25), and considering the derivatives as follows:

$$\frac{du_r^*(r, \xi)}{dr} = \frac{dH(r - \xi)}{dr} w(r, \xi) + H(r - \xi) \frac{dw(r, \xi)}{dr} \quad (32)$$

Where,

$$\frac{dH(r - \xi)}{dr} = \delta(r - \xi) \quad (33)$$

$$\frac{du_r^*(r, \xi)}{dr} = \delta(r - \xi) w(r, \xi) + H(r - \xi) \frac{dw(r, \xi)}{dr} \quad (34)$$

By substituting the condition from eqn. (31), we get:

$$\frac{du_r^*(r, \xi)}{dr} = H(r - \xi) \frac{dw(r, \xi)}{dr} \quad (35)$$

Similarly,

$$\frac{d^2 u_r^*(r, \xi)}{dr^2} = \delta(r - \xi) \frac{dw(r, \xi)}{dr} + H(r - \xi) \frac{d^2 w(r, \xi)}{dr^2} \quad (36)$$

$$\frac{d^2 u_r^*(r, \xi)}{dr^2} = \delta(r - \xi) + H(r - \xi) \frac{d^2 w(r, \xi)}{dr^2} \quad (37)$$

By substituting eqns. (27, 35, and 37 into eqn. (25), we get:

$$\begin{aligned} & \delta(r - \xi) + H(r - \xi) \frac{d^2 w(r, \xi)}{dr^2} + \frac{n_1 + 1}{r} H(r - \xi) \frac{dw(r, \xi)}{dr} \\ & + \frac{\bar{v} n_1 - 1}{r^2} H(r - \xi) w(r, \xi) = \delta(r - \xi) \end{aligned} \quad (38)$$

Then, by substituting and simplifying and for $r > \xi$,

$$\frac{d^2 w(r, \xi)}{dr^2} + \frac{n_1 + 1}{r} \frac{dw(r, \xi)}{dr} + \frac{\bar{v} n_1 - 1}{r^2} w(r, \xi) = 0 \quad (39)$$

This is non-homogeneous Cauchy-Euler equation and the solution can be found easily by using:

$$w(r) = r^m \quad (40)$$

The solution is:

$$w(r) = C_1 r^{\frac{-n_1 + \sqrt{n_1^2 - 4n_1\bar{\nu} + 4}}{2}} + C_2 r^{\frac{-n_1 - \sqrt{n_1^2 - 4n_1\bar{\nu} + 4}}{2}} \quad (41)$$

The conditions eqn. (31) are used to find the constants C_1 and C_2 . Thus, the fundamental solution $u_r^*(r, \xi)$ at any point in the domain $Q(\xi, t)$ is the solution of homogenous DE obtained:

$$w(r, \xi) = \frac{\xi}{a_1} \left[\left(\frac{r}{\xi} \right)^{\frac{-n_1 + a_1}{2}} - \left(\frac{r}{\xi} \right)^{\frac{-n_1 - a_1}{2}} \right] \quad (42)$$

Where,

$$a_1 = \sqrt{n_1^2 - 4n_1\bar{\nu} + 4} \quad (43)$$

3.2 The Integral Equation

The Fundamental solution is used in BEM to write the governing PDE in the weight-residual form. The idea is to consider the residual remains when inserting the approximated solution in the governing PDE, multiplies this residual with the fundamental solution (weighting function), and seeking the disappearance of this product over the domain.

$$\int_{r_i}^{r_o} \left[\frac{\partial^2 u_r(r,t)}{\partial r^2} + \frac{n_1+1}{r} \frac{\partial u_r(r,t)}{\partial r} + \frac{\bar{v}n_1-1}{r^2} u_r(r,t) - \frac{\rho_o(1-\bar{v}^2)r^{(n_2-n_1)}}{\bar{E}_o r_o^{(n_2-n_1)}} \frac{\partial^2 u_r(r,t)}{\partial t^2} \right] u_r^*(r,\xi) dr = 0 \quad (44)$$

Hence, to obtain the integral equation formulation, all the differentiation acting on the unknown function, $u_r(r,t)$, are shifted by the integration by parts to act on the known function (fundamental solution), $u_r^*(r,\xi)$.

$$\begin{aligned} \int_{r_i}^{r_o} \frac{\partial^2 u_r(r,t)}{\partial r^2} u_r^*(r,\xi) dr &= \left[\frac{\partial u_r(r,t)}{\partial r} u_r^*(r,\xi) - u_r(r,t) \frac{du_r^*(r,\xi)}{dr} \right]_{r_i}^{r_o} \\ &+ \int_{r_i}^{r_o} \frac{\partial^2 u_r^*(r,\xi)}{\partial r^2} u_r(r,t) dr \end{aligned} \quad (45)$$

$$\begin{aligned} \int_{r_i}^{r_o} \frac{n+1}{r} \frac{\partial u_r(r,t)}{\partial r} u_r^*(r,\xi) dr &= \left[\frac{n+1}{r} u_r(r,t) u_r^*(r,\xi) \right]_{r_i}^{r_o} \\ &- \int_{r_i}^{r_o} \frac{n+1}{r} \frac{du_r^*(r,\xi)}{dr} u_r(r,t) dr + \int_{r_i}^{r_o} \frac{n+1}{r^2} u_r^*(r,\xi) u_r(r,t) dr \end{aligned} \quad (46)$$

Substituting in eqn. (44), we get:

$$\begin{aligned}
& \left[\frac{\partial u_r(r,t)}{\partial r} u_r^*(r,\xi) + \left(\frac{n_1+1}{r} u_r^*(r,\xi) - \frac{\partial u_r^*(r,\xi)}{\partial r} \right) u_r(r,t) \right]_{r_i}^{r_o} + \\
& \int_{r_i}^{r_o} \left(\frac{\partial^2 u_r^*(r,\xi)}{\partial r^2} + \frac{n_1+1}{r} \frac{\partial u_r^*(r,\xi)}{\partial r} + \frac{\bar{v}n_1-1}{r^2} u_r^*(r,\xi) \right) u_r(r,t) dr + \\
& \int_{r_i}^{r_o} \left(\frac{n_1+1}{r^2} u_r^*(r,\xi) - 2 \frac{n_1+1}{r} \frac{\partial u_r^*(r,\xi)}{\partial r} \right) u_r(r,t) dr \\
& = \frac{\rho_o(1-\bar{v}^2)}{\bar{E}_o r_o^{(n_2-n_1)}} \int_{r_i}^{r_o} r^{(n_2-n_1)} u_r^*(r,\xi) \frac{\partial^2 u_r(r,t)}{\partial t^2} dr
\end{aligned} \tag{47}$$

Simplifying,

$$\begin{aligned}
& u_r(\xi,t) + \left[\frac{\partial u_r(r_o,t)}{\partial r} u_r^*(r_o,\xi) + \left(\frac{n_1+1}{r_o} u_r^*(r_o,\xi) - \frac{\partial u_r^*(r_o,\xi)}{\partial r} \right) u_r(r_o,t) \right] + \\
& \left[- \frac{\partial u_r(r_i,t)}{\partial r} u_r^*(r_i,\xi) - \left(\frac{n_1+1}{r_i} u_r^*(r_i,\xi) - \frac{\partial u_r^*(r_i,\xi)}{\partial r} \right) u_r(r_i,t) \right] + \\
& \int_{r_i}^{r_o} \left(\frac{n_1+1}{r^2} u_r^*(r,\xi) - 2 \frac{n_1+1}{r} \frac{\partial u_r^*(r,\xi)}{\partial r} \right) u_r(r,t) dr \\
& = \frac{\rho_o(1-\bar{v}^2)}{\bar{E}_o r_o^{(n_2-n_1)}} \int_{r_i}^{r_o} r^{(n_2-n_1)} u_r^*(r,\xi) \frac{\partial^2 u_r(r,t)}{\partial t^2} dr
\end{aligned} \tag{48}$$

Using the stress boundary conditions:

$$\sigma_r = -P_o(t), \text{ at the outer radius, } r = r_o.$$

$$\sigma_r = -P_i(t), \text{ at the inner radius, } r = r_i.$$

From the constitutive equations, we get:

$$\frac{\partial u_r(r_i, t)}{\partial r} = -\frac{\bar{v}}{r_i} u_r(r_i, t) - P_i(t) \frac{(1 - \bar{v}^2)}{\bar{E}_i} \quad (49)$$

$$\frac{\partial u_r(r_o, t)}{\partial r} = -\frac{\bar{v}}{r_o} u_r(r_o, t) - P_o(t) \frac{(1 - \bar{v}^2)}{\bar{E}_o} \quad (50)$$

Substituting the equations of derivatives, we get the integral equation:

$$u_r(\xi, t) + \left[\left(\frac{n_1 + 1 - \bar{v}}{r_o} u_r^*(r_o, \xi) - \frac{\partial u_r^*(r_o, \xi)}{\partial r} \right) u_r(r_o, t) - \left(\frac{n_1 + 1 - \bar{v}}{r_i} u_r^*(r_i, \xi) - \frac{\partial u_r^*(r_i, \xi)}{\partial r} \right) u_r(r_i, t) \right] + \int_{r_i}^{r_o} \left(\frac{n_1 + 1}{r^2} u_r^*(r, \xi) - 2 \frac{n_1 + 1}{r} \frac{\partial u_r^*(r, \xi)}{\partial r} \right) u_r(r, t) dr = \quad r_i < \xi < r_o. \quad (51)$$

$$\frac{\rho_o(1 - \bar{v}^2)}{\bar{E}_o r_o^{(n_2 - n_1)}} \int_{r_i}^{r_o} r^{(n_2 - n_1)} u_r^*(r, \xi) \frac{\partial^2 u_r(r, t)}{\partial t^2} dr + P_o(t) \frac{(1 - \bar{v}^2)}{\bar{E}_o} u_r^*(r_o, \xi) - P_i(t) \frac{(1 - \bar{v}^2)}{\bar{E}_i} u_r^*(r_i, \xi)$$

However, the presence of the inertial domain integral and the non-linearity term in the integral equation will require the discretization of the domain.

3.3 Numerical Procedure

Because of the presence of inertia and the axisymmetric of the problem, the domain can be described as a line connecting the inner and the outer rims of the thick-walled cylinder (blue line), as shown in figure (4). Therefore, the domain line is discretized into isoparametric quadratic elements, to ensure that the geometry and the variables are approximated with an equal order. However, shape functions, developed in finite elements and taken to boundary element, are used to describe the geometry and behavior of any element, because they use the nodes on the element that have the variable value.

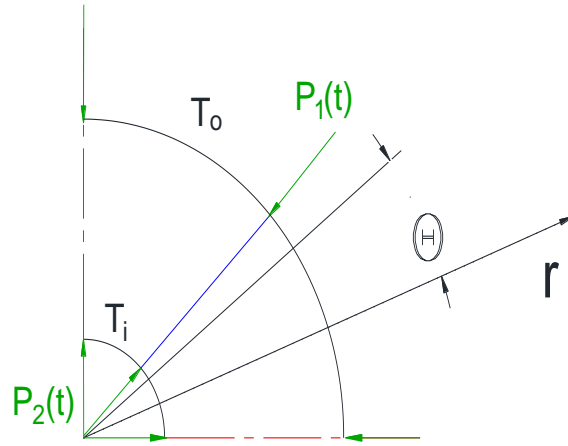


Figure 4: Domain and symmetric boundary conditions

Thus, the domain is discretized and divided into a number of quadratic elements, M , and each cell has three nodes, as shown in figure (5).

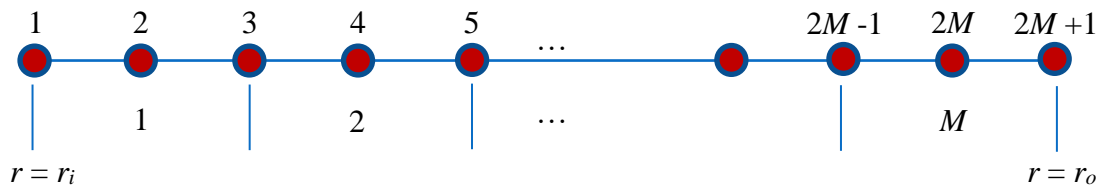


Figure 5: Domain discretization into quadratic elements

The total number of nodes, N , is found by the following relation:

$$N = 2M + 1 \quad (52)$$

Hence, for the j^{th} element, there are 3 nodes and, $1 \leq j \leq M$ and, to approximate the value of the displacement variable $u_r(r, t)$ and its second derivative $\ddot{u}_r(r, t)$ at any node and at time t , a polynomial of second order, Lagrange interpolation, shape functions are used, as follows:

$$u_r^{(j)}(r, t) = \sum_{k=1}^3 N_k^{(j)}(r) u_r(r_k^{(j)}, t) \quad (53)$$

$$\ddot{u}_r^{(j)}(r, t) = \sum_{k=1}^3 N_k^{(j)}(r) \ddot{u}_r(r_k^{(j)}, t) \quad (54)$$

where $u_r(r_k^{(j)}, t)$ and $\ddot{u}_r(r_k^{(j)}, t)$ are the displacement and acceleration in nodal description and, $N_i^{(j)}(r)$, are the shape functions of second degree:

$$N_1^{(j)}(r) = \frac{(r - r_2^{(j)})(r - r_3^{(j)})}{2l^2} \quad (55)$$

$$N_2^{(j)}(r) = -\frac{(r - r_1^{(j)})(r - r_3^{(j)})}{l^2} \quad (56)$$

$$N_3^{(j)}(r) = \frac{(r - r_1^{(j)})(r - r_2^{(j)})}{2l^2} \quad (57)$$

Where, l , is the half length of the element.

$$l = (r_2^{(j)} - r_1^{(j)}) = (r_3^{(j)} - r_2^{(j)}) \quad (58)$$

After considering the approximation using the shape functions, an approximate time dependent integral equation is obtained, as follows:

$$\begin{aligned}
& u_r(\xi, t) + \left(\frac{n_1 + 1 - \bar{\nu}}{r_o} u_r^*(r_o, \xi) - \frac{\partial u_r^*(r_o, \xi)}{\partial r} \right) u_r(r_o, t) \\
& - \left(\frac{n_1 + 1 - \bar{\nu}}{r_i} u_r^*(r_i, \xi) - \frac{\partial u_r^*(r_i, \xi)}{\partial r} \right) u_r(r_i, t) \\
& + \sum_{j=1}^M \int_{r_1^{(j)}}^{r_3^{(j)}} \left(\frac{n_1 + 1}{r^2} u_r^*(r, \xi) - 2 \frac{n_1 + 1}{r} \frac{\partial u_r^*(r, \xi)}{\partial r} \right) \left(\sum_{k=1}^3 N_k^{(j)}(r) u_r(r_k^{(j)}, t) \right) dr \\
& - \frac{\rho_o (1 - \bar{\nu}^2)}{\bar{E}_o r_o^{(n_2 - n_1)}} \sum_{j=1}^M \int_{r_1^{(j)}}^{r_3^{(j)}} r^{(n_2 - n_1)} u_r^*(r, \xi) \left(\sum_{k=1}^3 N_k^{(j)}(r) \ddot{u}_r(r_k^{(j)}, t) \right) dr \\
& = P_o(t) \frac{1 - \bar{\nu}^2}{\bar{E}_o} u_r^*(r_o, \xi) - P_i(t) \frac{1 - \bar{\nu}^2}{\bar{E}_i} u_r^*(r_i, \xi), \quad r_i < \xi < r_o.
\end{aligned} \tag{59}$$

Once the spatial discretization is accomplished, the obtained integral equation is applied to the boundary and internal nodes generating a system of algebraic equations; Hence,

However, by using N collocation points, eqn. (59) is reduced to a temporal system of ordinary differential equations.

These collocation points are considered as nodes and, the coordinates become:

$$\xi_k = (r_i, r_o), \quad k = (1, N), \quad \text{for the boundary nodes.}$$

$$\xi_k = (r_i + l, r_i + 2l, \dots, r_i + (N-1)l), \quad k = (2, 3, \dots, N-1), \quad \text{for the domain nodes.}$$

Thus, the resulting matrix form of the system of ordinary differential equations is written as follows:

$$\begin{bmatrix} \mathbf{S}^{bb} & \mathbf{S}^{bd} \\ \mathbf{S}^{db} & \mathbf{S}^{dd} \end{bmatrix} \begin{bmatrix} \ddot{\mathbf{u}}_r^b \\ \ddot{\mathbf{u}}_r^d \end{bmatrix} + \begin{bmatrix} \mathbf{H}^{bb} + \mathbf{G}^{bb} & \mathbf{G}^{bd} \\ \mathbf{H}^{db} + \mathbf{G}^{db} & \mathbf{H}^{dd} + \mathbf{G}^{dd} \end{bmatrix} \begin{bmatrix} \mathbf{u}_r^b \\ \mathbf{u}_r^d \end{bmatrix} = \begin{bmatrix} \mathbf{C}^b \\ \mathbf{C}^d \end{bmatrix} \tag{60}$$

The superscripts b and d are pointed to the boundary and domain nodes, respectively.

However, the displacements vectors are defined as follows:

$$\mathbf{u}_r^b = \begin{bmatrix} u_r(r_i, t) \\ u_r(r_o, t) \end{bmatrix} \quad (61)$$

and, its size is (2 x 1).

$$\mathbf{u}_r^d = \begin{bmatrix} u_r(r_i + l, t) \\ u_r(r_i + 2l, t) \\ \vdots \\ u_r(r_i + (N-1)l, t) \end{bmatrix} \quad (62)$$

and, its size is ((N-2) x 1).

Whereas, the acceleration vectors are defined as follows:

$$\ddot{\mathbf{u}}_r^b = \begin{bmatrix} \ddot{u}_r(r_i, t) \\ \ddot{u}_r(r_o, t) \end{bmatrix} \quad (63)$$

and, its size is (2 x 1).

$$\ddot{\mathbf{u}}_r^d = \begin{bmatrix} \ddot{u}_r(r_i + l, t) \\ \ddot{u}_r(r_i + 2l, t) \\ \vdots \\ \ddot{u}_r(r_i + (N-1)l, t) \end{bmatrix} \quad (64)$$

and, its size is ((N-2) x 1).

The system of ordinary differential equations is written in the complete form as follows:

$$\begin{aligned}
& \left[\begin{array}{cc} [S_{11} & S_{1N}]^{bb} & [S_{12} & S_{13} & \cdots & S_{1(N-1)}]^{bd} \\ [S_{N1} & S_{NN}] & [S_{N2} & S_{N3} & \cdots & S_{N(N-1)}] \end{array} \right] \left[\begin{array}{c} \left\{ \ddot{U}_{r_{11}}^b \right\} \\ \left\{ \ddot{U}_{r_{21}}^b \right\} \\ \ddot{U}_{r_{11}}^d \\ \ddot{U}_{r_{21}}^d \\ \vdots \\ \ddot{U}_{r_{(N-2)1}}^d \end{array} \right] + \\
& \left[\begin{array}{cc} [S_{21} & S_{2N}]^{db} & [S_{22} & S_{23} & \cdots & S_{2(N-1)}]^{dd} \\ [S_{31} & S_{3N}] & [S_{32} & S_{33} & \cdots & S_{3(N-1)}] \\ \vdots & \vdots & \vdots & \vdots & \cdots & \vdots \\ \vdots & \vdots & \vdots & \vdots & \cdots & \vdots \\ S_{(N-1)1} & S_{(N-1)N} & S_{(N-1)2} & S_{(N-1)3} & \cdots & S_{(N-1)(N-1)} \end{array} \right] \left[\begin{array}{c} \ddot{U}_{r_{11}}^d \\ \ddot{U}_{r_{21}}^d \\ \vdots \\ \ddot{U}_{r_{(N-2)1}}^d \end{array} \right] + \\
& \left(\left[\begin{array}{cc} [H_{11}^{bb} & H_{12}^{bb}] & [H_{11}^{bd} & H_{12}^{bd} & \cdots & H_{1(N-2)}^{bd}] \\ [H_{21}^{bb} & H_{22}^{bb}] & [H_{21}^{bd} & H_{22}^{bd} & \cdots & H_{2(N-2)}^{bd}] \\ [H_{11}^{db} & H_{12}^{db}] & [H_{11}^{dd} & H_{12}^{dd} & \cdots & H_{1(N-2)}^{dd}] \\ [H_{21}^{db} & H_{22}^{db}] & [H_{21}^{dd} & H_{22}^{dd} & \cdots & H_{2(N-2)}^{dd}] \\ \vdots & \vdots & \vdots & \vdots & \cdots & \vdots \\ \vdots & \vdots & \vdots & \vdots & \cdots & \vdots \\ H_{(N-2)1}^{db} & H_{(N-2)2}^{db} & H_{(N-2)1}^{dd} & H_{(N-2)2}^{dd} & \cdots & H_{(N-2)(N-2)}^{dd} \end{array} \right] + \left[\begin{array}{c} \left\{ U_{r_{11}}^b \right\} \\ \left\{ U_{r_{21}}^b \right\} \\ U_{r_{11}}^d \\ U_{r_{21}}^d \\ \vdots \\ U_{r_{(N-2)1}}^d \end{array} \right] \right) \\
& \left(\left[\begin{array}{cc} [G_{11} & G_{1N}]^{bb} & [G_{12} & G_{13} & \cdots & G_{1(N-1)}]^{bd} \\ [G_{N1} & G_{NN}] & [G_{N2} & G_{N3} & \cdots & G_{N(N-1)}] \\ [G_{21} & G_{2N}]^{db} & [G_{22} & G_{23} & \cdots & G_{2(N-1)}]^{dd} \\ [G_{31} & G_{3N}] & [G_{32} & G_{33} & \cdots & G_{3(N-1)}] \\ \vdots & \vdots & \vdots & \vdots & \cdots & \vdots \\ \vdots & \vdots & \vdots & \vdots & \cdots & \vdots \\ G_{(N-1)1} & G_{(N-1)N} & G_{(N-1)2} & G_{(N-1)3} & \cdots & G_{(N-1)(N-1)} \end{array} \right] + \left[\begin{array}{c} \left\{ U_{r_{11}}^b \right\} \\ \left\{ U_{r_{21}}^b \right\} \\ U_{r_{11}}^d \\ U_{r_{21}}^d \\ \vdots \\ U_{r_{(N-2)1}}^d \end{array} \right] \right) \\
& = \left[\begin{array}{c} \left\{ C_{11}^b \right\} \\ \left\{ C_{21}^b \right\} \\ C_{11}^d \\ C_{21}^d \\ \vdots \\ \vdots \\ C_{(N-2)1}^d \end{array} \right]
\end{aligned}$$

(65)

The inertia matrices, \mathbf{S} , are as follows:

$$\mathbf{S} = \frac{\rho_o(\bar{v}^2 - 1)}{\bar{E}_o r_o^{(n_2 - n_1)}} \sum_{j=1}^M \int_{r_1^{(j)}}^{r_3^{(j)}} r^{(n_2 - n_1)} u_r^*(r, \xi_k) \left\{ \sum_{k=1}^3 N_k^{(j)}(r) \ddot{u}_r(r_k^{(j)}, t) \right\} dr \quad (66)$$

$$\mathbf{S} = \frac{\rho_o(\bar{v}^2 - 1)}{\bar{E}_o r_o^{(n_2 - n_1)}} \begin{bmatrix} h_1^{k(j)} & h_2^{k(j)} & h_3^{k(j)} \end{bmatrix} \begin{Bmatrix} \ddot{u}_r^{(j)}(r_1, t) \\ \ddot{u}_r^{(j)}(r_2, t) \\ \ddot{u}_r^{(j)}(r_3, t) \end{Bmatrix} \quad (67)$$

However, the boundary nodes i.e. $\xi_k = (r_i, r_o)$, $k = (1, N)$, and the domain nodes i.e.

$$\xi_k = (r_i + l, r_i + 2l, \dots, r_i + (N-1)l), \quad k = (2, 3, \dots, N-1).$$

Expressions of the matrices \mathbf{S}^{ij} are:

$$\mathbf{S}^{bb} = C_o \begin{bmatrix} h_1^{11} & h_3^{1M} \\ h_1^{N1} & h_3^{NM} \end{bmatrix}, \quad (68)$$

$$\mathbf{S}^{bd} = C_o \begin{bmatrix} h_2^{11} & h_3^{11} + h_1^{12} & \dots & h_3^{1(M-1)} + h_1^{1M} & h_2^{1M} \\ h_2^{N1} & h_3^{N1} + h_1^{N2} & \dots & h_3^{N(M-1)} + h_1^{NM} & h_2^{NM} \end{bmatrix}, \quad (69)$$

$$\mathbf{S}^{db} = C_o \begin{bmatrix} h_1^{21} & h_3^{2M} \\ h_1^{31} & h_3^{3M} \\ \vdots & \vdots \\ h_1^{(N-1)1} & h_3^{(N-1)M} \end{bmatrix}, \quad (70)$$

$$\mathbf{S}^{dd} = C_o \begin{bmatrix} h_2^{21} & h_3^{21} + h_1^{22} & \dots & h_3^{2(M-1)} + h_1^{2M} & h_2^{2M} \\ h_2^{31} & h_3^{31} + h_1^{32} & \dots & h_3^{3(M-1)} + h_1^{3M} & h_2^{3M} \\ \vdots & \vdots & \vdots & \vdots & \vdots \\ h_2^{(N-1)1} & h_3^{(N-1)1} + h_1^{(N-1)2} & \dots & h_3^{(N-1)(M-1)} + h_1^{(N-1)M} & h_2^{(N-1)M} \end{bmatrix}, \quad (71)$$

$$C_o = \frac{\rho_o(\bar{v}^2 - 1)}{\bar{E}_o r_o^{(n_2 - n_1)}}, \quad (72)$$

where h_k^{ij} are defined in the Appendix. Sizes of the matrices \mathbf{S}^{bb} , \mathbf{S}^{bd} , \mathbf{S}^{db} , and \mathbf{S}^{dd} are respectively, 2×2 , $2 \times (N-2)$, $(N-2) \times 2$, and $(N-2) \times (N-2)$.

\mathbf{H}^{bb} and \mathbf{H}^{bd} are sub-matrices of the boundary conditions and, they are related to the boundary points, whereas the sub-matrix \mathbf{H}^{dd} is related to the internal nodes.

However, the matrices \mathbf{H}^{ij} are given by:

$$\mathbf{H}^{bb} = \begin{bmatrix} 2 & \frac{n_1+1-\bar{v}}{r_o} u_r^*(r_o, r_i) - \frac{du_r^*(r_o, r_i)}{dr} \\ \frac{\bar{v}-(n_1+1)}{r_i} u_r^*(r_i, r_o) + \frac{du_r^*(r_i, r_o)}{dr} & 0 \end{bmatrix}, \quad (73)$$

$$\mathbf{H}^{db} = \begin{bmatrix} \frac{\bar{v}-(n_1+1)}{r_i} u_r^*(r_i, \xi_2) + \frac{du_r^*(r_i, \xi_2)}{dr} & \frac{n_1+1-\bar{v}}{r_o} u_r^*(r_o, \xi_2) - \frac{du_r^*(r_o, \xi_2)}{dr} \\ \vdots & \vdots \\ \frac{\bar{v}-(n_1+1)}{r_i} u_r^*(r_i, \xi_{N-1}) + \frac{du_r^*(r_i, \xi_{N-1})}{dr} & \frac{n_1+1-\bar{v}}{r_o} u_r^*(r_o, \xi_{N-1}) - \frac{du_r^*(r_o, \xi_{N-1})}{dr} \end{bmatrix}, \quad (74)$$

$$\mathbf{H}^{dd} = \begin{bmatrix} 1 & 0 & \cdots & 0 \\ 0 & 1 & \cdots & 0 \\ \vdots & \vdots & \ddots & \vdots \\ 0 & 0 & \cdots & 1 \end{bmatrix}, \quad (75)$$

where the matrices \mathbf{H}^{bb} , \mathbf{H}^{db} , and \mathbf{H}^{dd} are of sizes (2×2) , $(N-2) \times 2$, and $(N-2) \times (N-2)$, respectively.

The following domain integrals are numerically solved as follows:

$$\mathbf{G} = \sum_{j=1}^M \int_{r_1^{(j)}}^{r_3^{(j)}} \left(\frac{n_1+1}{r^2} u_r^*(r, \xi) - 2 \frac{n_1+1}{r} \frac{\partial u_r^*(r, \xi_k)}{\partial r} \right) \left\{ \sum_{k=1}^3 N_k^{(j)}(r) u_r \left(r_k^{(j)}, t \right) \right\} dr \quad (76)$$

Where,

$$\mathbf{G}_1 = \sum_{j=1}^M \int_{r_1^{(j)}}^{r_3^{(j)}} \left(\frac{n_1+1}{r^2} u_r^*(r, \xi_k) \right) \left\{ \sum_{k=1}^3 N_k^{(j)}(r) u_r(r_k^{(j)}, t) \right\} dr \quad (77)$$

$$\mathbf{G}_2 = \sum_{j=1}^M \int_{r_1^{(j)}}^{r_3^{(j)}} \left(2 \frac{n_1+1}{r} \frac{\partial u_r^*(r, \xi)}{\partial r} \right) \left\{ \sum_{k=1}^3 N_k^{(j)}(r) u_r(r_k^{(j)}, t) \right\} dr \quad (78)$$

$$\mathbf{G} = \mathbf{G}_1 + \mathbf{G}_2 \quad (79)$$

The matrices \mathbf{G}^{ij} , produced by domain integral equation, are expressed as follows:

$$\mathbf{G}^{bb} = C_1 \begin{bmatrix} m_1^{11} + 2b_1^{11} & m_3^{1M} + 2b_3^{1M} \\ m_1^{N1} + 2b_1^{N1} & m_3^{NM} + 2b_3^{NM} \end{bmatrix}, \quad (80)$$

$$\mathbf{G}^{bd} = C_1 \begin{bmatrix} m_2^{11} + 2b_2^{11} & (m_3^{11} + 2b_3^{11} + m_1^{12} + 2b_1^{12}) & \dots & (m_3^{1(M-1)} + 2b_3^{1(M-1)} + m_1^{1M} + 2b_1^{1M}) & m_2^{1M} + 2b_2^{1M} \\ m_2^{N1} + 2b_2^{N1} & (m_3^{N1} + 2b_3^{N1} + m_1^{N2} + 2b_1^{N2}) & \dots & (m_3^{N(M-1)} + 2b_3^{N(M-1)} + m_1^{NM} + 2b_1^{NM}) & m_2^{NM} + 2b_2^{NM} \end{bmatrix}, \quad (81)$$

$$\mathbf{G}^{db} = C_1 \begin{bmatrix} m_1^{21} + 2b_1^{21} & m_3^{2M} + 2b_3^{2M} \\ m_1^{31} + 2b_1^{31} & m_3^{3M} + 2b_3^{3M} \\ \vdots & \vdots \\ m_1^{(N-1)1} + 2b_1^{(N-1)1} & m_3^{(N-1)M} + 2b_3^{(N-1)M} \end{bmatrix}, \quad (82)$$

$$\mathbf{G}^{dd} = C_1 \begin{bmatrix} m_2^{21} + 2b_2^{21} & (m_3^{21} + 2b_3^{21} + m_1^{22} + 2b_1^{22}) & \dots & (m_3^{2(M-1)} + 2b_3^{2(M-1)} + m_1^{2M} + 2b_1^{2M}) & m_2^{2M} + 2b_2^{2M} \\ m_2^{31} + 2b_2^{31} & (m_3^{31} + 2b_3^{31} + m_1^{32} + 2b_1^{32}) & \dots & (m_3^{3(M-1)} + 2b_3^{3(M-1)} + m_1^{3M} + 2b_1^{3M}) & m_2^{3M} + 2b_2^{3M} \\ \vdots & \vdots & \dots & \vdots & \vdots \\ m_2^{(N-1)1} + 2b_2^{(N-1)1} & (m_3^{(N-1)1} + 2b_3^{(N-1)1} + m_1^{(N-1)2} + 2b_1^{(N-1)2}) & \dots & (m_3^{(N-1)(M-1)} + 2b_3^{(N-1)(M-1)} + m_1^{(N-1)M} + 2b_1^{(N-1)M}) & m_2^{(N-1)M} + 2b_2^{(N-1)M} \end{bmatrix}, \quad (83)$$

where $C_1 = n_1 + 1$. The matrices \mathbf{G}^{bb} , \mathbf{G}^{bd} , \mathbf{G}^{db} , and \mathbf{G}^{dd} are of sizes 2×2 , $2 \times (N-2)$, $(N-2) \times 2$, and $(N-2) \times (N-2)$.

The expressions of m_i^{jk} and b_i^{jk} are provided in the Appendix.

Moreover, the right-hand side load vectors \mathbf{C}^b and \mathbf{C}^d are found as:

$$\mathbf{C}^b = \begin{bmatrix} -\frac{1-\bar{v}^2}{\bar{E}_i} u_r^*(r_i, r_o) P_i(t) \\ \frac{1-\bar{v}^2}{\bar{E}_o} u_r^*(r_o, r_i) P_o(t) \end{bmatrix}, \quad (84)$$

$$\mathbf{C}^d = \begin{bmatrix} -\frac{1-\bar{v}^2}{\bar{E}_i} u_r^*(r_i, \xi_2) P_i(t) + \frac{1-\bar{v}^2}{\bar{E}_o} u_r^*(r_o, \xi_2) P_o(t) \\ -\frac{1-\bar{v}^2}{\bar{E}_i} u_r^*(r_i, \xi_3) P_i(t) + \frac{1-\bar{v}^2}{\bar{E}_o} u_r^*(r_o, \xi_3) P_o(t) \\ \vdots \\ -\frac{1-\bar{v}^2}{\bar{E}_i} u_r^*(r_i, \xi_{N-1}) P_i(t) + \frac{1-\bar{v}^2}{\bar{E}_o} u_r^*(r_o, \xi_{N-1}) P_o(t) \end{bmatrix}. \quad (85)$$

3.3.1 Time Marching with the Houbolt Method

Houbolt's method is utilized as a time marching in the numerical solution of the temporal system of ordinary differential equations stated by Eq. (60). The method is implicit, unconditionally stable; and built on the cubic Lagrange interpolation of the temporal variable $u_r(r, t)$ from time $t_{m-2} = 2\Delta t$ to time $t_{m+1} = (m+1)\Delta t$ [43].

In Houbolt's time marching scheme, the velocity and acceleration are given by the following formulae:

$$\dot{u}_{r_{m+1}}(t) = \frac{1}{6\Delta t} (11u_{r_{m+1}} - 18u_{r_m} + 9u_{r_{m-1}} - 2u_{r_{m-2}}), \quad (86)$$

$$\ddot{u}_{r_{m+1}}(t) = \frac{1}{(\Delta t)^2} (2u_{r_{m+1}} - 5u_{r_m} + 4u_{r_{m-1}} - u_{r_{m-2}}). \quad (87)$$

Using these formulas in combination with eqn. (60) will result in:

$$\begin{bmatrix} \mathbf{A}^{bb} & \mathbf{A}^{bd} \\ \mathbf{A}^{db} & \mathbf{A}^{dd} \end{bmatrix} \begin{bmatrix} \mathbf{u}_{r_{m+1}}^b \\ \mathbf{u}_{r_{m+1}}^d \end{bmatrix} - \frac{1}{(\Delta t)^2} \begin{bmatrix} \mathbf{S}^{bb} & \mathbf{S}^{bd} \\ \mathbf{S}^{db} & \mathbf{S}^{dd} \end{bmatrix} \begin{bmatrix} \mathbf{g}_{m+1}^b \\ \mathbf{g}_{m+1}^d \end{bmatrix} = \begin{bmatrix} \mathbf{C}^b \\ \mathbf{C}^d \end{bmatrix}, \quad (88)$$

$$\mathbf{A}^{bb} = \mathbf{H}^{bb} + \mathbf{G}^{bb} - \frac{2}{(\Delta t)^2} \mathbf{S}^{bb}, \quad (89)$$

$$\mathbf{A}^{bd} = \mathbf{G}^{bd} - \frac{2}{(\Delta t)^2} \mathbf{S}^{bd}, \quad (90)$$

$$\mathbf{A}^{db} = \mathbf{H}^{db} + \mathbf{G}^{db} - \frac{2}{(\Delta t)^2} \mathbf{S}^{db}, \quad (91)$$

$$\mathbf{A}^{dd} = \mathbf{H}^{dd} + \mathbf{G}^{dd} - \frac{2}{(\Delta t)^2} \mathbf{S}^{dd}. \quad (92)$$

The vectors \mathbf{g}_{m+1}^b and \mathbf{g}_{m+1}^d are expressed as:

$$\mathbf{g}_{m+1}^b = \begin{bmatrix} -5u_r(r_i, t_m) + 4u_r(r_i, t_{m-1}) - u_r(r_i, t_{m-2}) \\ -5u_r(r_o, t_m) + 4u_r(r_o, t_{m-1}) - u_r(r_o, t_{m-2}) \end{bmatrix}, \quad (93)$$

$$\mathbf{g}_{m+1}^d = \begin{bmatrix} -5u_r(r_i + l, t_m) + 4u_r(r_i + l, t_{m-1}) - u_r(r_i + l, t_{m-2}) \\ -5u_r(r_i + 2l, t_m) + 4u_r(r_i + 2l, t_{m-1}) - u_r(r_i + 2l, t_{m-2}) \\ \vdots \\ -5u_r(r_i + (N-1)l, t_m) + 4u_r(r_i + (N-1)l, t_{m-1}) - u_r(r_i + (N-1)l, t_{m-2}) \end{bmatrix}. \quad (94)$$

Obviously, the time marching using Houbolt's method requires the calculations of u_{r-1} and u_{r-2} to start the computations for each time step.

Therefore, to determine u_{r-1} , \dot{u}_{r0} is computed using the forward and backward finite difference at time $t = 0$

$$\dot{u}_{r0} = \frac{u_{r1} - u_{r0}}{\Delta t} = \frac{u_{r0} - u_{r-1}}{\Delta t} \quad (95)$$

Then from eqn. (95), we get:

$$u_{r-1} = 2u_{r0} - u_{r1}, \quad (96)$$

Similarly, to determine u_{r-2} , \dot{u}_{r-1} is computed using the forward and backward finite difference at time $t = -\Delta t$

$$\dot{u}_{r-1} = \frac{u_{r0} - u_{r-1}}{\Delta t} = \frac{u_{r-1} - u_{r-2}}{\Delta t} \quad (97)$$

Then from eqn. (97), we get:

$$u_{r-2} = 2u_{r-1} - u_{r0} \quad (98)$$

Therefore, substituting eqn. (95) into eqn. (97), we get:

$$u_{r-2} = 2(2u_{r0} - u_{r1}) - u_{r0} = 3u_{r0} - 2u_{r1} \quad (99)$$

Moreover, when the radial displacement is calculated as a function of time, the distributions of radial and circumferential stresses are calculated by using the constitutive relations. This computation needs the calculation of the r - derivative of the radial displacement, u_r . Thus, the required r - derivatives are determined by the use of the finite difference method.

For the radial stress:

$$\sigma_r(r, t) = \frac{\bar{E}(r)}{1 - \bar{\nu}^2} \left(\frac{\partial u_r(r, t)}{\partial r} + \bar{\nu} \frac{u_r(r, t)}{r} \right) \quad (100)$$

$$\begin{bmatrix} \sigma_r(r_i, t_{m+1}) \\ \sigma_r(r_i + l, t_{m+1}) \\ \vdots \\ \sigma_r(r_i + (N-1)l, t_{m+1}) \\ \sigma_r(r_o, t_{m+1}) \end{bmatrix} = \frac{1}{1 - \bar{\nu}^2} \begin{bmatrix} \bar{E}(r_i) \\ \bar{E}(r_i + l) \\ \vdots \\ \bar{E}(r_i + (N-1)l) \\ \bar{E}(r_o) \end{bmatrix} \left[\begin{bmatrix} \frac{du_r(r_i, t_{m+1})}{dr} \\ \frac{du_r(r_i + l, t_{m+1})}{dr} \\ \vdots \\ \frac{du_r(r_i + (N-1)l, t_{m+1})}{dr} \\ \frac{du_r(r_o, t_{m+1})}{dr} \end{bmatrix} + \bar{\nu} \begin{bmatrix} \frac{u_r(r_i, t_{m+1})}{r_i} \\ \frac{u_r(r_i + l, t_{m+1})}{r_i + l} \\ \vdots \\ \frac{u_r(r_i + (N-1)l, t_{m+1})}{r_i + (N-1)l} \\ \frac{u_r(r_o, t_{m+1})}{r_o} \end{bmatrix} \right] \quad (101)$$

For the calculation of the derivatives of the radial displacement (radial strain), the finite difference is used. The radial strain of boundary points is found by forward and backward difference for the inner radius and outer radius, respectively. Whereas for the domain nodes; the central difference is performed to find the radial strain, as follows:

$$\begin{bmatrix} \frac{du_r(r_i)}{dr} \\ \frac{du_r(r_i + l)}{dr} \\ \vdots \\ \frac{du_r(r_i + (N-1)l)}{dr} \\ \frac{du_r(r_o)}{dr} \end{bmatrix} = \begin{bmatrix} \frac{u_r(r_i + l) - u_r(r_i)}{l} \\ \frac{u_r(r_i + 2l) - u_r(r_i)}{2l} \\ \vdots \\ \frac{u_r(r_i + kl) - u_r(r_i + (k-2)l)}{2l} \\ \frac{u_r(r_o) - u_r(r_i + (N-2)l)}{l} \end{bmatrix} \quad (102)$$

Where,

$k = (2, 3, \dots, N-1)$, for the domain nodes.

For the tangential (hoop) stress:

$$\sigma_\theta(r, t) = \frac{\bar{E}(r)}{1 - \bar{\nu}^2} \left(\frac{u_r(r, t)}{r} + \bar{\nu} \frac{\partial u_r(r, t)}{\partial r} \right) \quad (103)$$

$$\begin{bmatrix} \sigma_\theta(r_i, t_{m+1}) \\ \sigma_\theta(r_i + l, t_{m+1}) \\ \vdots \\ \sigma_\theta(r_i + (N-1)l, t_{m+1}) \\ \sigma_\theta(r_o, t_{m+1}) \end{bmatrix} = \frac{1}{1 - \bar{\nu}^2} \begin{bmatrix} \bar{E}(r_i) \\ \bar{E}(r_i + l) \\ \vdots \\ \bar{E}(r_i + (N-1)l) \\ \bar{E}(r_o) \end{bmatrix} \left(\begin{bmatrix} \frac{u_r(r_i, t_{m+1})}{r_i} \\ \frac{u_r(r_i + l, t_{m+1})}{r_i + l} \\ \vdots \\ \frac{u_r(r_i + (N-1)l, t_{m+1})}{r_i + (N-1)l} \\ \frac{u_r(r_o, t_{m+1})}{r_o} \end{bmatrix} + \bar{\nu} \begin{bmatrix} \frac{du_r(r_i, t_{m+1})}{dr} \\ \frac{du_r(r_i + l, t_{m+1})}{dr} \\ \vdots \\ \frac{du_r(r_i + (N-1)l, t_{m+1})}{dr} \\ \frac{du_r(r_o, t_{m+1})}{dr} \end{bmatrix} \right) \quad (104)$$

The calculation of the radial strain is the same as in eqn. (102).

CHAPTER 4

VERIFICATION OF THE METHOD

4.1 First Comparison

To validate the numerical solution developed by D-BEM, a functionally graded material thick-walled cylinder with the inner radius r_i and outer radius r_o , as shown in fig. (6), is subjected to different uniformly-distributed dynamic pressures at the inner boundary surface, in order to compare it to the work of Nikkhah et al. [24].

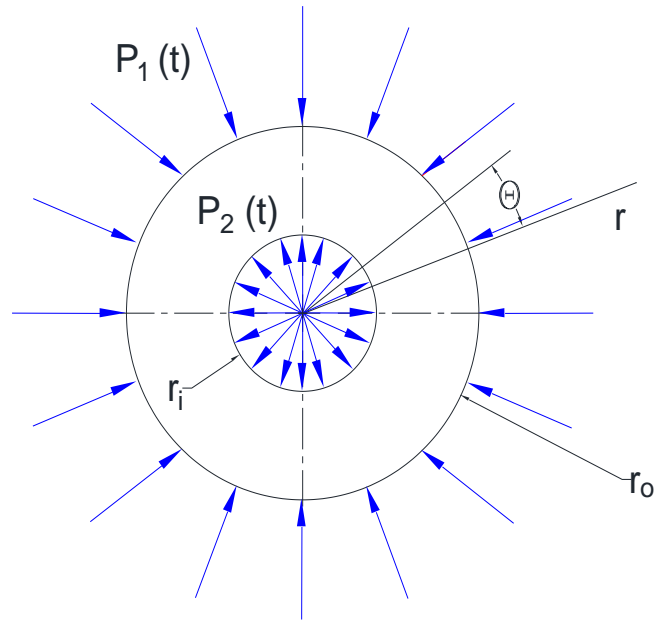


Figure 6: Cross-section of the FGM thick-walled cylinder with the boundary conditions.

The material properties of the cylinder vary through the thickness according to the power law volume fraction function eqn. (1).

However, Poisson's ratio is considered to be constant, $\nu = 0.3$. For controlling the material properties of the FGM cylinder through the thickness, the exponents of the

power law function for the modulus of elasticity and the mass density are considered as follows:

$$E = E_o (r / r_o)^{n_1}, \quad \rho = \rho_o (r / r_o)^{n_2} \quad (105)$$

The boundary and initial conditions of the thick-walled FGM cylinder are expressed as: $\sigma_r(r_i, t) = -P_1(t)$, $\sigma_r(r_o, t) = -P_2(t)$. (106)

$$u_r(r, 0) = u_{r_0}(r) = 0, \quad \dot{u}_r(r, 0) = \dot{u}_{r_0}(r) = 0. \quad (107)$$

Where, $\sigma_r(r, t)$, $u_{r_0}(r)$ and $\dot{u}_{r_0}(r)$ are the radial stress, the initial radial displacement, and the initial radial velocity, respectively.

The FGM thick-walled cylinder geometry and, mechanical properties are proposed, as shown in table (1).

Property	Inner Edge	Outer Edge
First Comparison		
Material	Aluminum	Ceramic Alumina
Radius (m)	$r_i = 1$	$r_o = 1.2$
Elastic Modulus, $E(GPa)$	70	380
Density, $\rho (\frac{kg}{m^3})$	2700	3800
Poisson Ratio, ν	0.3	0.3

Table 1: Thick-walled cylinder geometry and mechanical properties [24].

4.1.1 Dynamic Loadings

The studied FGM thick-walled cylinder is subjected to various internal dynamic pressures, as follows:

1. The inner surface of the FGM cylinder is subjected to a uniformly-distributed short-time ramp pressure, figure (7), which can be expressed as:

$$P_2(t) = \begin{cases} P^* t & 0 < t \leq t_0 \\ 0 & t > t_0 \end{cases} \quad \text{and,} \quad (108)$$

$$P_1(t) = 0$$

Where, P^* and t_0 are taken as 4 GPa/s and 0.005 s, respectively.

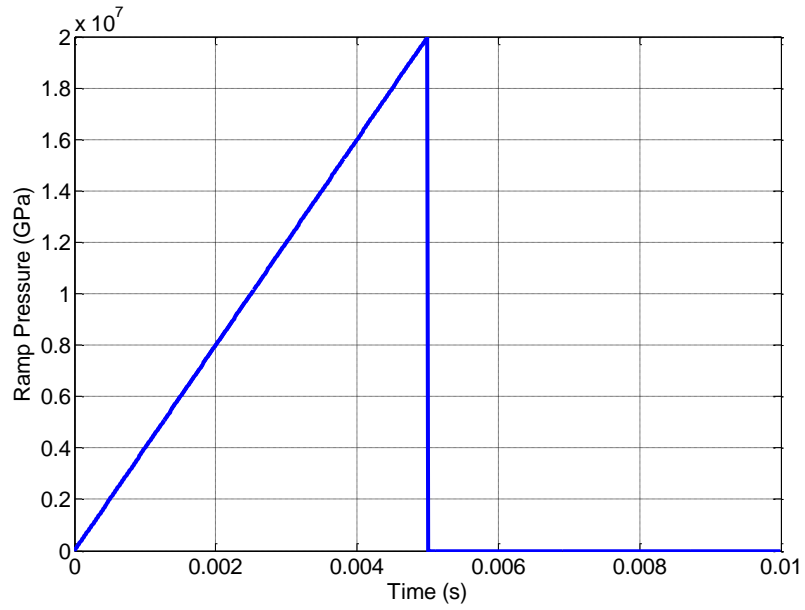


Figure 7: The variation of the internal ramp pressure with time proposed.

2. The inner boundary surface is subjected to an exponential dynamic pressure imposed uniformly, as shown in figure (8). The non-dimensional time histories of the imposed pressures at the inner and outer boundary surfaces can be expressed as:

$$P_1(\tau) = 0.001(1 - e^{-C_o\tau}) \quad \text{and,} \quad (109)$$

$$P_2(\tau) = 0$$

Where, C_o is a constant equal to 0.1, and the following non-dimensional parameters are introduced:

$$\bar{u} = \frac{u}{r_o}, \quad \tau = \frac{C_v}{r_o} \quad \text{and,} \quad C_v = \sqrt{\frac{C_{10}}{\rho_o}}. \quad (110)$$

Where, $C_{10} = 511.54 \text{ GPa}$

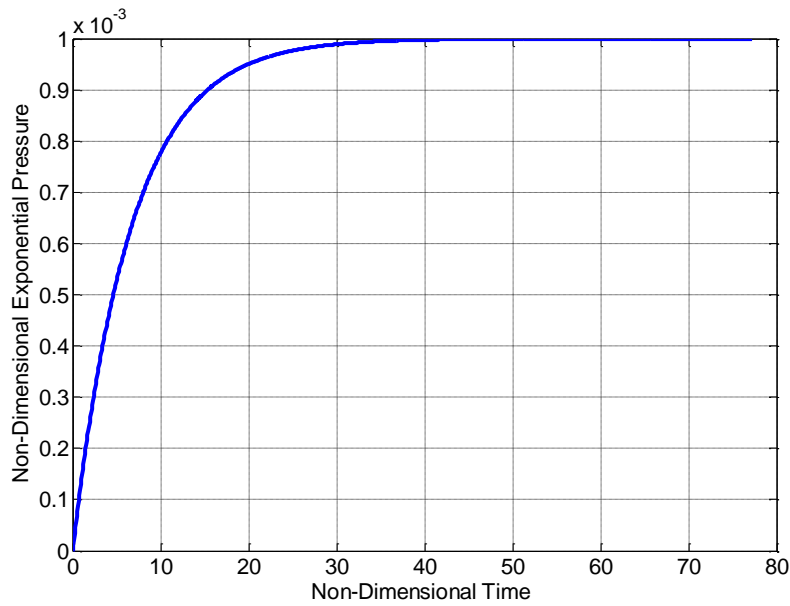


Figure 8: The variation of the internal non-dimensional exponential pressure with non-dimensional time proposed for verification.

4.1.1.1 Ramp Dynamic Loading Results and Comparison

Time histories of the radial displacement at the middle point of the thickness for various values of power law exponents are calculated and, a comparison is made for each case with the results obtained by using D-BEM method, as shown in figures (9, 10 and 11). However, all the results obtained, with various material indices, by D-BEM are plotted in figure (12) to show the effect of the material property index.

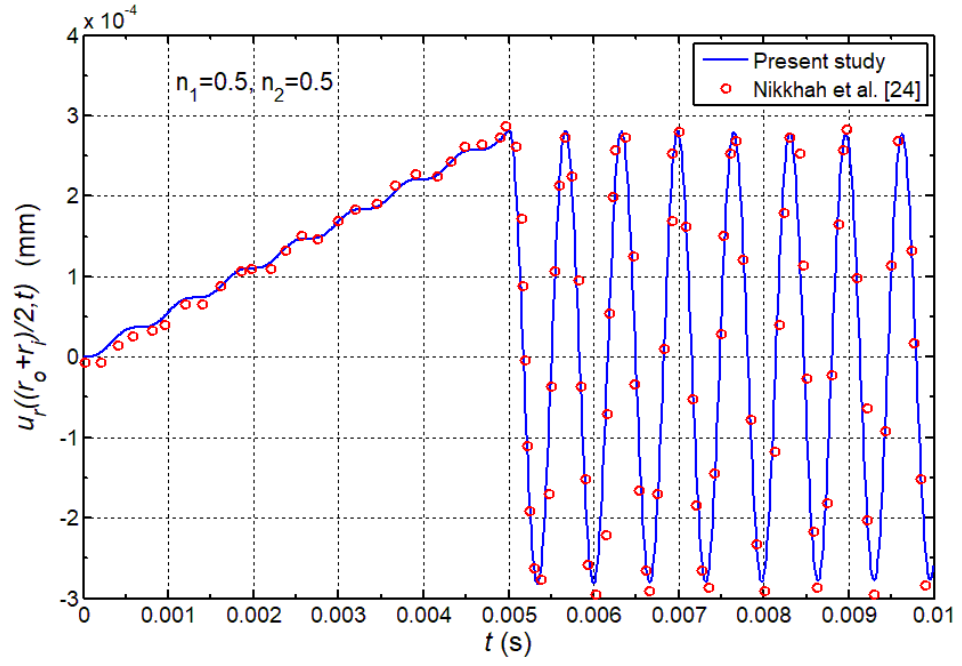


Figure 9: Time history of radial displacement at midpoint with $n_1 = n_2 = 0.5$.

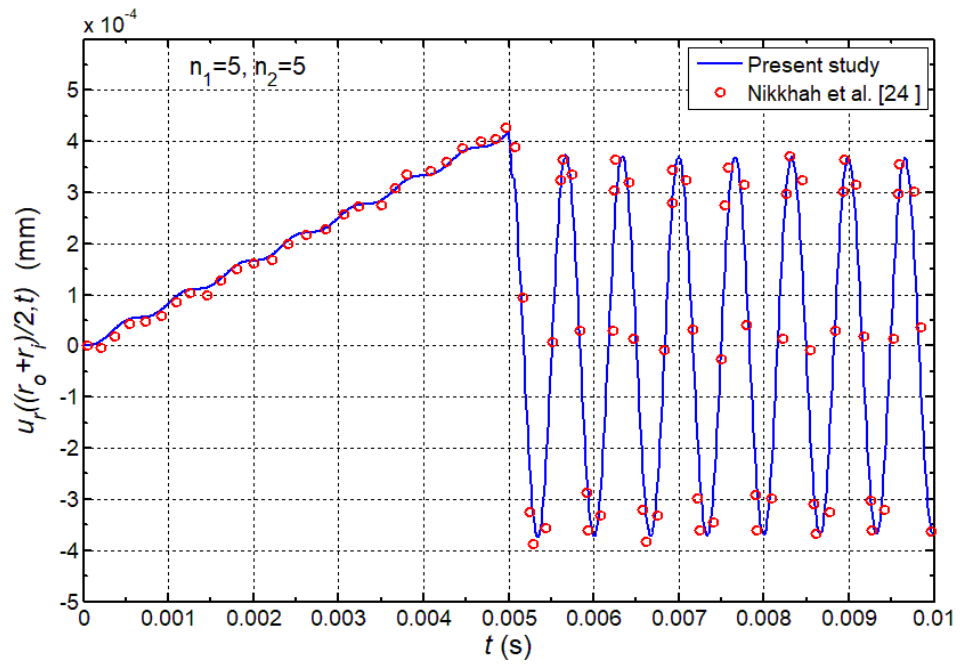


Figure 10: Time history of radial displacement at midpoint with $n_1 = n_2 = 5$.

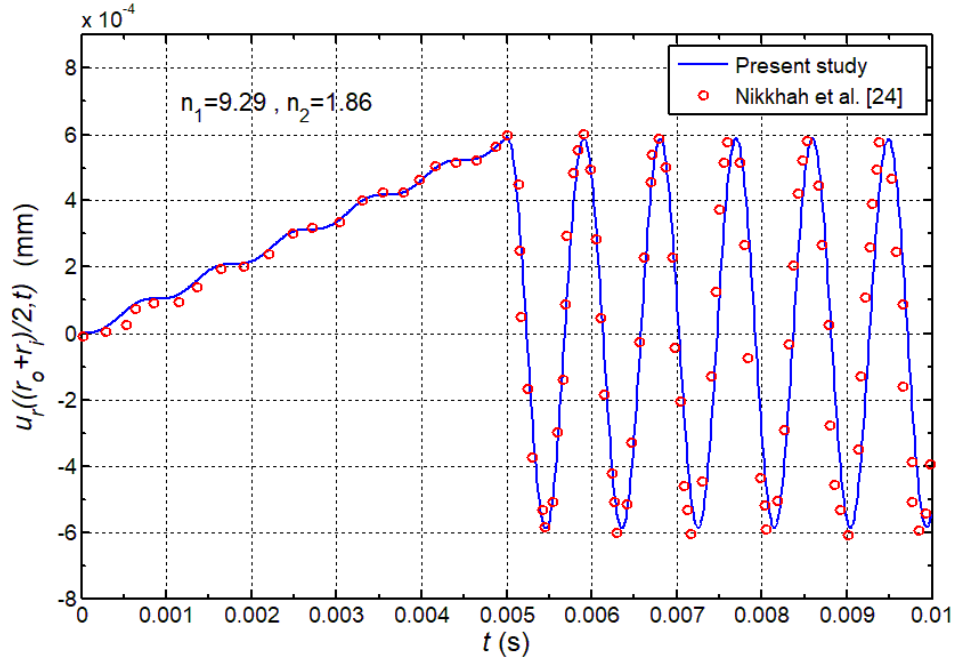


Figure 11: Time history of radial displacement at midpoint with $n_1 = 9.29$, $n_2 = 1.86$.

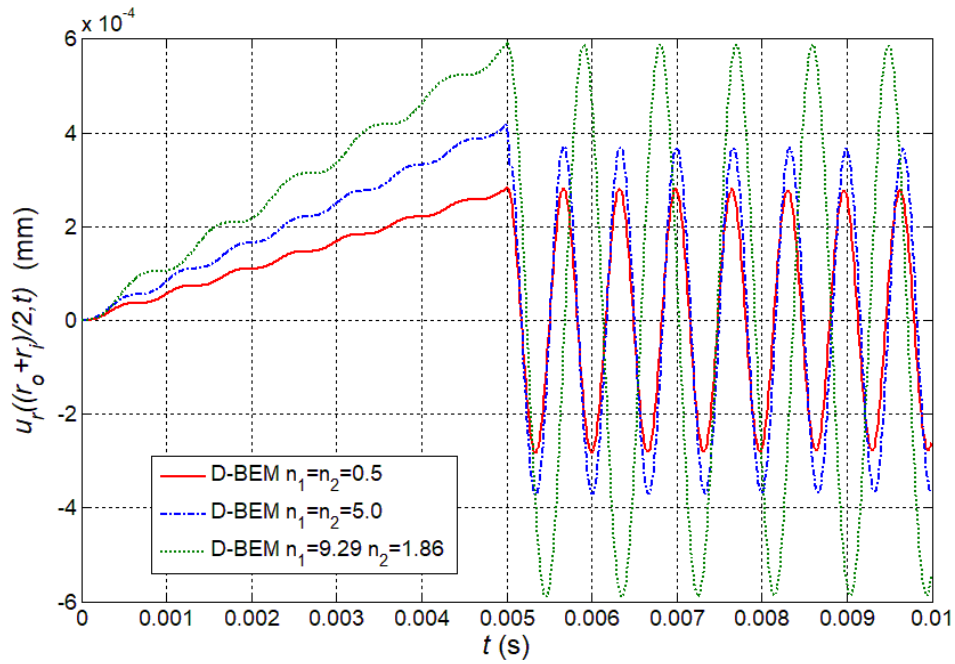


Figure 12: Time history of radial displacement at midpoint with different material property indices by using D-BEM.

Furthermore, circumferential stress result at midpoint for material property exponents $n_1 = n_2 = 5.0$. has been calculated and compared to the results obtained from the

research work of Nikkhah et al. [24]. It is clearly evident that the results obtained by using D-BEM are congruent with the compared ones, as shown in figure (13).

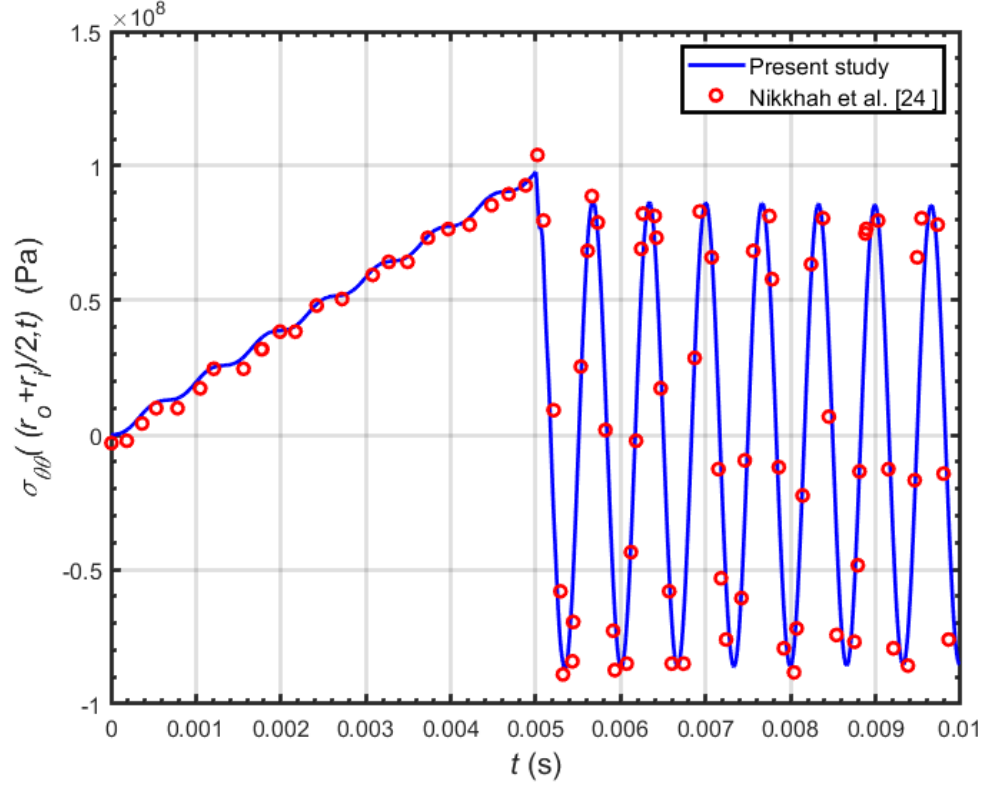


Figure 13: Time history of circumferential stress at midpoint with $n_1 = n_2 = 5.0$.

4.1.1.2 Exponential Dynamic Loading Results and Comparison

Using an exponential non-dimensional dynamic pressure imposed uniformly at the inner boundary surface of the FGM thick-walled cylinder with inner radius $r_i = 1.0$ and outer radius of the cylinder $r_o = 1.5$.

Time histories of the non-dimensional radial displacement at the middle point of thickness of the thick-walled hollow FGM cylinder with material properties index, $n_1 = n_2 = 0.5$, are obtained using D-BEM and compared to the results of reference paper Nikkhah et al. [24], as shown in figures (14). The result obtained shows a consistency with those of the reference.

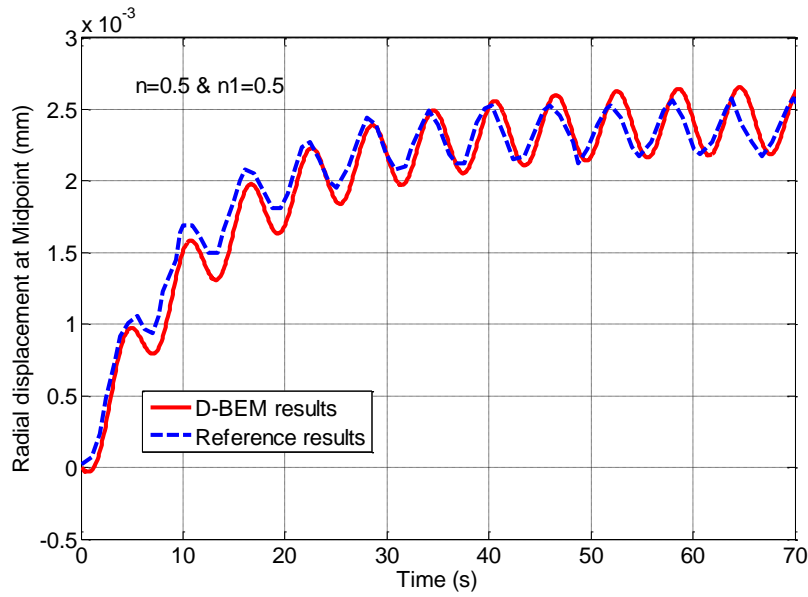


Figure 14: Time history of non-dimensional radial displacement at midpoint with $n_1 = n_2 = 0.5$

4.2 Second Comparison

This study is to investigate the exact free and forced vibrations behavior of FGM thick-walled cylinders under dynamic internal pressure, Keles and Tutuncu [57].

Consider a thick-walled hollow cylinder of inner radius, a , and outer radius, ka , where k is a constant, figure (15).

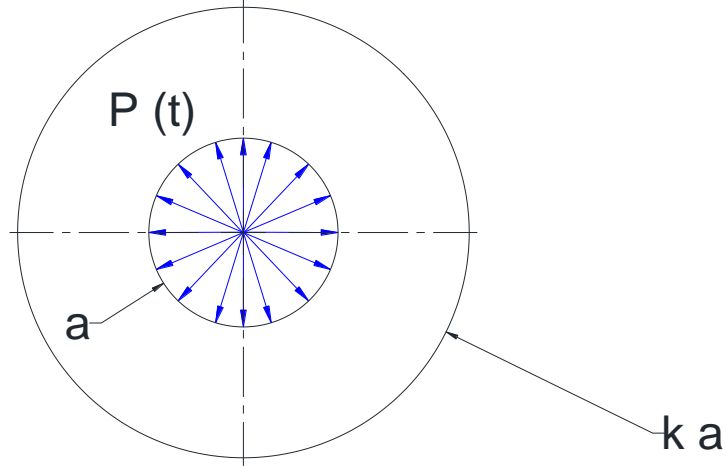


Figure 15: Schematic diagram of the boundary conditions and geometry of FGM thick-walled cylinder

4.2.1 Formulation of the problem

A different formulation is used here to study the dynamic response of the FGM thick-walled cylinder. Under axisymmetric conditions the strain-displacement relations in polar coordinates are found by equations (11 and 12).

However, the constitutive linear relations are:

$$\sigma_{rr} = \frac{E}{1-\bar{\nu}^2} \varepsilon_{rr} + \frac{E\bar{\nu}}{1-\bar{\nu}^2} \varepsilon_{\theta\theta} \quad (111)$$

$$\sigma_{\theta\theta} = \frac{E\bar{\nu}}{1-\bar{\nu}^2} \varepsilon_{rr} + \frac{E}{1-\bar{\nu}^2} \varepsilon_{\theta\theta} \quad (112)$$

Or,

$$\sigma_{rr} = C_{11}\varepsilon_{rr} + C_{12}\varepsilon_{\theta\theta} \quad (113)$$

$$\sigma_{\theta\theta} = C_{12}\varepsilon_{rr} + C_{22}\varepsilon_{\theta\theta} \quad (114)$$

Where,

C_{11} and C_{22} refer to stiffness in the radial and circumferential directions, respectively whereas, C_{12} includes the Poisson's ratio effect.

Thus, for the axisymmetric non-rotating problem, the elasto-dynamic equation of motion is as follows:

$$\frac{\partial \sigma_{rr}}{\partial r} + \frac{\sigma_{rr} - \sigma_{\theta\theta}}{r} = \rho \frac{\partial^2 u_r(r, t)}{\partial t^2} \quad (115)$$

Substituting the stresses and the strain relations and simplifying, the governing elastodynamic equation of motion becomes:

$$r^2 \frac{\partial^2 u_r}{\partial r^2} + r m_1 \frac{\partial u_r}{\partial r} + m_2 u_r = \frac{r^2}{C^2} \frac{\partial^2 u_r}{\partial t^2} \quad (116)$$

Where,

$$C^2 = \frac{C_{11}}{\rho} \quad (117)$$

$$m_1 = \beta + 1, \quad m_2 = \frac{\nu \beta}{(1 - \nu)} - 1 \quad (118)$$

ρ : The material density.

Two cases are considered for the comparison with this reference work. The first case, the value of β is taken to be zero.

Thus,

$$m_1 = 1, \quad m_2 = -1 \quad (119)$$

Hence, substituting eqn. (119) in eqn. (116), the governing equation of motion resulted is the same as the one obtained in the Research Methodology chapter eqn. (20) for the homogenous case.

The second case, the value of β is taken as 2. This is the same as considering the material exponents $n_1 = n_2 = 2.0$ in eqn. (20).

The boundary conditions, with inner dynamic exponential pressure $P(t)$, are as follows:

$$\sigma_{rr}|_{r=a} = -P(t) \quad \sigma_{rr}|_{r=ka} = 0$$

4.2.2 Dynamic loadings

The non-dimensional exponential loading is used in this comparison:

$$P_2(\tau) = P(\tau) = P_o(1 - e^{-\gamma\tau}) \quad (120)$$

Where,

$$\tau = \frac{Ct}{u_{r_i}} \quad (121)$$

$$C_{11} = \frac{E_o(1-\nu)}{(1+\nu)(1-2\nu)}, \quad (122)$$

$$\gamma = 1.0 \quad (123)$$

The elastodynamic analysis is performed using D-BEM. The domain is divided into 20 isoparametric cells and the time step used for time marching by Houbolt's method is $\Delta t = 1 \times 10^{-5}$. The obtained dimensionless radial displacement at the inner surface, for both cases are plotted in figure (16) for comparison and, it shows a good consistency with the analytical solution developed by Keles and Tutuncu [50].

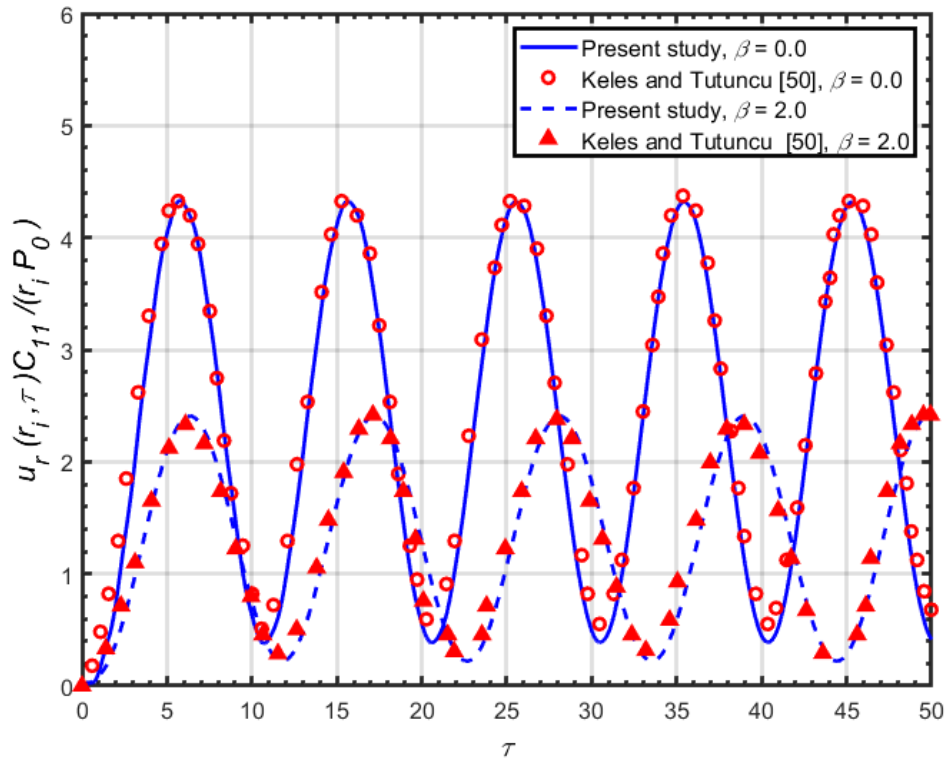


Figure 16: Comparisons of normalized radial displacements to the results given by Keles and Tütüncü [57] for $\beta = 0$ & 2.0 .

CHAPTER 5

NUMERICAL RESULTS

5.1 Composite thick-walled cylinder in plane stress condition.

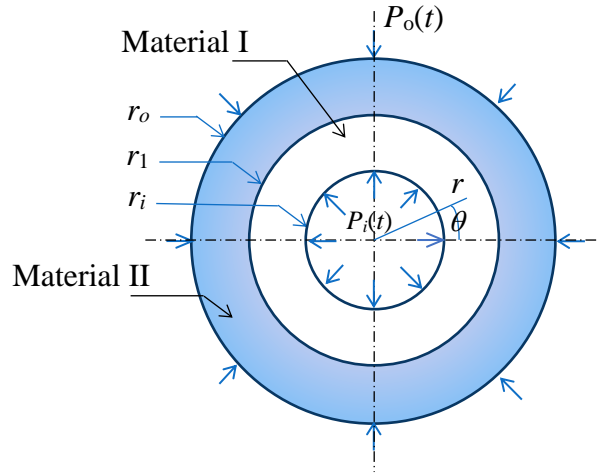


Figure 17: Composite thick-walled hollow cylinder under pressure shock loads

The composite thick-walled cylinder in plane stress is considered to validate the numerical solution obtained by using the D-BEM, as shown in figure (17). The domain is divided into M elements equals to 20 elements; that is 41 nodes, N . However, for the homogeneous part (Material I), the material indices, n_1 and n_2 are equal, whereas for the FGM part (Material II), the material indices are: $n_1 = 9.27$ and $n_2 = 1.87$.

Since the formulation is carried out in plane stress, thus; the Poisson's ratio and the elasticity modulus are as follows:

$$\bar{E}(r) = E(r) \quad \text{and} \quad \bar{\nu} = \nu \quad (124)$$

Therefore, the composite thick-walled cylinder geometry and, mechanical properties are proposed, as shown in table (2).

Material I	Aluminium	
Radius (m)	$r_i = 1$	
Elastic Modulus, $\bar{E} (GPa)$	70	
Density, $\rho (\frac{kg}{m^3})$	2700	
Material II	Aluminum	Ceramic Alumina
Radius (m)	$r_1 = 1.25$	$r_o = 1.5$
Elastic Modulus, $\bar{E} (GPa)$	70	380
Density, $\rho (\frac{kg}{m^3})$	2700	3800
Poisson Ratio, $\bar{\nu}$	0.3	0.3

Table 2: Composite thick-walled cylinder geometry and mechanical properties - plane stress

In this study, the composite hollow cylinder is subjected to uniformly-distributed internal shock ramp pressure as expressed in eqn. (108).

5.1.1 Radial displacement response results for plane stress

Different important points, along the depth of the wall, have been selected to show the radial response of the composite thick-walled cylinder under the ramp pressure shock applied. Therefore, the radial displacement response has been calculated for a time period of 0.01 second at the following positions:

1. Quarter depth point, at radius equals to 1.125 m.
2. At radius equals to 1.2 m.
3. Midpoint depth point, at radius equals to 1.25 m.
4. At radius equals to 1.3 m.
5. Three quarter depth point, at radius equals to 1.375 m.

For plane stress, the comparison of all the radial displacement responses at the positions selected above has been plotted, as shown in figure (18).

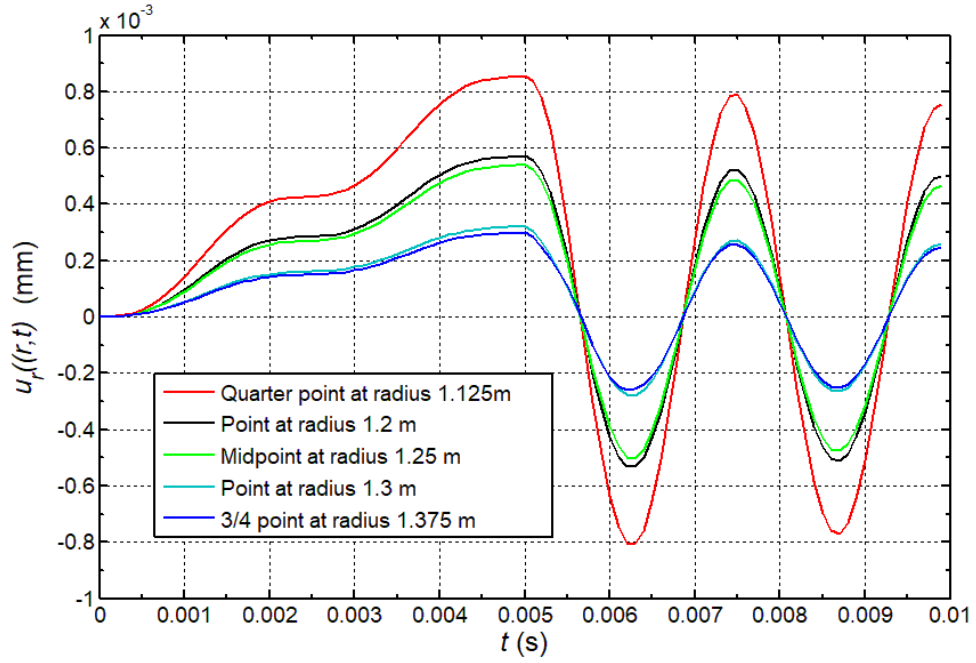


Figure 18: Comparison of various time history of radial displacement at different radii with $n_1 = 9.27$ & $n_2 = 1.87$.

5.1.2 Radial and circumferential stresses calculations for plane stress

To calculate the radial and hoop stresses, the displacement form of the constitutive equations is used:

For the radial stress:

For the tangential (hoop) stress:

5.1.2.1 Radial stress results for plane stress

Different positions at the wall thickness of the cylinder has been selected (quarter point, midpoint and $\frac{3}{4}$ point of the thickness). The radial stress responses at these selected points for a time period of 0.01s have been plotted in figure (19).

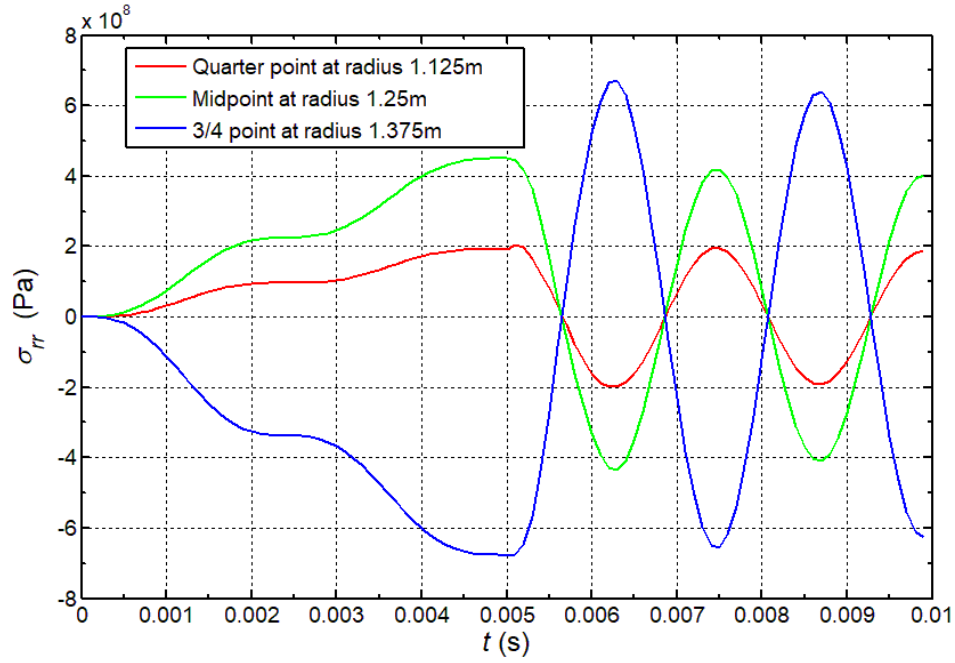


Figure 19: Comparison of radial stress at various points of wall thickness

5.1.2.2 Hoop stress results for plane stress

Similarly, the responses of circumferential stress at the same selected points at the wall thickness have been plotted in figure (20) for the same time period of 0.01s.

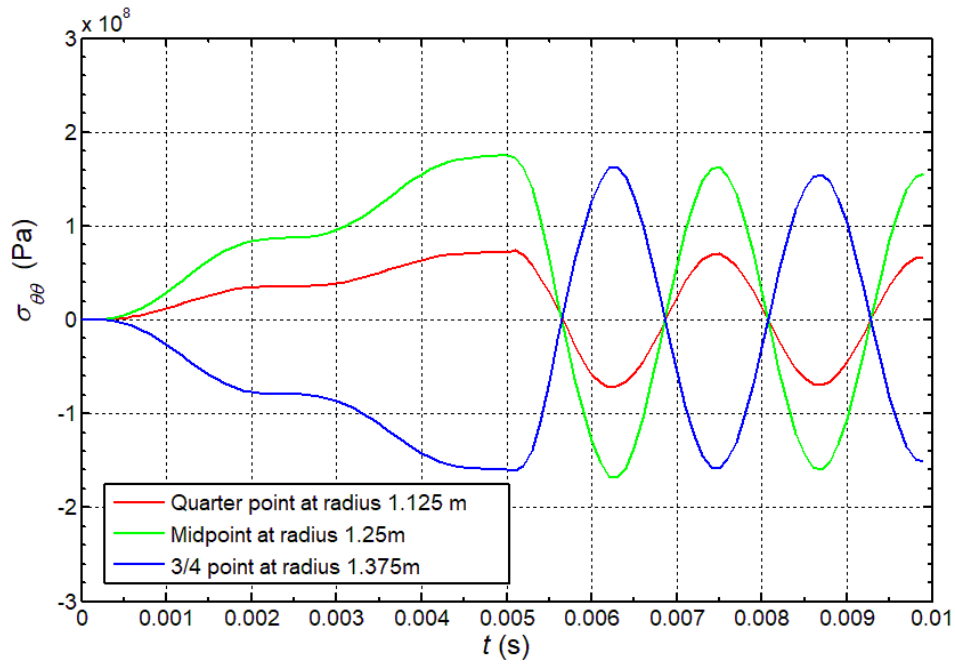


Figure 20: Comparison of hoop stress at various points of wall thickness

5.2 Composite thick-walled cylinder in plane strain condition –First case study

Similarly, the domain of the thick-walled cylinder is divided into M elements equal to 20 elements; that is 41 nodes. To validate the numerical solution obtained in plane strain condition by using the D-BEM, the solution of the homogeneous part (Material I) including the inner boundary term, $r \leq r_i$, is found by equating the material property indices: $n_1 = n_2$ and $E(r) = E_i$ & $\rho(r) = \rho_i$. Whereas, for the FGM part (Material II) including the outer boundary term, $r > r_i$, the solution can be obtained by putting $n_1 = 9.27$ and $n_2 = 1.87$ in the integral equation.

For plane strain, the Composite thick-walled cylinder geometry and, mechanical properties are proposed, as shown in table (3).

Material I	Aluminium	
Radius (m)	$r_i = 1.0$	
Elastic Modulus, $\bar{E}(GPa)$	76.92	
Density, $\rho (\frac{kg}{m^3})$	2700	
Material II	Aluminum	Ceramic Alumina
Radius (m)	$r_1 = 1.25$	$r_o = 1.5$
Elastic Modulus, $\bar{E}(GPa)$	76.92	417
Density, $\rho (\frac{kg}{m^3})$	2700	3800
Poisson Ratio, $\bar{\nu}$	0.428	0.428

Table 3: Composite thick-walled cylinder geometry and mechanical properties -plane strain.

For the plane strain, we can get the elasticity modulus $\bar{E}(r)$ and Poisson's ratio $\bar{\nu}$, as follows:

$$\bar{E}(r) = \frac{E(r)}{1-\nu^2}, \quad \bar{\nu} = \frac{\nu}{1-\nu} \quad (125)$$

So that for the inner radius, $r_i = 1m$:

$$\bar{E}_i = \frac{E_i}{1-\nu^2} = \frac{70}{1-0.3^2} = 76.92 \text{ GPa}$$

$$\bar{\nu} = \frac{\nu}{1-\nu} = \frac{0.3}{1-0.3} = 0.428$$

And using the material index, $n_1 = 9.27$, we get the elasticity for the outer surface as follows:

$$\bar{E}_o = \frac{\bar{E}_i}{(r_i/r_o)^{n_1}} = \frac{76.92}{(1.25/1.5)^{9.27}} = 417 \text{ GPa}$$

The studied composite thick-walled cylinder is subjected to an internal ramp pressure shock as expressed in eqn. (108).

5.2.1 Radial displacement response results for plane strain

As in the plane stress condition, different important points have been selected to show the radial displacement responses of the composite thick-walled cylinder. The ramp pressure shock is applied for a time period of 0.01 second at the following points:

1. Quarter depth point, at radius equals to 1.125 m.
2. At radius equals to 1.2 m.
3. Midpoint depth point, at radius equals to 1.25 m.
4. At radius equals to 1.3 m.
5. Three quarter depth point, at radius equals to 1.375 m.

For plane strain, the obtained radial displacement response for each of the selected points has been plotted, as shown in fig. (21).

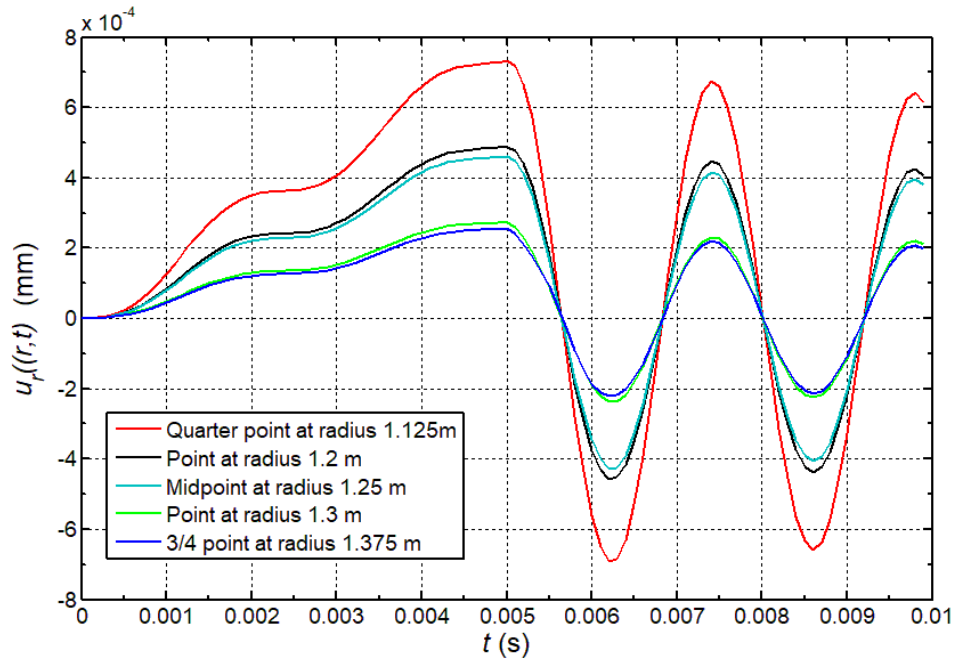


Figure 21: Comparison of various time history of radial displacement at different radii with $n_1 = 9.27$ & $n_2 = 1.87$.

5.2.2 Radial and circumferential stresses calculations for plane strain

Similarly, the radial and hoop stresses are calculated from the same equations (26 & 29) obtained in plane stress condition with the use of the appropriate values of Poisson's ratio and elasticity modulus listed in table (4).

The derivatives of the radial displacement (radial strain) are found by using the finite difference, as shown in eqn. (102).

5.2.2.1 Radial stress results for plane strain

Three different points along the thickness of the wall are selected to make the comparison (quarter point, midpoint and three-quarter point of wall's thickness). For the same ramp pressure shock, the radial stress responses are plotted along the time interval of 0.01 second, as shown in fig. (22).

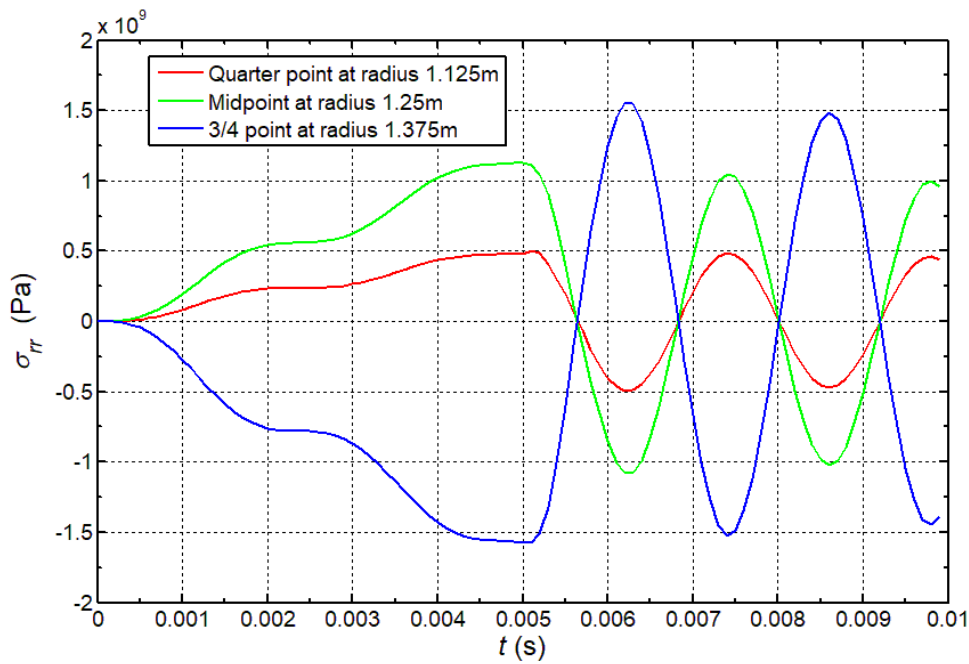


Figure 22: Comparison of Radial Stress at Various Points of Wall Thickness

5.2.2.2 Hoop stress results for plane strain

In the same way, the responses of the circumferential stress at the same selected points along the thickness of the wall are calculated and plotted for comparison, as shown in fig. (23).

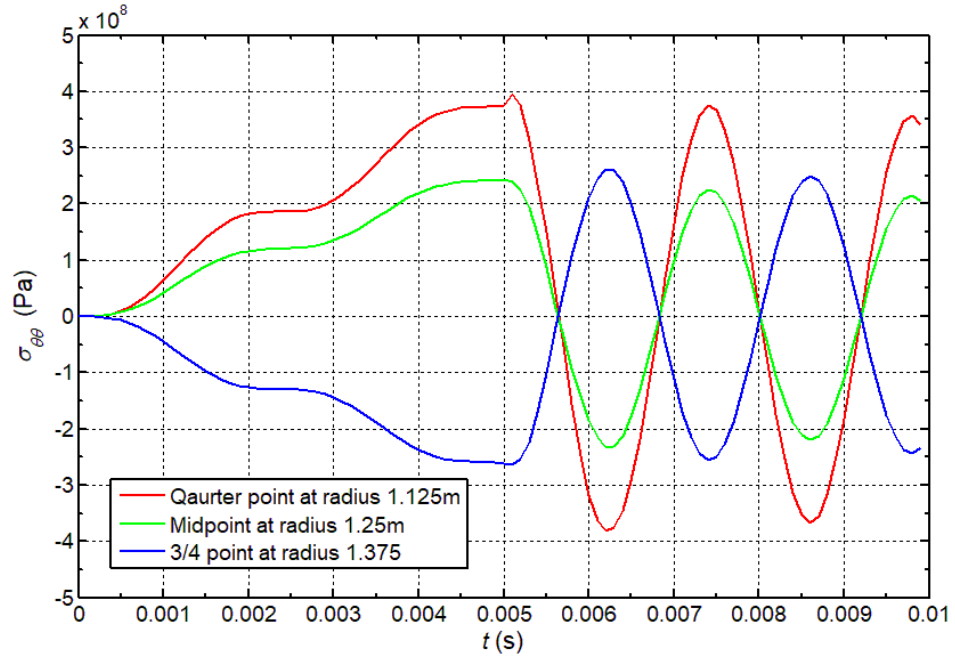


Figure 23: Comparison of Hoop Stress at Various Points of Wall Thickness.

5.3 FGM thick-walled cylinder in plane strain condition – Second case study

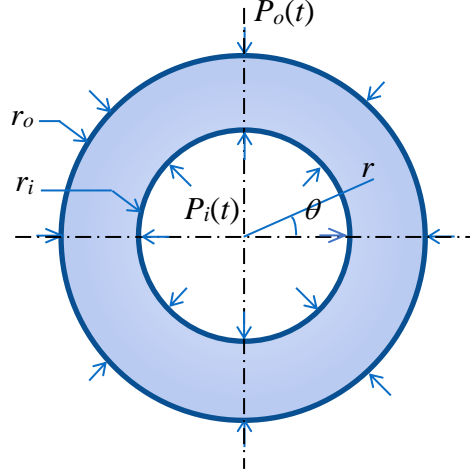


Figure 24: FGM thick-walled hollow cylinder under pressure shock loads

The FGM thick-walled cylinder under the effect of pressure shock type of loading is considered in this case study is illustrated in fig. (24). Two different loading conditions are taken to study the effect of ramp pressure shock.

5.3.1 The pressure loading on the inner surface of the cylinder

On the inner surface, uniformly distributed variable shock pressure $P_i(t)$ of ramp type that is given by eqn. (108). But, there is no external pressure applied, i.e., $P_o(t) = 0$. In all the computations, the thick-walled cylinder is assumed to be in the plane strain state. The elastic modulus and the material density are varying according to the relations given by eqn. (126).

$$E(r) = E_o \left(\frac{r}{r_o} \right)^{n_1}, \quad \rho(r) = \rho_o \left(\frac{r}{r_o} \right)^{n_2}, \quad (126)$$

In addition, inner and outer radii of the cylinder are $r_i = 1$ m and $r_o = 1.2$ m, respectively. The outer surface at $r = r_o$ is considered Ceramic alumina with

$E_o = 380 \text{ GPa}$ and $\rho_o = 3800 \text{ kg/m}^3$. However, Poisson's ratio is considered constant, $\nu = 0.3$. The normalized parameters used for the illustration are defined as:

$$\sigma_0 = p^* t_0, \quad u_0 = \frac{\sigma_0}{E_o} r_o. \quad (127)$$

The time response of the normalized radial displacement and normalized stress components, u_r/u_0 , σ_{rr}/σ_0 , and $\sigma_{\theta\theta}/\sigma_0$, at the midpoint, $r = (r_i + r_o)/2$, are plotted in figures (25, 26 and 27), respectively. The domain is divided into 20 quadratic elements and, the time step used in the execution of the Houbolt's method is $1 \times 10^{-5} \text{ s}$. The radial displacement, u_r , behavior follows the ramp type shock loading until the time, $t = t_0$. At the cut-off time, the cylinder is unloaded, and the location studied at the midpoint begins to experience oscillatory motion. As the material indices n_1 and n_2 are decreased from 0.5 to -1.0 , the displacement amplitude is getting smaller. This means that when $n_i > 0$, the material properties increase in r -direction, whereas when $n_i < 0$, they are decreasing function of r . Moreover, the vibration amplitudes and magnitudes of radial and circumferential stresses also become lesser as the material indices n_1 and n_2 are decreased from 0.5 to -1.0 .

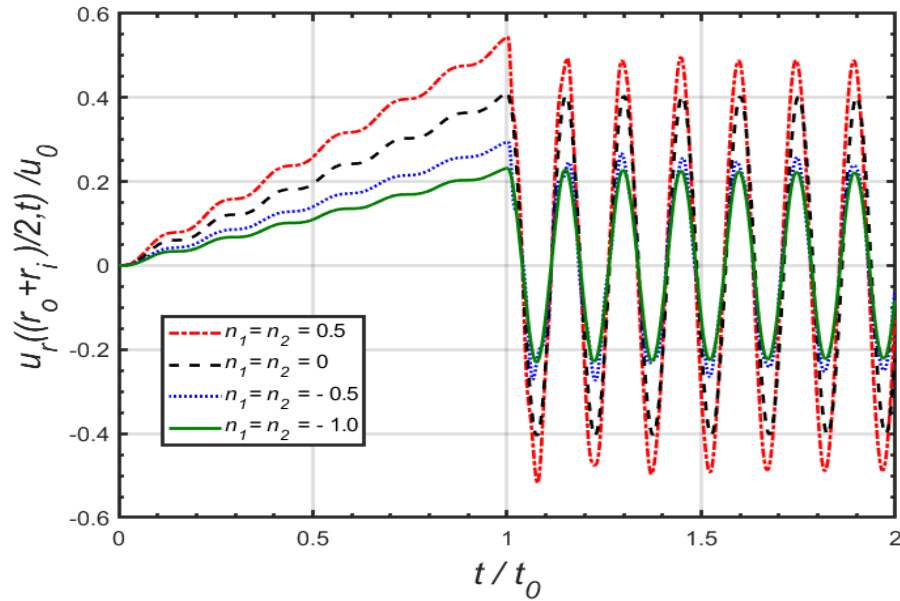


Figure 25: Dimensionless radial displacement at the mid-point, $r = (r_i + r_o)/2$, of an FGM cylinder under internal pressure shock.

Therefore, it can be concluded that, as long as the material property values at the outer surface, $r = r_o$, are constant, midpoint stress components magnitudes calculated by considering the decrease of material properties are less than those determined with the increase physical properties.

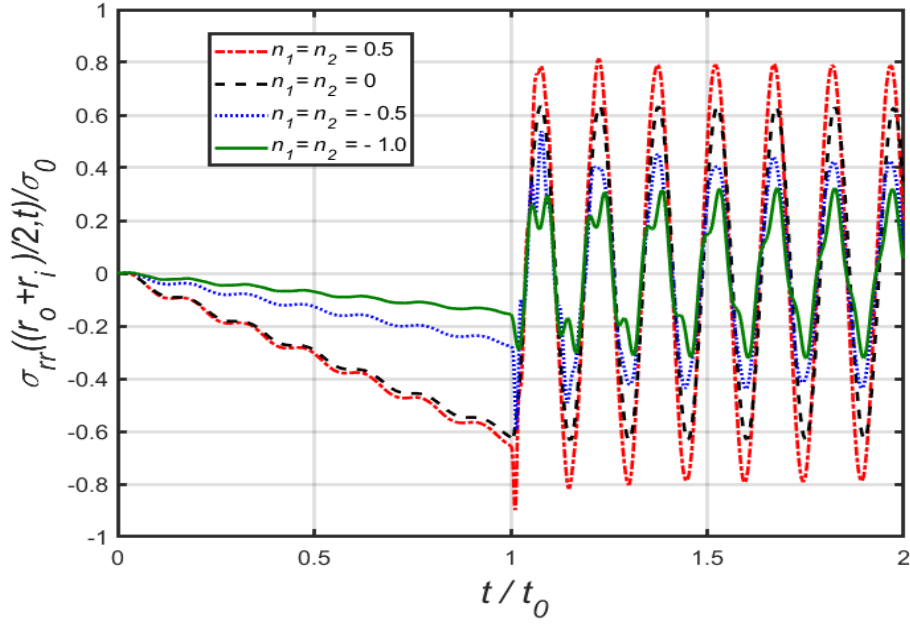


Figure 26: Dimensionless radial stress at the mid-point, $r = (r_i + r_o)/2$, of an FGM cylinder under internal pressure shock.

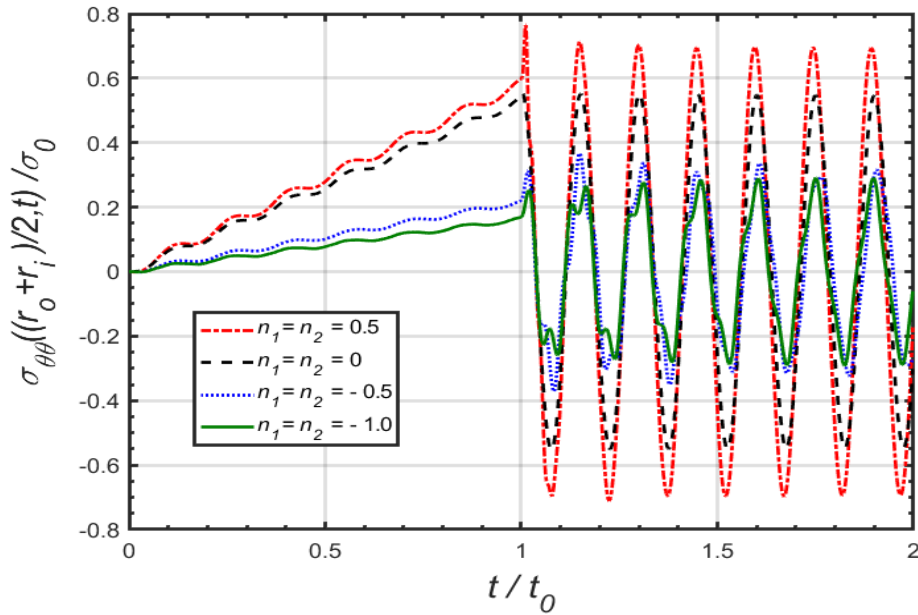


Figure 27: Dimensionless tangential stress at the mid-point, $r = (r_i + r_o)/2$, of an FGM cylinder under internal pressure shock.

For further investigation, a point closer to the inner surface of the FGM thick-walled cylinder is considered. This point is taken as $r_c = r_i + (r_o - r_i)/10$. The time histories of dimensionless radial displacements, dimensionless radial stress and tangential stresses at various material property indices are plotted for comparison, as shown in figures (28, 29 and 30). Displacement amplitude and vibration amplitudes of stresses get smaller as n_1 and n_2 are decreased from 0.5 to -1.0 . But, as observed the vibrations have a time lag behaviour. The amplitudes of radial displacement as well as the radial stress are larger than those obtained at the midpoint of thickness.

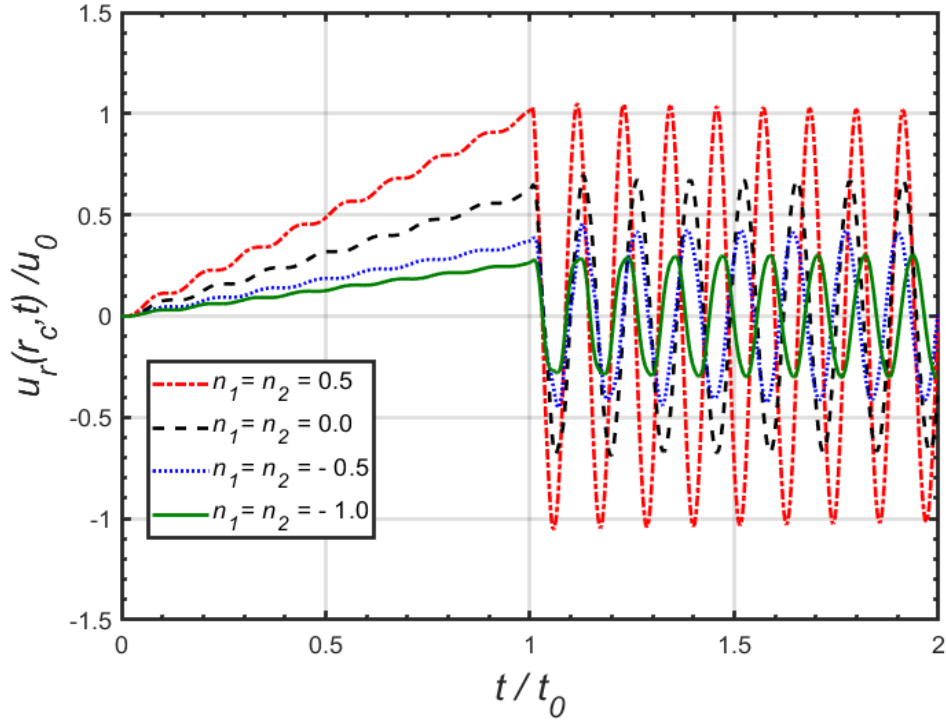


Figure 28: Dimensionless radial displacement at point, $r_c = r_i + (r_o - r_i)/10$, of an FGM cylinder under internal pressure shock.

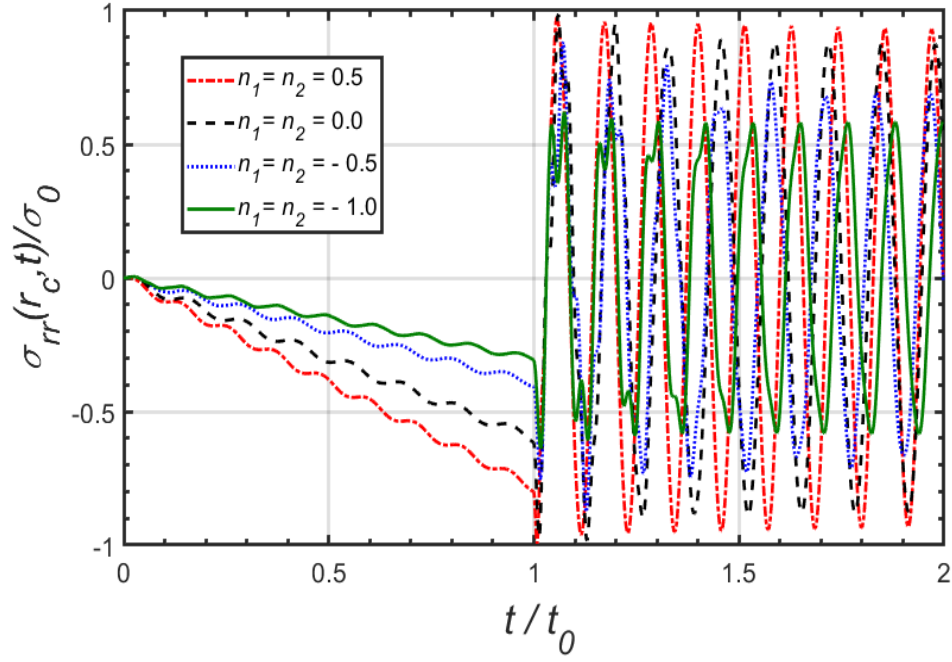


Figure 29: Dimensionless radial stress at point, $r_c = r_i + (r_o - r_i)/10$, of an FGM cylinder under internal pressure shock.

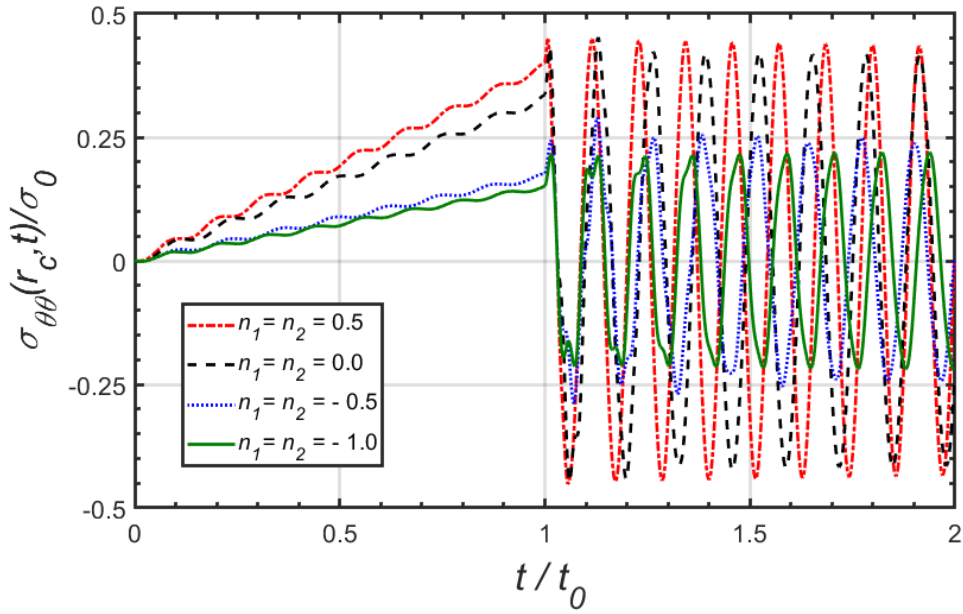


Figure 30: Dimensionless tangential stress at point, $r_c = r_i + (r_o - r_i)/10$, of an FGM cylinder under internal pressure shock.

Another important factor which has a significant effect on the elastodynamic response of FGM cylinders is the radius ratio of the cylinder, r_o/r_i . Different outer radii of the cylinder are used to study this factor. Material property exponents n_1 and n_2 are taken as -1 , and the inner radius of the cylinder, r_i , is taken as 0.1 m. However, the responses of the non-dimensional radial displacement, radial and tangential stresses at the midpoint of wall thickness are plotted at various radius ratio, as shown in figures (31, 32 and 33). It is obvious that the amplitudes of radial displacement and stresses are decreased with the increase ratio r_o/r_i . Moreover, the behavior of stress vibrations at the midpoint has a different pattern and this could be due to the high stiffness of the material.

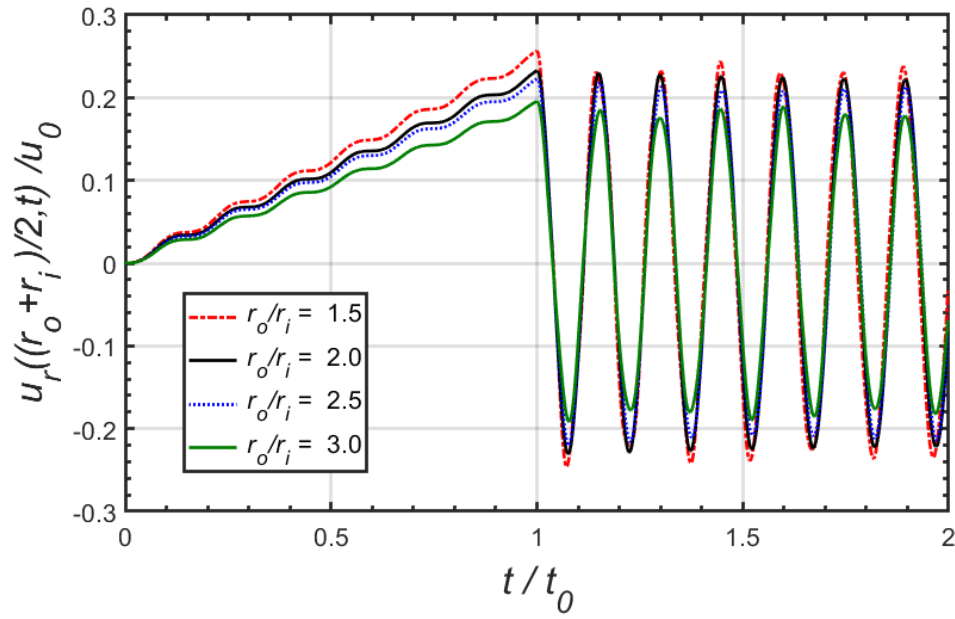


Figure 31: Dimensionless radial displacement response at different r_o/r_i for an FGM cylinder under internal pressure shock at $n_1 = n_2 = -1$.

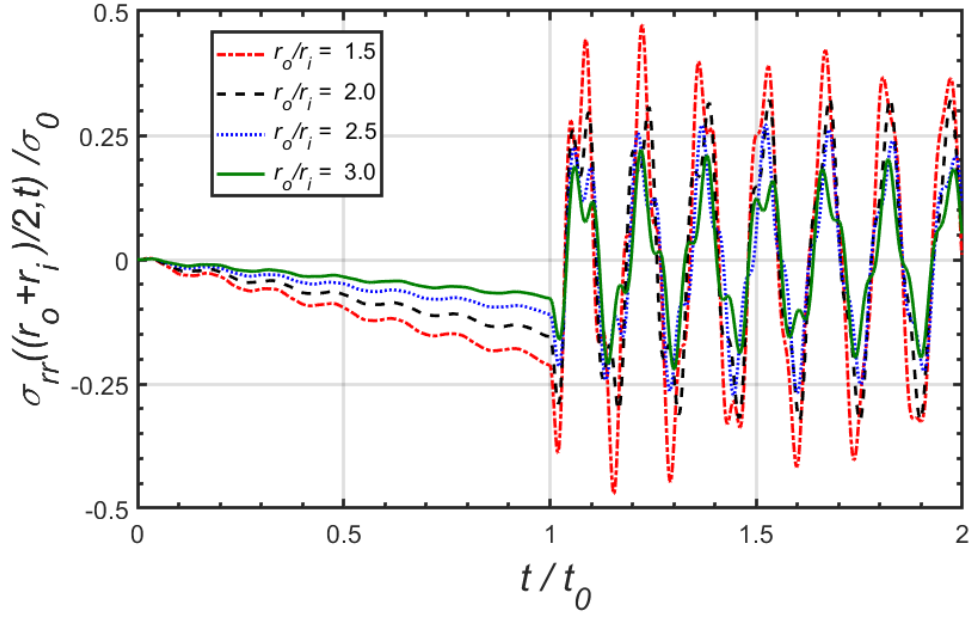


Figure 32: Dimensionless radial stress response at different r_o/r_i for an FGM cylinder under internal pressure shock at $n_1 = n_2 = -1$.

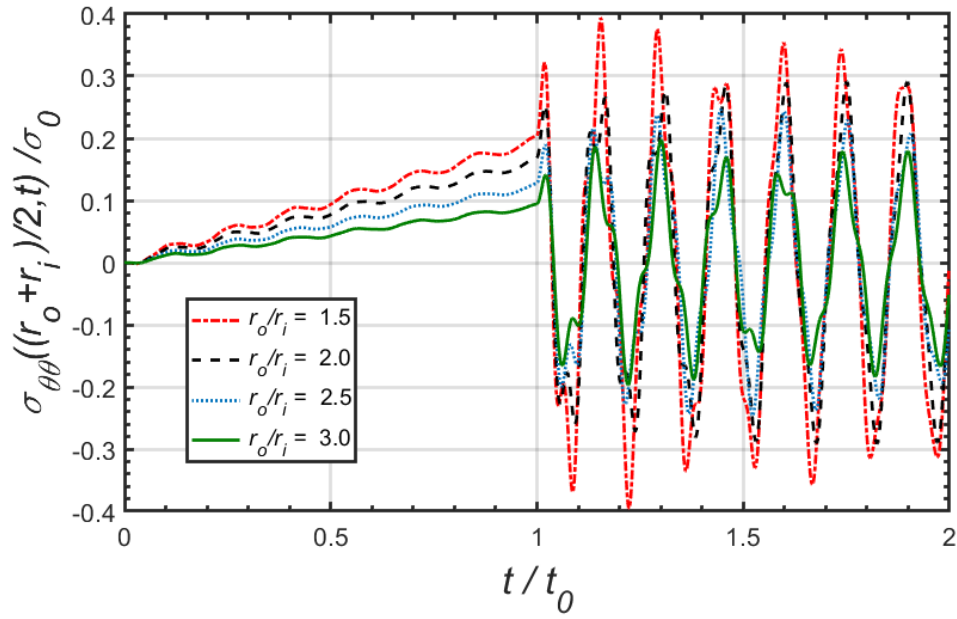


Figure 33: Dimensionless tangential stress response at different r_o/r_i for an FGM cylinder under internal pressure shock at $n_1 = n_2 = -1$.

Furthermore, another set of results are obtained for the same ratios of the outer radii of the cylinder, but with different material property exponents n_1 and n_2 , which are taken as 0.5, and the inner radius of the cylinder, r_i , is taken as 0.1 m. This means the material at midpoint is less stiff with increasing the outer radius. The vibration response of the radial displacement, radial stress and tangential stresses are plotted for the various radii ratios, r_o/r_i , as shown in figures (34, 35 and 36). Obviously, the amplitudes of the vibration waves increase with the decrease of the radii ratio r_o/r_i . As the material becomes less stiff at the midpoint of thickness, the behavior of vibration is becoming more harmonic and single peaks are present as compared to the last case when the material is more stiff with $n_1 = n_2 = -1$.

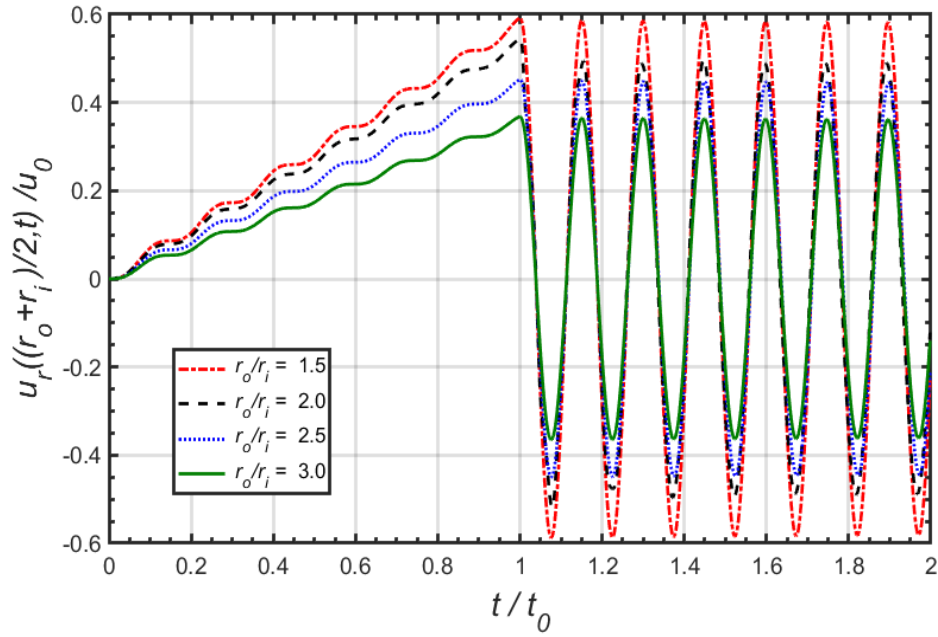


Figure 34: Dimensionless radial displacement response at different r_o/r_i for an FGM cylinder under internal pressure shock at $n_1 = n_2 = 0.5$.

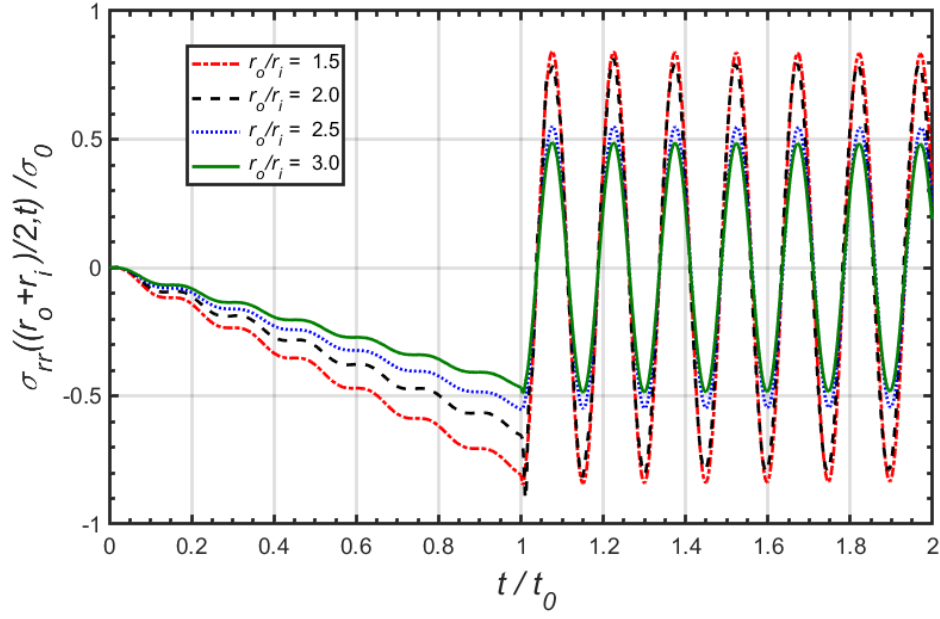


Figure 35: Dimensionless radial stress response at different r_o/r_i for an FGM cylinder under internal pressure shock at $n_1 = n_2 = 0.5$.

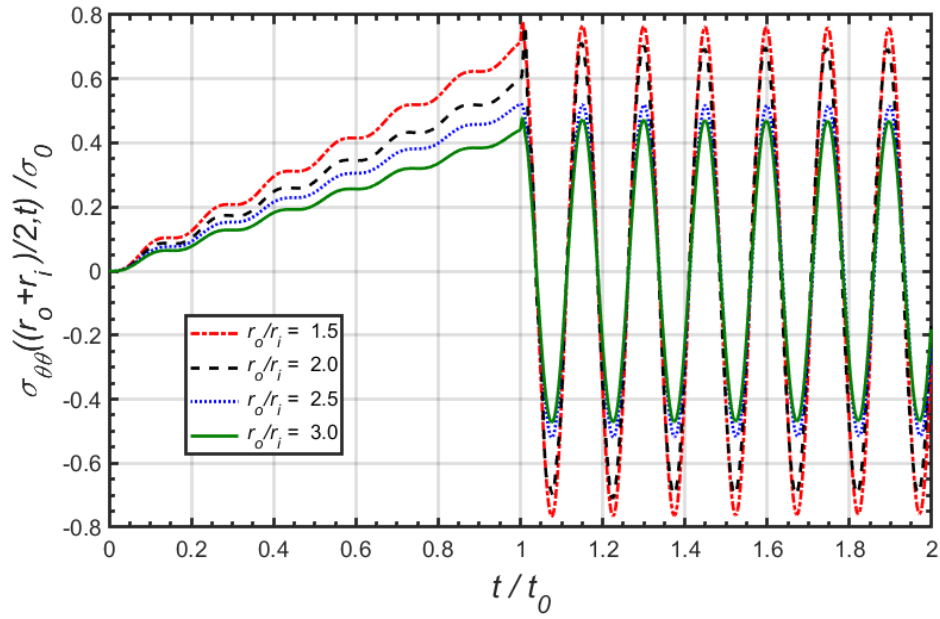


Figure 36: : Dimensionless tangential stress response at different r_o/r_i for an FGM cylinder under internal pressure shock at $n_1 = n_2 = 0.5$.

The spatial radial displacement, radial stress and tangential stress as functions of r/r_i for $t=t_0$ are shown in figures (37, 38 and 39), respectively. However, the radial displacement is positive for all the material indices n_1 and n_2 values used in the calculations, and decrease in the r -direction. The normalized radial stress component, σ_{rr}/σ_0 is compressive at $t=t_0$, and its normalized value changes from -1 at the inner surface, $r=r_i$, to 0 at the outer free surface, $r=r_o$, which is in agreement with the stress boundary conditions. On the other side, circumferential stress is in tension and the overall trend rely on the material property exponents n_1 and n_2 , which means when the material indices are zero or positive, the normalized tangential stress, $\sigma_{\theta\theta}/\sigma_0$ is increasing r -direction. However, in case of the negative exponents, the normalized tangential stress is decreasing in the radial direction.

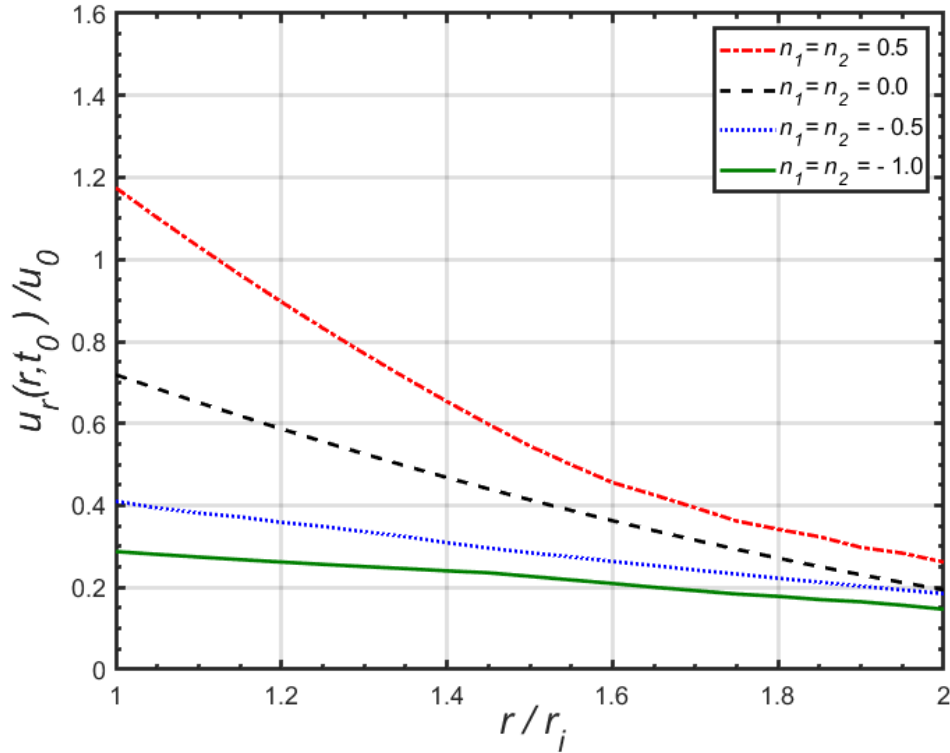


Figure 37: Dimensionless spatial radial displacement computed at $t=t_0=0.005$ s considering an FGM cylinder under internal pressure shock.

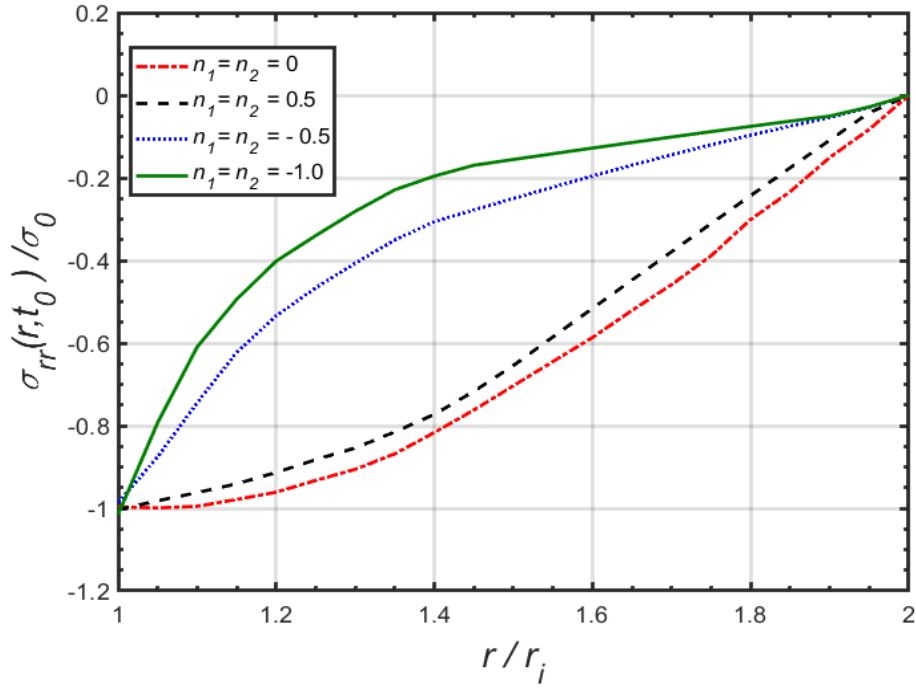


Figure 38: Dimensionless spatial radial stress computed at $t = t_0 = 0.005$ s considering an FGM cylinder under internal pressure shock.

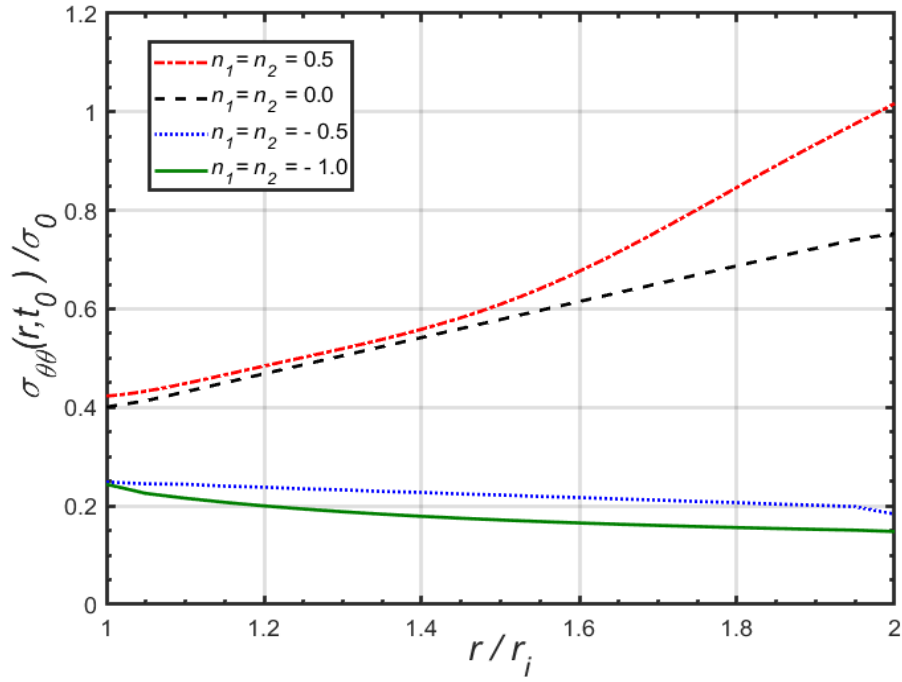


Figure 39: Dimensionless spatial tangential stress computed at $t = t_0 = 0.005$ s considering an FGM cylinder under internal pressure shock.

5.3.1.1 Parametric analysis of stress concentration related to circumferential stress

To make this parametric analysis, the maximum absolute tangential stress is divided by the stress at the cut off time, t_0 , which is $|\sigma_{\theta\theta}|_{\max}/\sigma_0$. Hence, three different temporal points are selected $0.5t_0, t_0$ & $1.08t_0$ and four material exponents $n_1 = n_2 = n = 0.5, 0.0, -0.5$ & -1.0 . Therefore, the magnitude of the maximum circumferential stress and the location, normalized radial coordinates, of the stress concentration points are tabulated in tables (4 and 5), respectively.

N	t/t_0		
	0.5	1.00	1.08
0.5	0.476	1.015	1.002
0.0	0.355	0.753	0.697
-0.5	0.108	0.248	0.379
-1.0	0.113	0.244	0.250

Table 4: $|\sigma_{\theta\theta}|_{\max}/\sigma_0$ values for an FGM thick-walled cylinder under internal pressure shock, $r_i = 0.1$ m, $r_o = 0.2$ m, $n_1 = n_2 = n$.

n	t/t_0		
	0.5	1.00	1.08
0.5	2.00	2.00	2.00
0.0	2.00	2.00	1.55
-0.5	2.00	1.00	1.55
-1.0	1.00	1.00	1.00

Table 5: r/r_i values corresponding to largest circumferential stress amplitudes for an FGM thick-walled cylinder under internal pressure shock, $r_i = 0.1$ m, $r_o = 0.2$ m, $n_1 = n_2 = n$.

From the tables above, the stress concentration is more when the material property exponent equals to 0.5, and it occurs at the outer surface. Whereas, when the material exponents are negative the stress concentration, $|\sigma_{\theta\theta}|_{\max}/\sigma_0$, is less as compared to the results obtained for positive material exponents. Moreover, the maximum stress concentration mostly happens at either the inner edge or the outer edge of the thick-walled cylinder depending on the material property exponent used.

5.3.2 The pressure loading on the outer surface of the cylinder

The thick-walled FGM cylinder under effect of the external pressure $P_o(t)$ is studied. The cylinder geometry and the pressure loading are shown in Fig. (1). However, the internal pressure is considered to be zero; whereas the outer edge pressure shock is defined as the short-time ramp loading:

$$P_o(t) = \begin{cases} p^* t, & 0 < t \leq t_0, \\ 0, & t > t_0, \end{cases} \quad (128)$$

Where; p^* and t_0 are 4 GPa/s and 0.005 s, respectively.

The outer surface of the thick-walled cylinder is considered 100% alumina. However, the material properties formulas and the dimensions of the cylinder are precisely the same as the one used in the calculation of the inner loading condition studied in the last section. In addition, the normalized parameters are given by Eq. (127).

The numerical results obtained are plotted in figures (40, 41 and 42), which show the response of the radial displacement and stress components (radial and circumferential) at the midpoint of wall thickness, $r = (r_i + r_o)/2$, for different values of the material property exponents $n_1 = n_2 = \{0.5, 0, -0.5, -1.0\}$.

However, the radial displacement at the midpoint of the cylinder's wall thickness initially varies in the negative r -direction because of the application of pressure shock on the outer surface. The resulted vibration motion got the highest amplitudes of vibration for the radial displacement and the stress components when calculated at material property exponents $n_1 = n_2 = 0.5$. But, the amplitudes are getting smaller when the exponents n_1 and n_2 are reduced from 0.5 to -1.0 . Thus, the general trend of the vibrations resulted in the case of applying external pressure shock is similar to that obtained for the same internal ramp shock loading. This means that decreasing physical properties will lower the magnitudes of vibrations.

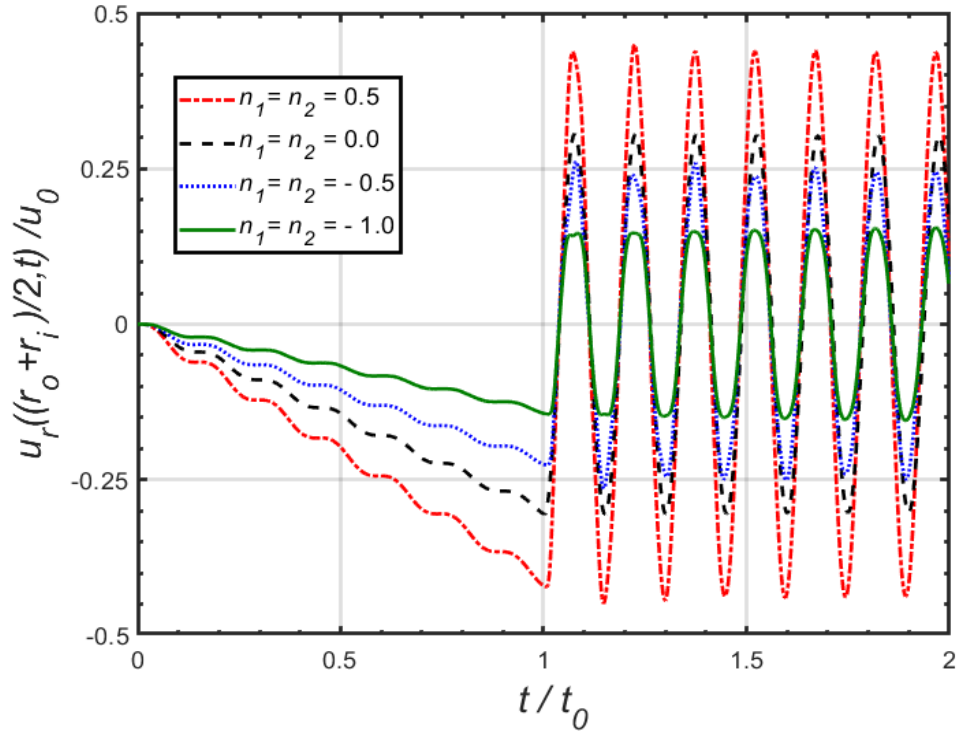


Figure 40: Dimensionless radial displacement at the mid-point, $r = (r_i + r_o)/2$, of a FGM cylinder under external pressure shock.

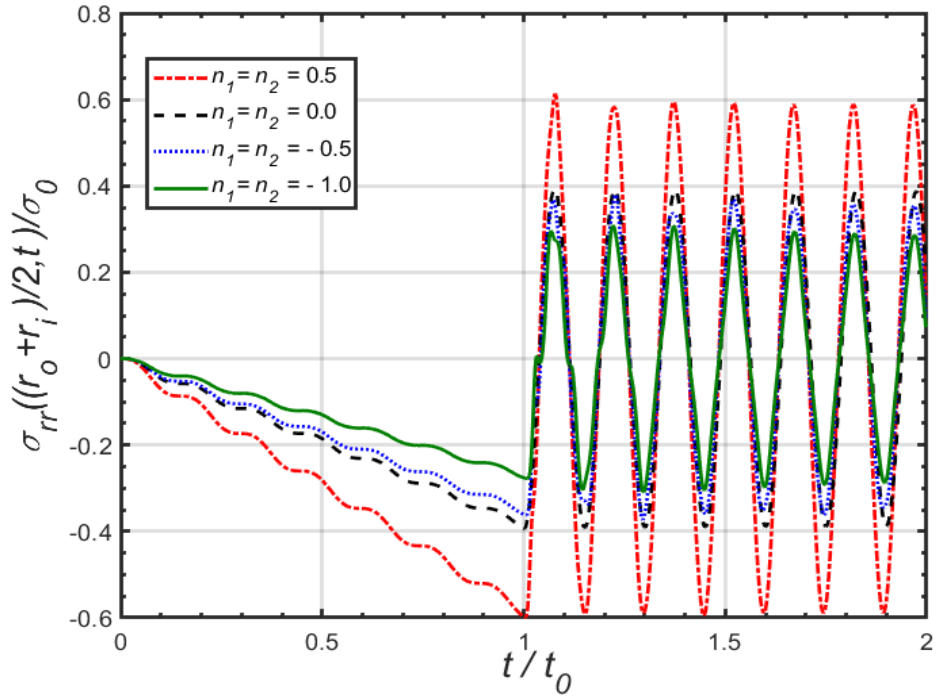


Figure 41: Dimensionless radial stress at the mid-point, $r = (r_i + r_o)/2$, of a FGM cylinder under external pressure shock.

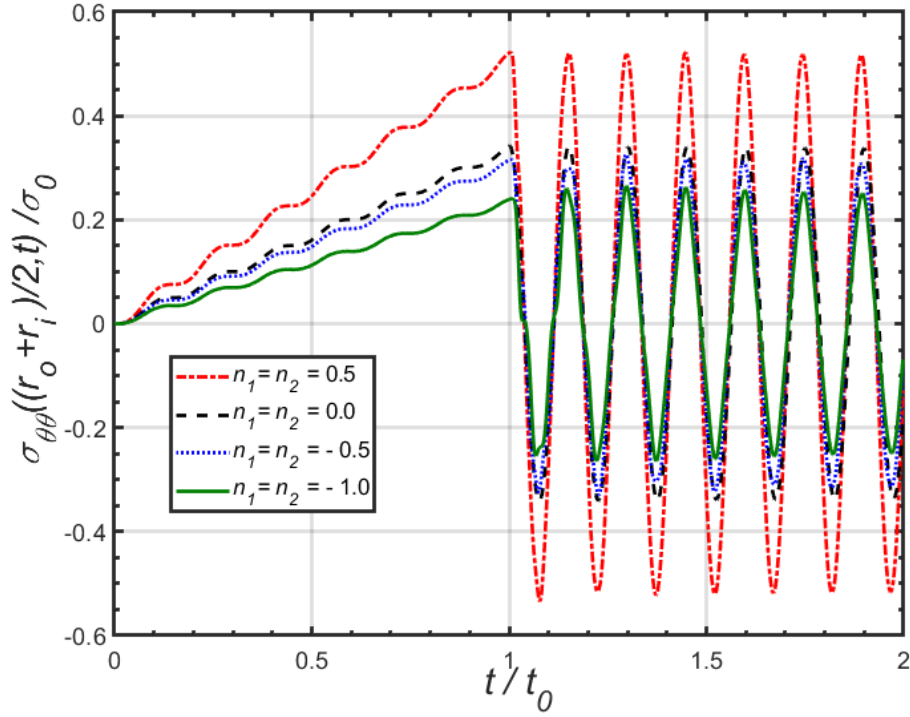


Figure 42: Dimensionless tangential stress at the mid-point, $r = (r_i + r_o)/2$, of a FGM cylinder under external pressure shock.

However, spatial distributions computed at $t = t_0$ for radial displacement, radial stress and tangential stress are shown in figures (43, 44 and 45), respectively. At the selected cut-off time, the radial spatial displacements are decreasing in the radial direction r . Though, the radial stress component is compressive and satisfies the stress boundary conditions at both edges, and the circumferential stress component is found to be positive for all the suggested values of material property exponents, n_1 and n_2 .

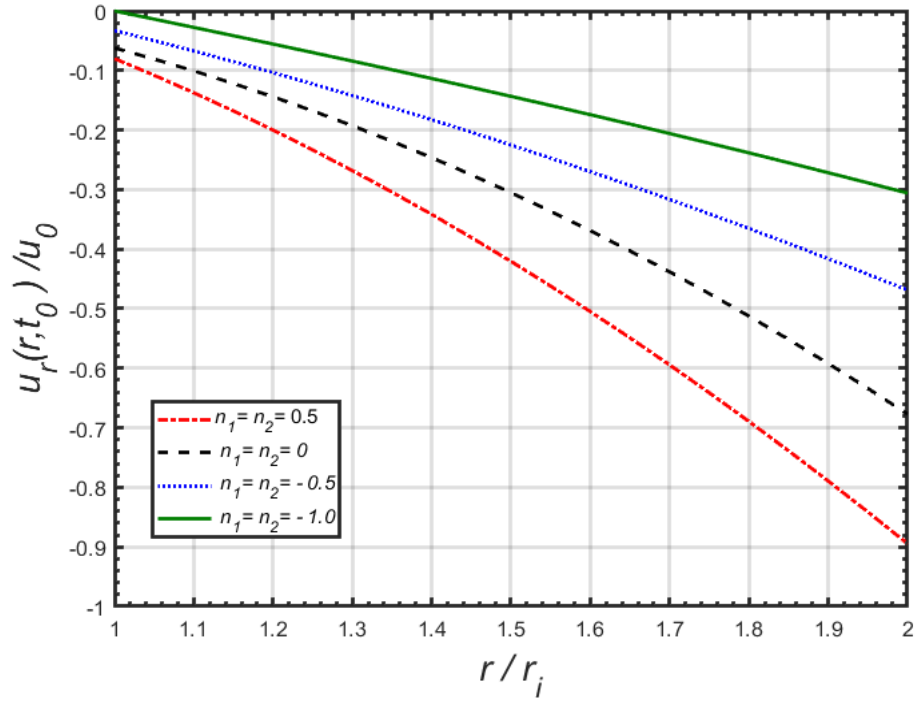


Figure 43: Dimensionless spatial radial displacement computed at $t = t_0 = 0.005$ s considering an FGM cylinder under external pressure shock.

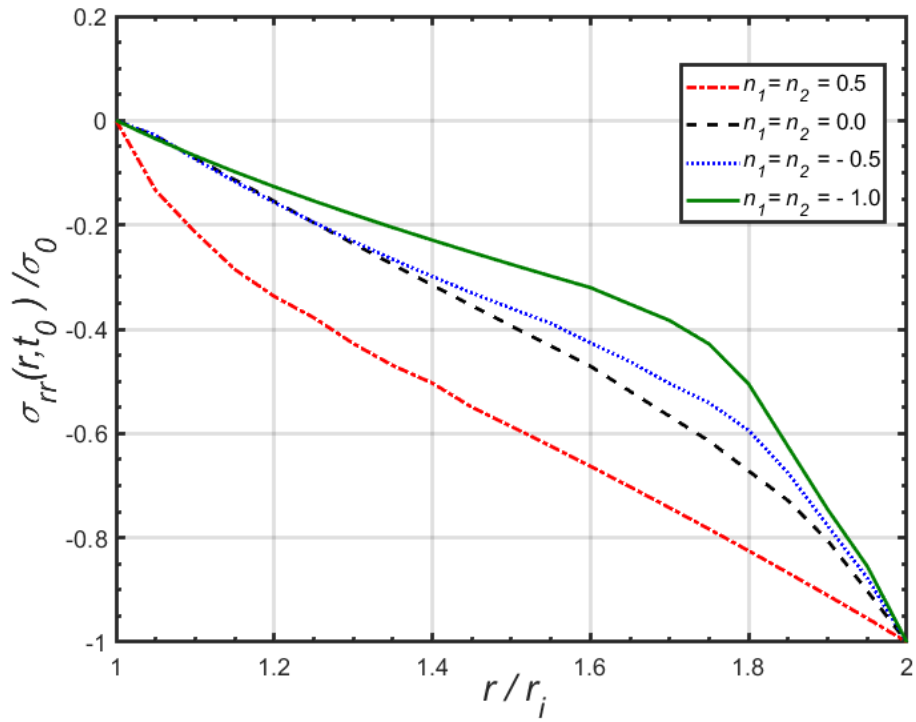


Figure 44: Dimensionless spatial radial stress computed at $t = t_0 = 0.005$ s considering an FGM cylinder under external pressure shock.

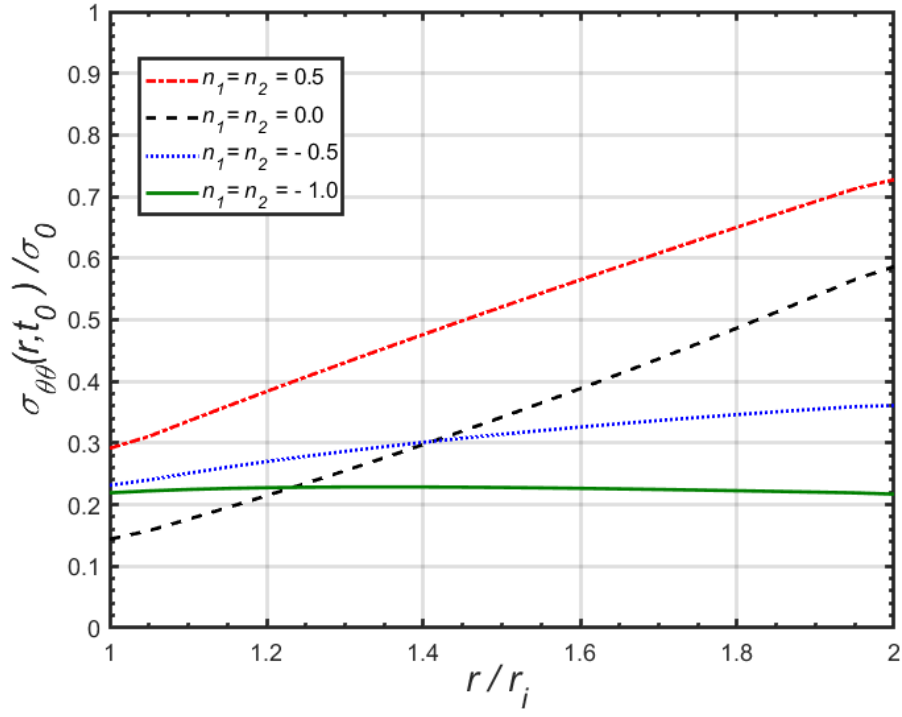


Figure 45: Dimensionless spatial tangential stress computed at $t = t_0 = 0.005$ s considering an FGM cylinder under external pressure shock.

5.4 Annular external FGM coating thick-walled cylinder in plane strain condition

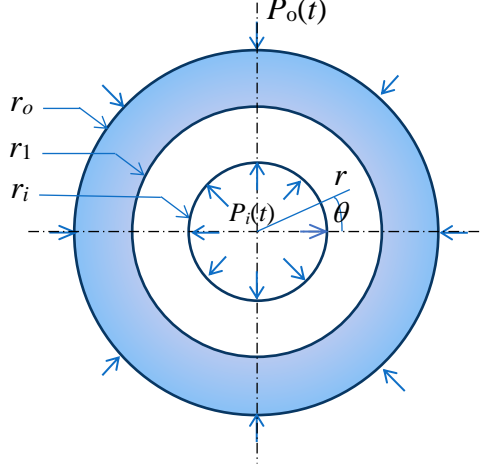


Figure 46: Composite thick-walled cylinder under exponential internal pressure.

The other problem we consider in numerical analyses is that of an annular FGM coating ($r_i < r < r_o$) bonded to a homogeneous substrate ($r_i < r < r_1$) on the external surface, as shown in Figure (46). The homogeneous substrate is assumed to be subjected to an internal exponential variation type pressure shock, exponential loading, whose mathematical representation is as follows:

$$P_i(t) = P_a (1 - \exp(-\gamma t)), \quad t > 0, \quad (129)$$

Where, P_a is the inner pressure for a large period of time t , and γ is a temporal constant with the unit $1/s$.

The pressure on the outer surface of the cylinder, $P_o(t)$, is assumed to be zero and, material properties of the FGM external coating and the homogeneous internal substrate are varying according to a power law of volume fraction and defined by:

$$E(r) = \begin{cases} E_o \left(\frac{r_1}{r_o} \right)^{n_1}, & r_i < r < r_1, \\ E_o \left(\frac{r}{r_o} \right)^{n_1}, & r_1 < r < r_o, \end{cases} \quad \rho(r) = \begin{cases} \rho_o \left(\frac{r_1}{r_o} \right)^{n_2}, & r_i < r < r_1, \\ \rho_o \left(\frac{r}{r_o} \right)^{n_2}, & r_1 < r < r_o. \end{cases} \quad (130)$$

Considering that the physical properties are continuous at the interface, $r = r_1$. The composite thick-walled cylinder is in the plane strain state; and Poisson's ratio is assumed constant and equals to 0.3. The radii are taken as: $r_i = 0.05$ m, $r_1 = 0.1$ m, and $r_o = 0.2$ m. Hence, with an appropriate definition of the material properties for the elements in the FGM annular coating and the homogeneous internal substrate of the cylinder, the formulation and solution procedure described in chapter three, the D-BEM formulation, can be applied to examine the elastodynamic behavior of the composite thick-walled cylinder. However, the homogeneous internal substrate is modelled by a total of 7 quadratic cells, whereas 15 quadratic cells are employed to model the external FGM coating, and the time step used for the Houbolt's method is 1×10^{-5} s. The composite cylinder is subjected to an exponential internal dynamic pressure. However, the normalized parameters are expressed as:

$$\sigma_0 = P_a, \quad u_0 = \frac{P_a}{E_o} r_o. \quad (131)$$

The time histories of the radial displacement, radial and circumferential stresses computed at the midpoint of wall's thickness, $r = (r_i + r_1)/2$, of the homogeneous substrate, are illustrated in figures (47, 48 and 49), respectively.

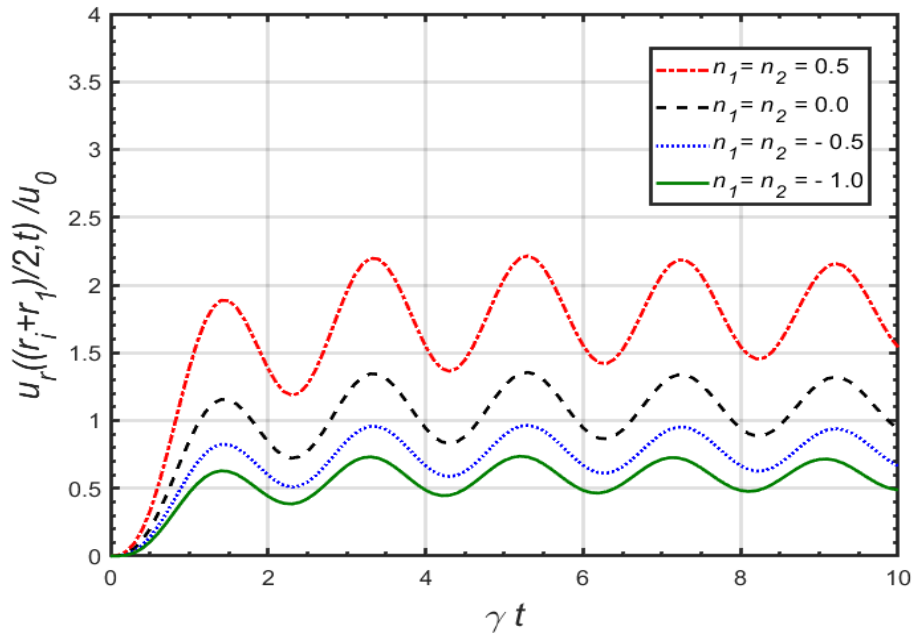


Figure 47: Dimensionless radial displacement at the mid-point, $r = (r_i + r_1)/2$, of the inner homogeneous substrate under internal exponential pressure

The material property exponents n_1 and n_2 are considered equal. The non-dimensional time γt is varied between 0 and 10. In each case, the trend of the oscillations is superimposed in an increasing or decreasing manner.

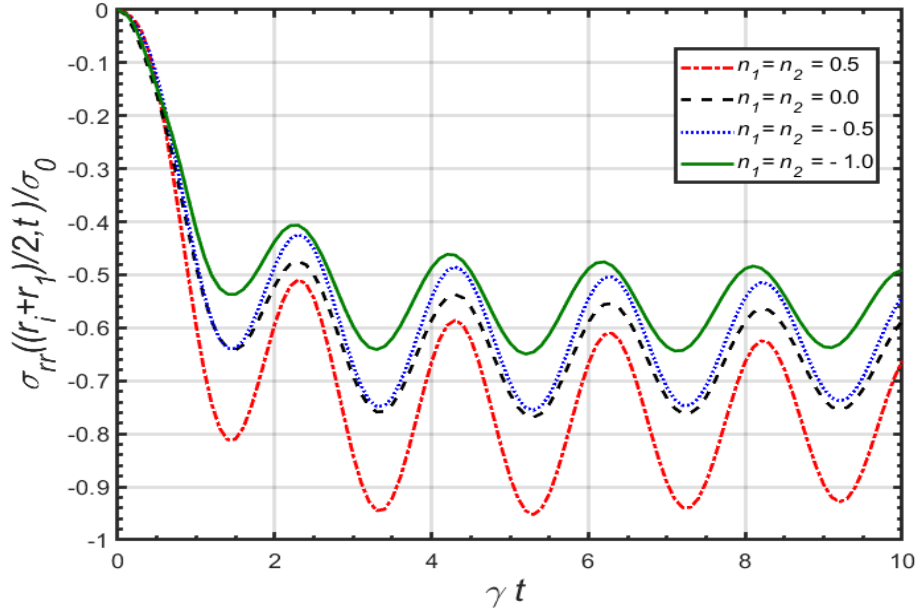


Figure 48: Dimensionless radial stress at the mid-point, $r = (r_i + r_1)/2$, of the inner homogeneous substrate under internal exponential pressure

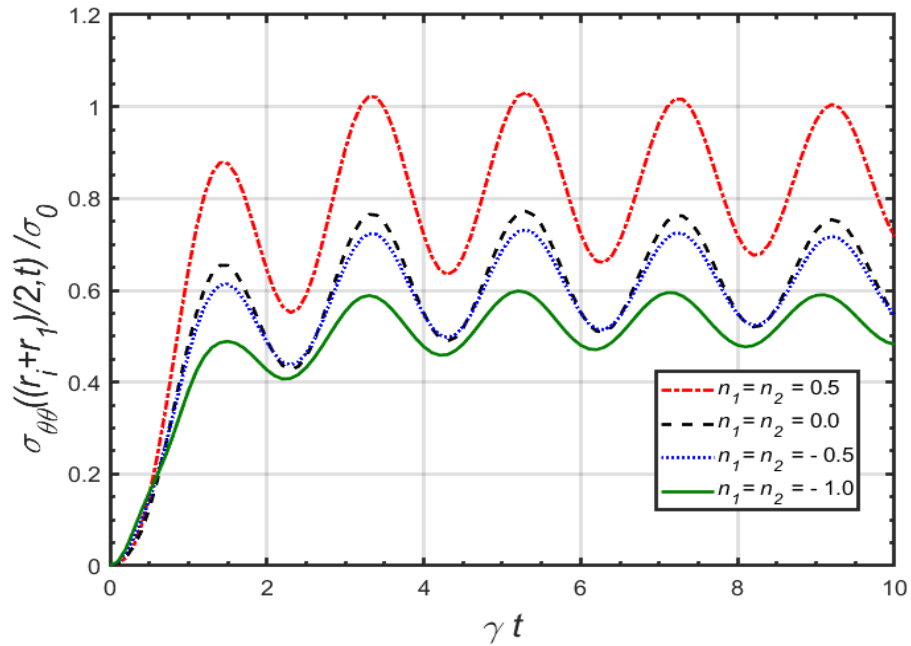


Figure 49: Dimensionless tangential stress at the mid-point, $r = (r_i + r_1)/2$, of the inner homogeneous substrate under internal exponential pressure

The magnitude of the amplitudes For both the radial displacement and stress components, the magnitude becomes smaller as the exponents are decreased from 0.5 to -1 . This shows that for a FGM external coating with physical properties decreasing in radial direction, the midpoint of thickness amplitudes computed are less than those computed for a FGM coating that has increasing material properties, assuming that properties at $r = r_o$ are constant.

Moreover, the numerical results that show the variations of the radial displacement and, the radial and hoop stresses at the midpoint of wall thickness, $r = (r_1 + r_o)/2$, of the functionally graded annular coating are shown in figures (50, 51 and 52).

However, the trend of time histories of the radial displacement, radial and tangential stresses are generally similar to the one computed for the midpoint of the homogeneous substrate of the cylinder. On the other side, as the material property exponents decreased from 0.5 to -1 , the magnitudes of these variables for the FGM annular coating are also decreased.

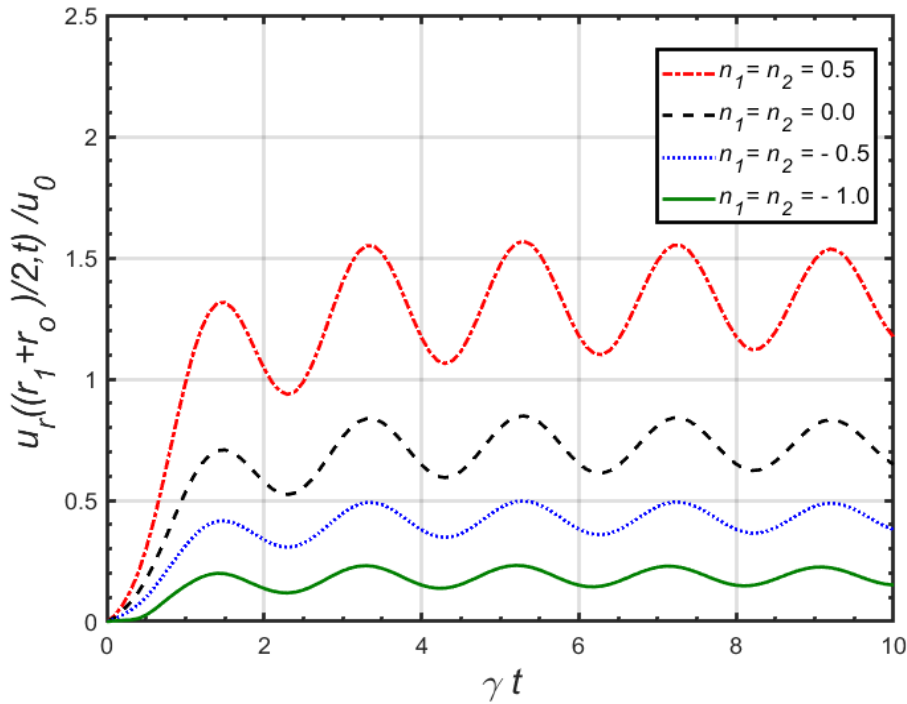


Figure 50: Dimensionless radial displacement at the mid-point, $r = (r_o + r_1)/2$, of the FGM outer coating under internal exponential pressure.

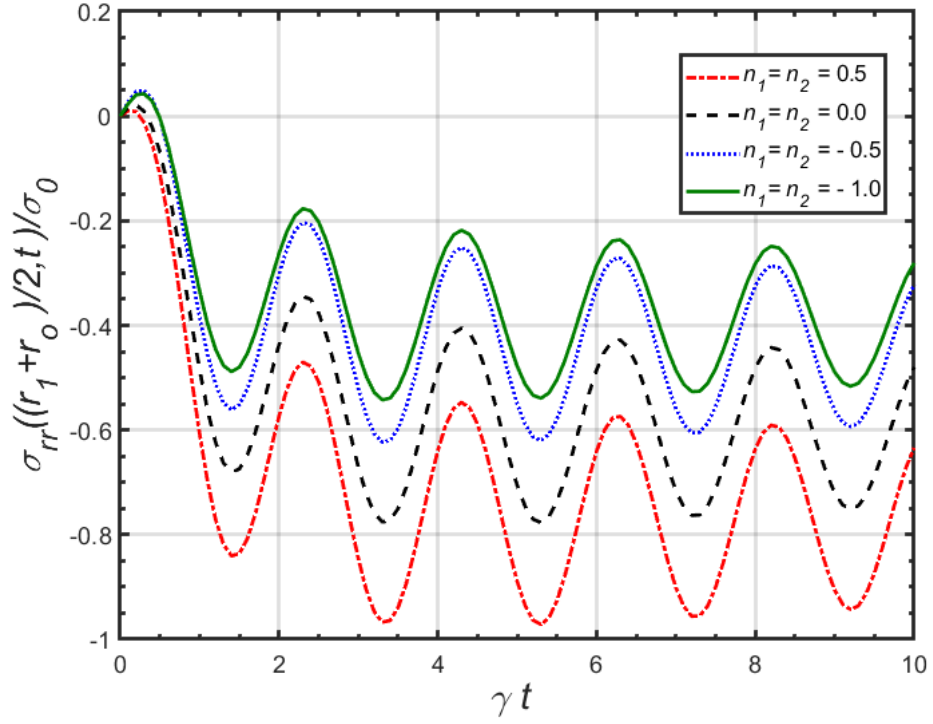


Figure 51: Dimensionless radial stress at the mid-point, $r = (r_o + r_i)/2$, of the FGM outer coating under internal exponential pressure.

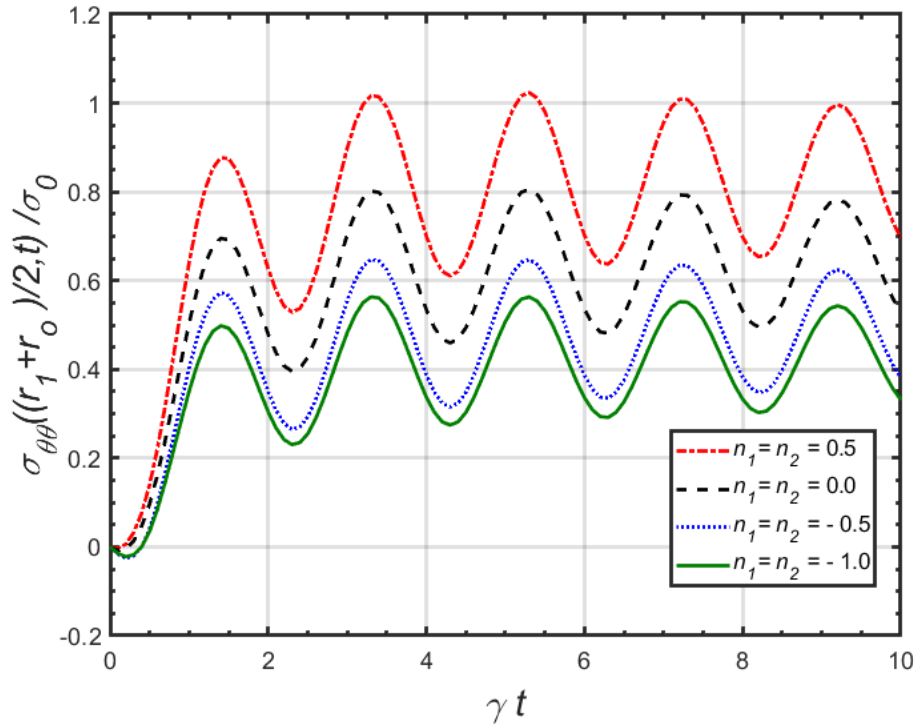


Figure 52: Dimensionless tangential displacement at the mid-point, $r = (r_o + r_i)/2$, of the FGM outer coating under internal exponential pressure.

Furthermore, at the dimensionless time γt equals 10, the variation of the spatial radial displacement and, spatial radial and tangential stress components are plotted in figures (53, 54 and 55), respectively. As r/r_1 is increased from 0.5 to 2.0, the radial displacements are positive and decreasing in the radial direction. Whereas, the radial stress satisfies the boundary conditions at both edges of the thick-walled cylinder, and it is increasing in the radial direction. Hence, the lowest radial stress magnitudes are computed at $n_1 = n_2 = -1$. On the other hand, the circumferential stress is always positive for all values of the material property indices used; and it passes through a minimum value when the exponents are either 0.5 or 0. But, the circumferential stress is a decreasing function in the radial direction, when the material exponents are either -0.5 or -1.0 .

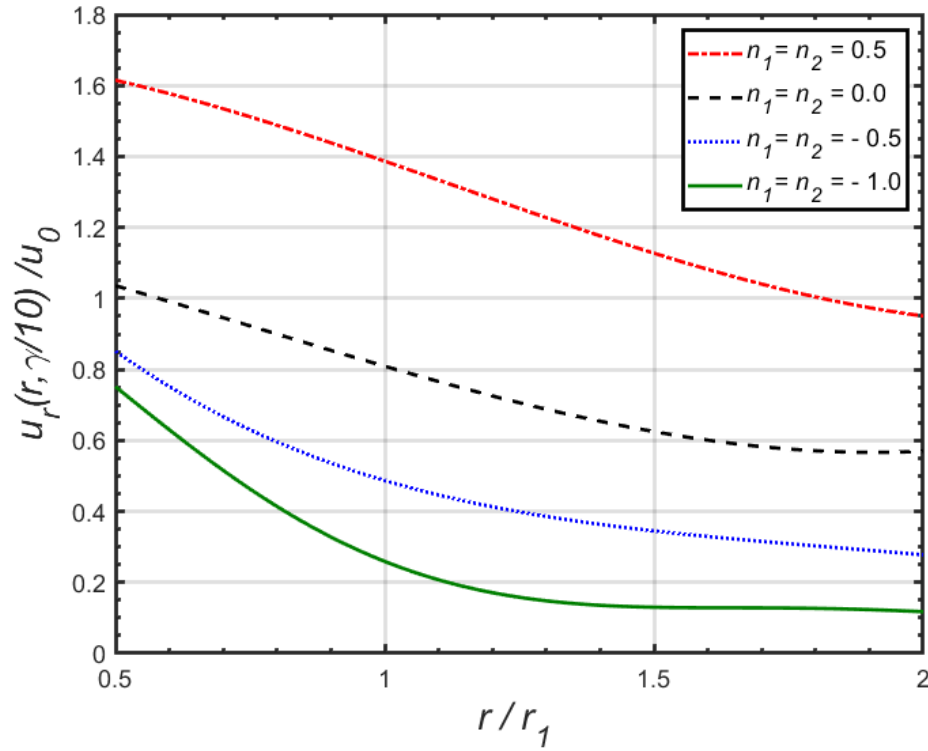


Figure 53: Dimensionless spatial radial displacement computed at $\gamma t = 10$ considering an external FGM coating under internal exponential pressure.

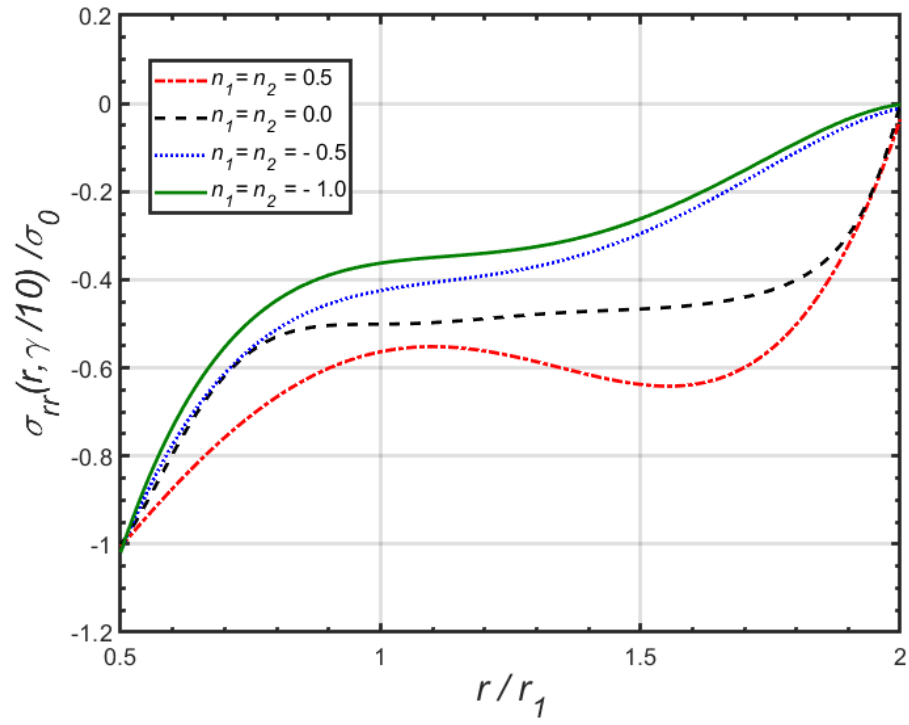


Figure 54: Dimensionless spatial radial stress computed at $\gamma t = 10$ considering an external FGM coating under internal exponential pressure.

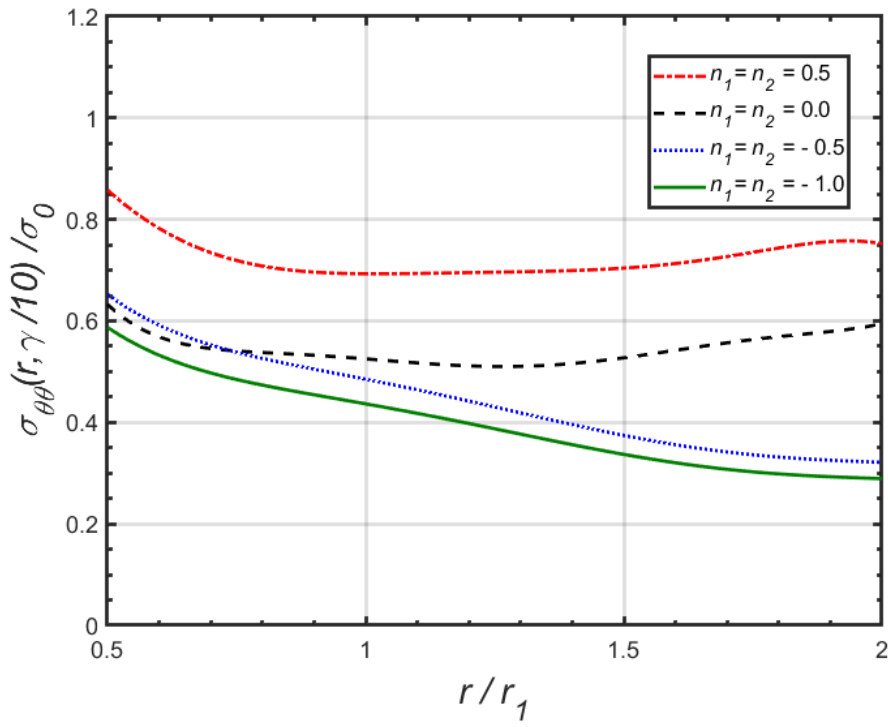


Figure 55: Dimensionless spatial tangential stress computed at $\gamma t = 10$ considering an external FGM coating under internal exponential pressure.

5.5 Annular internal FGM coating thick-walled cylinder in plane strain condition

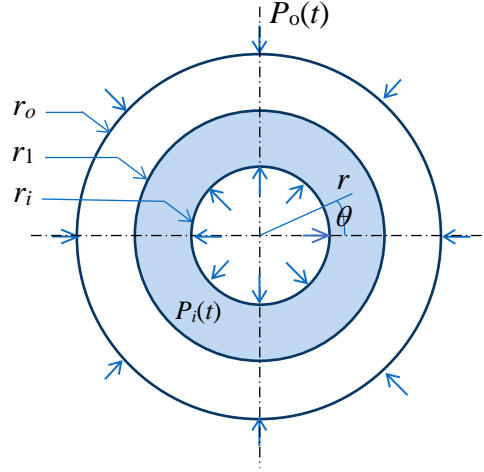


Figure 56: Annular internal FGM thick-walled cylinder under internal pressure.

Another annular coating problem is considered in numerical analyses is that of an internal annular FGM coating ($r_i < r < r_1$) bonded by a homogeneous substrate ($r_1 < r < r_o$) on the external surface, as shown in Figure (56). The FGM internal coating is considered to be subjected to an internal exponential type of pressure shock, in which its mathematical representation is as follows:

$$P_i(t) = P_a (1 - \exp(-\gamma t)), \quad t > 0, \quad (132)$$

Where, P_a is the inner pressure for a large period of time t , and γ is a temporal constant with the unit $1/s$.

The pressure on the outer surface, $P_o(t)$, is considered zero and, material properties of the internal FGM coating and the external homogeneous substrate are varying according to a power law of volume fraction and defined by:

$$E(r) = \begin{cases} E_1 \left(\frac{r}{r_1} \right)^{n_1}, & r_i < r < r_1, \\ E_1, & r_1 < r < r_o, \end{cases} \quad \rho(r) = \begin{cases} \rho_1 \left(\frac{r}{r_1} \right)^{n_2}, & r_i < r < r_1, \\ \rho_1, & r_1 < r < r_o. \end{cases} \quad (133)$$

Since the material properties are continuous at the interface, $r = r_1$; therefore, the same procedure used before for the external annular coating can be used here as well. The composite cylinder is considered in the plane strain state; whereas, the Poisson's ratio is constant and equals to 0.3. The radii are taken as $r_i = 0.05$ m, $r_1 = 0.1$ m, and $r_o = 0.2$ m. However, the formulation and solution procedure described in chapter three, the D-BEM formulation, can be applied to investigate the elastodynamic behavior of the composite cylinder under internal shock pressure, except that instead of ρ_o and E_o variables in the formulation ρ_1 and E_1 are used. Hence, 10 quadratic cells are used to model the internal FGM coating; whereas the number of quadratic cells used to model the outer homogeneous substrate is 20. The time step employed in the time marching of the Houbolt's method is also 1×10^{-5} s. Numerical results for the composite cylinder under the exponential internal dynamic pressure are calculated. The normalized parameters are expressed as:

$$\sigma_0 = P_a, \quad u_0 = \frac{P_a}{E_o} r_o. \quad (134)$$

Moreover, the response of the radial displacement and, the radial and circumferential stresses calculated at the midpoint of wall thickness, $r = (r_i + r_1)/2$, of the internal FGM coating are plotted, as shown in figures (57, 58 and 59), respectively.

The exponents n_1 and n_2 are considered equal. Whereas, a non-dimensional time γt is ranging from 0 to 10. Obviously, for the radial displacement, radial and tangential stresses, their magnitudes become smaller for a decreasing material exponent from 0.5 to -1 . It is also noticed that the oscillations trend of the homogeneous case has a time lag of the other FGM cases, and the radial stress components are compressive.

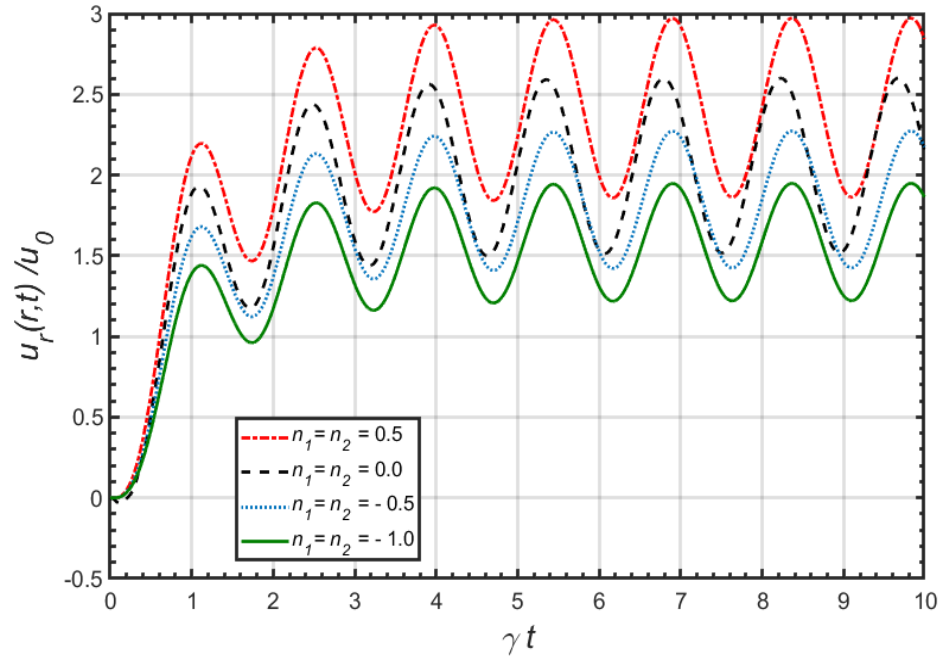


Figure 57: Dimensionless radial displacement at the mid-point, $r = (r_i + r_1)/2$, of the inner FGM coating under internal exponential pressure

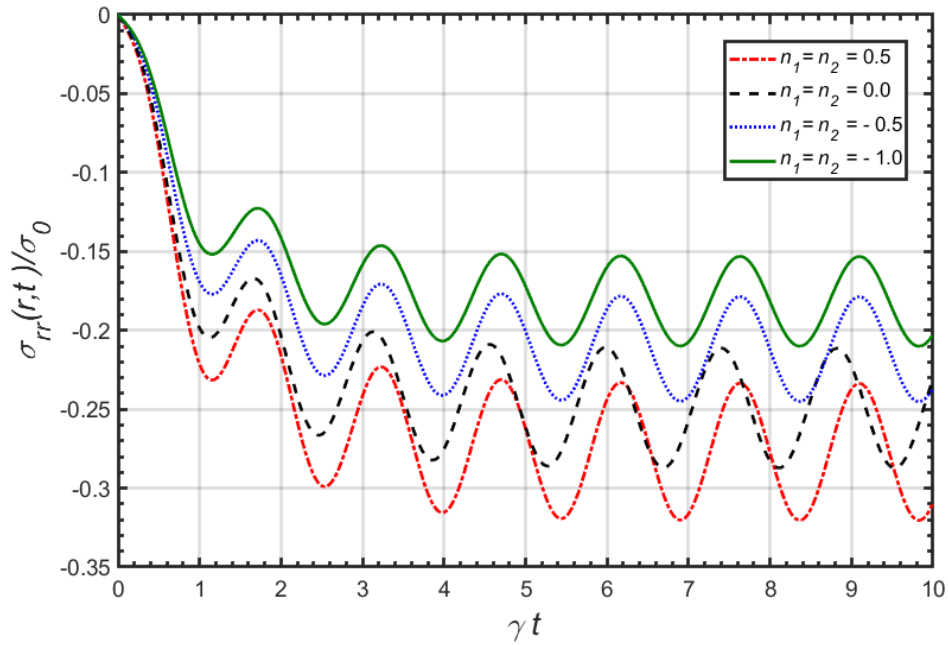


Figure 58: Dimensionless radial stress at the mid-point, $r = (r_i + r_1)/2$, of the inner FGM coating under internal exponential pressure

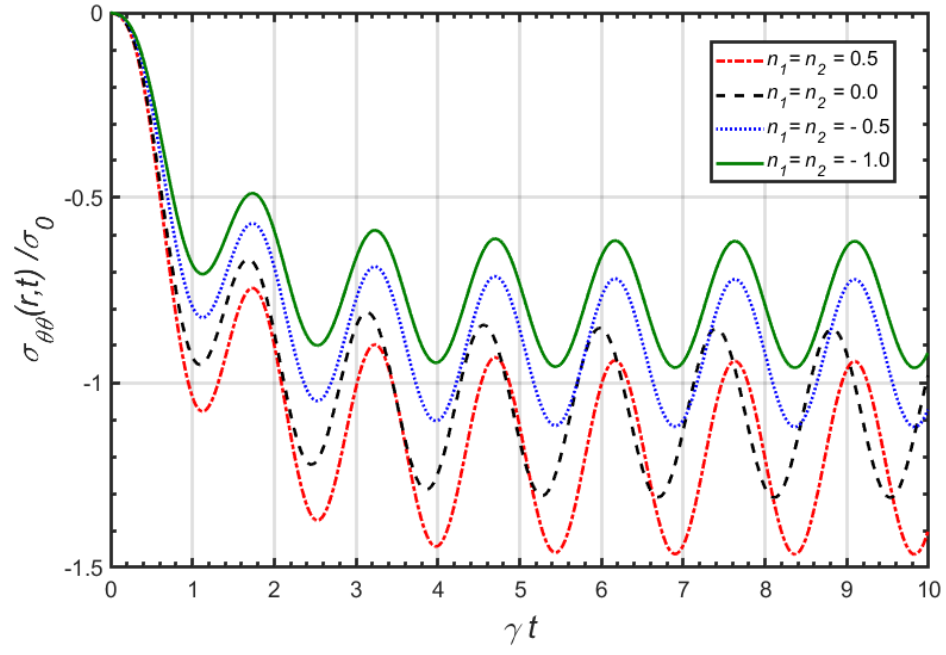


Figure 59: Dimensionless circumferential stress at the mid-point, $r = (r_i + r_1)/2$, of the inner FGM coating under internal exponential pressure

On the other side, Figures (60, 61 and 62) present the oscillations of the radial displacement and, the radial and tangential stress components at the midpoint, $r = (r_1 + r_o)/2$, of the homogeneous outer substrate of the cylinder wall. The time histories are in general similar to the one determined for the midpoint of the FGM inner coating of the cylinder. The magnitudes for the displacement and stress for the outer homogeneous substrate also decrease as the exponents are reduced from 0.5 to -1 .

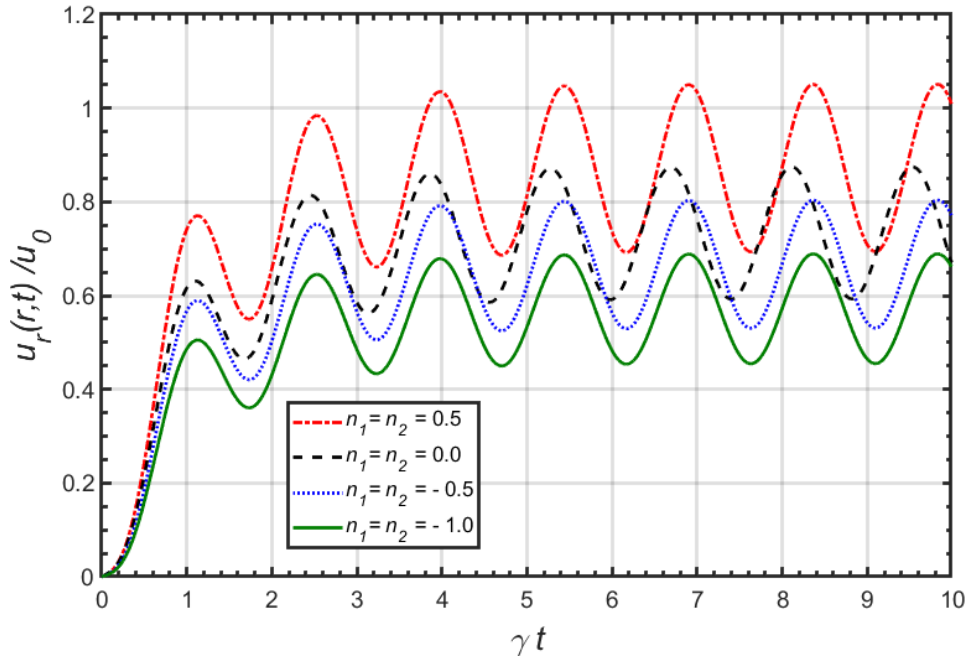


Figure 60: Dimensionless radial displacement at the mid-point, $r = (r_1 + r_o)/2$, of the outer homogeneous substrate under internal exponential pressure

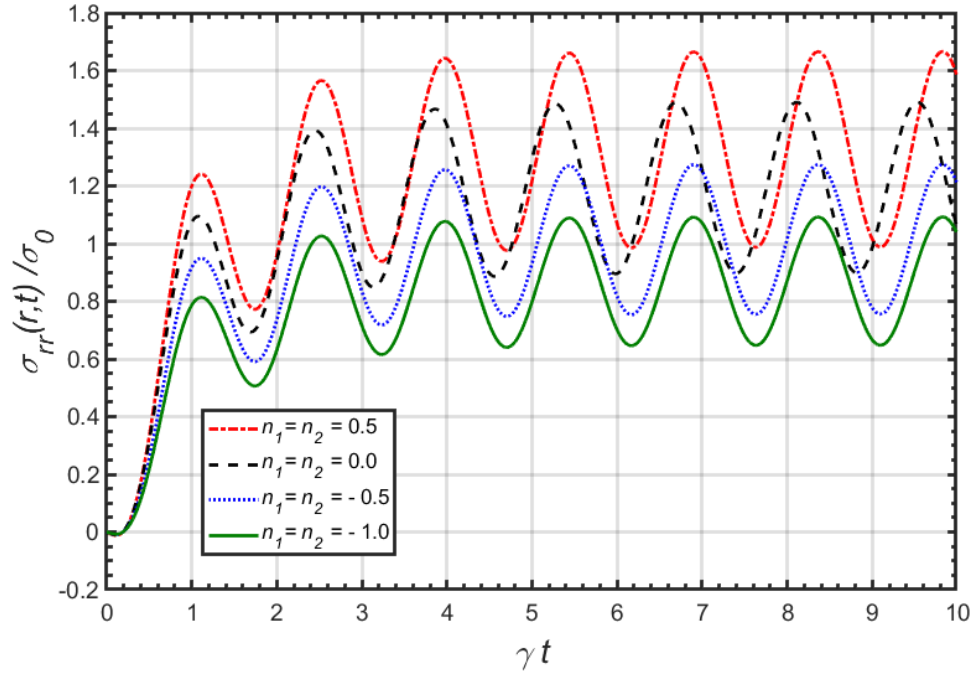


Figure 61: Dimensionless radial stress at the mid-point, $r = (r_1 + r_o)/2$, of the outer homogeneous substrate under internal exponential pressure

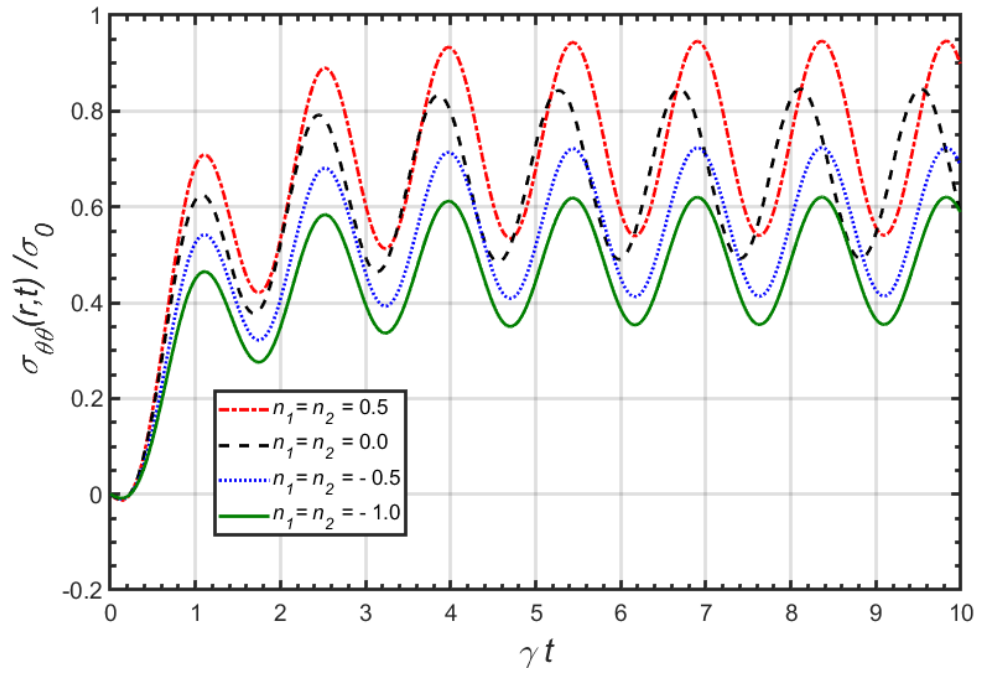


Figure 62: Dimensionless circumferential stress at the mid-point, $r = (r_1 + r_o)/2$, of the outer homogeneous substrate under internal exponential pressure

Furthermore, at a selected non-dimensional temporal point γt equals 10, figures (63, 64 and 65) show the spatial variations of the non-dimensional radial displacement and, radial and hoop stresses. The spatial radial displacements magnitudes are positive, and decrease as the non-dimensional radial coordinate, r/r_1 , is increased from 0.5 to 2.0. However, the radial stress satisfies the stress boundary conditions at the inner and outer edges of the cylinder, and its smallest values are found to be at the material property exponent $n_1 = n_2 = -1$. Moreover, radial and circumferential stresses are mostly negative for the inner coating substrate but, in the homogenous substrate they become positive for all values of the exponents considered.

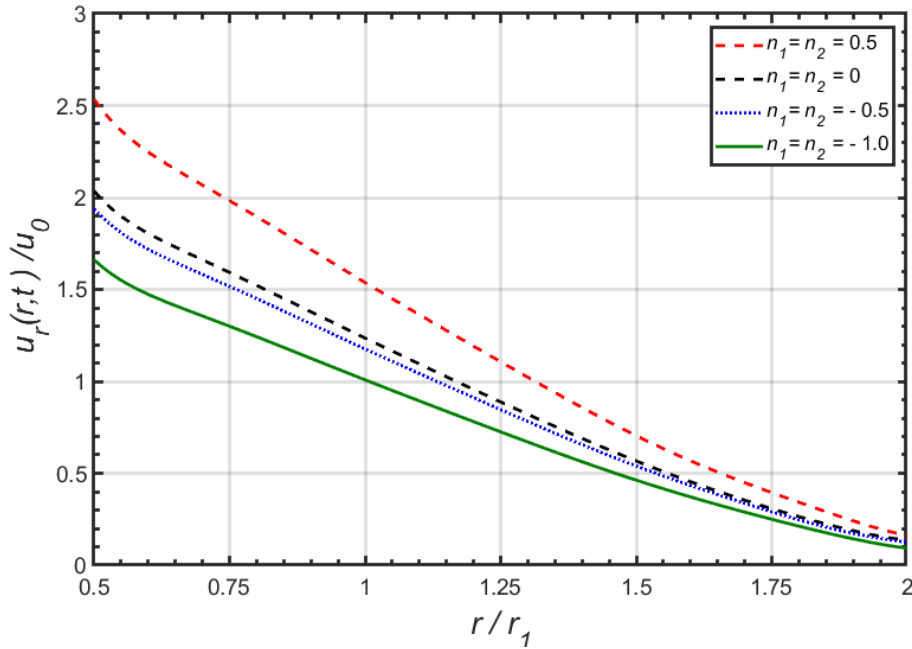


Figure 63: Dimensionless spatial radial displacement computed at $\gamma t = 10$ considering an internal FGM coating under internal exponential pressure.

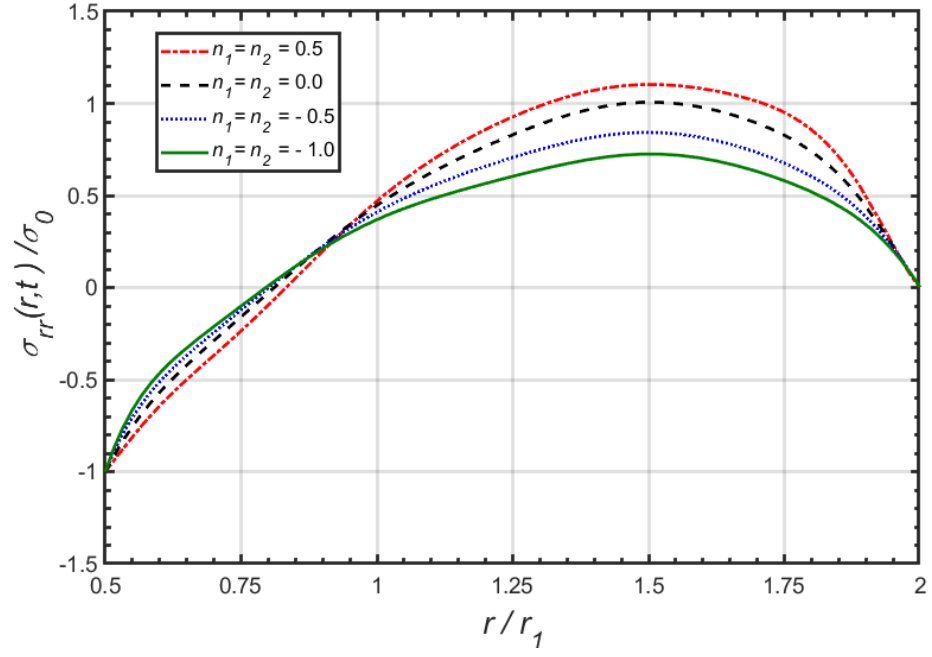


Figure 64: Dimensionless spatial radial stress computed at $\gamma t = 10$ considering an internal FGM coating under internal exponential pressure.

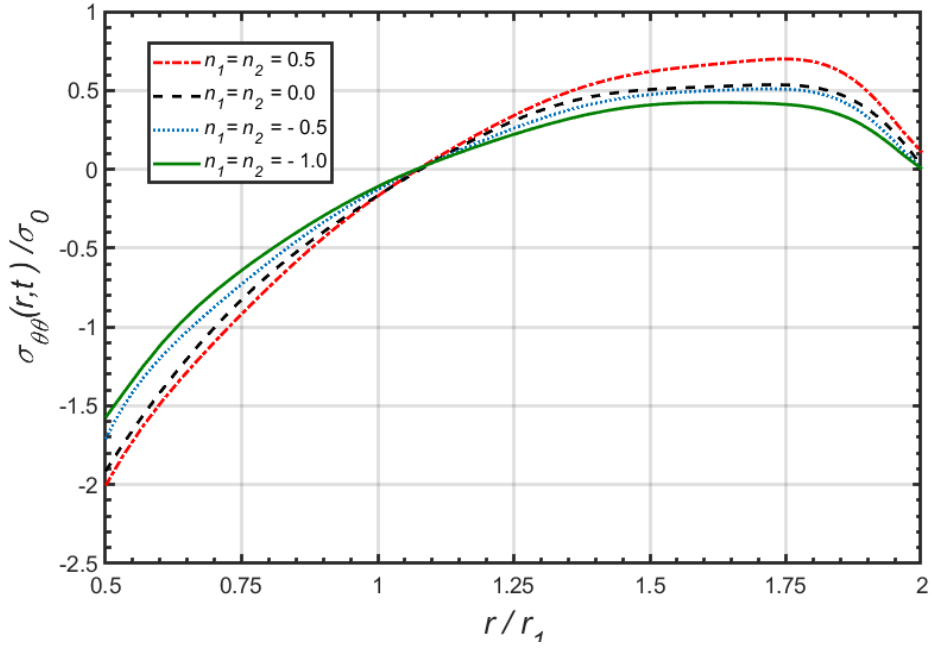


Figure 65: Dimensionless spatial circumferential stress computed at $\gamma t = 10$ considering an internal FGM coating under internal exponential pressure.

CHAPTER 6

CONCLUSIONS

In this research work, the elastodynamic analysis of functionally graded thick-walled cylinders and annular coatings subjected to various types of pressure shocks with different loading conditions is performed by utilizing a new computational technique based on the domain boundary element method. The physical properties except Poisson's ratio, which is considered constant and equal to 0.3, are assumed to be varying in the radial direction along the wall thickness according to a power law. The governing equation of motion is derived in agreement with the plane elastodynamics. The static fundamental solution, not the time dependent solution, is employed as the weight function to write the weighted residual form equation. Subsequently, the mathematical model of the problem is expressed by an integral equation in terms of the radial displacement and the inertia term. Hence, by applying the D-BEM technique, a system of temporal ordinary differential equations is achieved by the domain discretization with quadratic isoparametric elements due to the presence of inertia terms, and displacement domain terms. Houbolt's time marching scheme are employed to solve numerically the obtained temporal system of algebraic equations.

Moreover, the developed procedures are verified by different comparisons performed with the analytical results obtained from the literature, which validate our D-BEM procedure results. Furthermore, plane stress and plane strain states elastodynamic analysis of FGM hollow cylinder, subjected to internal shock loading, is studied to investigate the two states by performing a parametric analysis, in which time histories of radial displacement and stress components in functionally graded and composite thick-walled cylinder, subjected to a ramp type of pressure shock, are illustrated

For a functionally graded thick-walled cylinder subjected to internal or external ramp shock loading, numerical results are generated. These results indicate that the material property exponents n_1 and n_2 have an important effect on the variations of both the

radial displacement and stress components. Furthermore, a reduction in the values of these material property exponents is shown to cause corresponding decrease in the amplitudes of the transient wave of the midpoint radial displacements and stress components. Thus, this further leads to the conclusion that in a FGM cylinder with a fixed physical property values at the outer surface, the transient midpoint radial displacement and, radial and circumferential stresses magnitudes calculated for a decreasing material property index are less than those calculated for higher material property indices. Since the external and internal coatings of pipes has become important in today industries; especially in gas and oil industry. Therefore, other sets of computational results are provided by considering in the first case a composite cylinder consists of an external FGM coating and a homogeneous internal substrate. While in the second case an internal FGM annular coating is considered. In both cases, the loading is taken as exponentially varied type of internal pressure shock. The parametric elastodynamic analysis which is performed, in the case of annular coating, result in a similar trend concerning the impact of power function exponents on transient midpoints of the homogeneous and FGM substrates; as well as the amplitudes of the radial displacement and stress components. Furthermore, the results generated for both the FGM and composite thick-walled cylinders also include the spatial variations of radial displacement and stress components for given points selected in time.

Furthermore, a parametric analysis of the stress concentration related to the tangential stress is studied for the FGM thick-walled cylinder subjected to a ramp type of pressure shock. Three different temporal points and four different material property exponents are used in this investigation and, the maximum stress points and their normalized radial locations are determined. However, the maximum concentration points are found to be either at the inner or the outer surfaces depending on the material property exponents used.

The method used in this research work is general that it permits the modelling of thick-walled composite cylinders consisting of an arbitrary number of functionally graded and homogeneous annuli, and subjected to pressure shocks types of loading on both the inner and outer surfaces of the cylinder. Number of coating annuli, material property functions, and inner and outer pressure shock loading functions can be altered

to perform computations for different configurations. Thus, such analysis by the proposed numerical technique will result in high accuracy numerical results capable of revealing the elastodynamic behavior. Finally, the domain boundary element method presented in this work could be beneficial in the analysis, optimization and, design studies involving functionally graded material and composite thick-walled cylinders under different types of pressure shock loadings.

REFERENCES

1. B. Saleh, J. Jiang, R. Fathi, T. Al-hababi, Q. Xu, L. Wang, D. Song, A. Ma, “30 years of functionally graded materials: an overview of manufacturing methods, applications and future challenges”, *Compos. Part B-Eng.* 201 (2020) 108376, <https://doi.org/10.1016/j.compositesb.2020.108376>.
2. A. Pasha, B.M. Rajaprakash, “Fabrication and mechanical properties of functionally graded materials: a review”, *Mater. Today-Proc.* 52 (2022) 379–387, <https://doi.org/10.1016/j.matpr.2021.09.066>.
3. Y.A.C. Jande, M. Erdal, S. Dag, “Production of graded porous polyamide structures and polyamide-epoxy composites via selective laser sintering”, *J. Reinf. Plast. Comp.* 33 (2014) 1017–1036, <https://doi.org/10.1177/0731684414522536>.
4. S.C. Ram, K. Chattopadhyay, I. Chakrabarty, “High temperature tensile properties of centrifugally cast in-situ Al-Mg₂Si functionally graded composites for automotive block liners”, *J. Alloy. Compd.* 724 (2017) 84–97, <https://doi.org/10.1016/j.jallcom.2017.06.306>.
5. X. Miao, D. Sun, “Graded/gradient porous biomaterials”, *Materials* 3 (2010) 26–47, <https://doi.org/10.3390/ma3010026>.
6. D.J. Yang, Z.F. Yuan, P.H. Lee, H.M. Yin, “Simulation and experimental validation of heat transfer in a novel hybrid solar panel”, *Int. J. Heat Mass Tran.* 55 (2012) 1076–1082, <https://doi.org/10.1016/j.ijheatmasstransfer.2011.10.003>.
7. A. Zenkour “Analytical Solutions for Rotating Exponentially-Graded Annular Disks with Various Boundary Conditions”, *International Journal of Structural Stability and Dynamics*, 5(4), 557-577 (2005).
8. L. Xin, G. Dui, S. Yang, J. Zhang, “An elasticity solution for functionally graded thick-walled tube subjected to internal pressure”, *International Journal of Mechanical Sciences* 89 (2014) 344–349, <https://doi.org/10.1016/j.ijmecsci.2014.08.028>.

9. L. Xin, S. Yang, D. Zhou, G. Dui, “*An approximate analytical solution based on the Mori-Tanaka method for functionally graded thick-walled tube subjected to internal pressure*”, *Composite Structures* 135 (2016) 74–82, <https://doi.org/10.1016/j.compstruct.2015.08.104>.
10. H. Li, Y. Liu, “*Functionally graded hollow cylinders with arbitrary varying material properties under nonaxisymmetric loads*”, *Mechanics Research Communications* 55 (2014) 1–9, <https://doi.org/10.1016/j.mechrescom.2013.10.011>.
11. R. Sburlati, “*Analytical elastic solutions for pressurized hollow cylinders with internal functionally graded coatings*”, *Composite Structures* 94 (2012) 3592–3600, <https://doi.org/10.1016/j.compstruct.2012.05.018>.
12. Y.Z. Chen, “*A novel numerical solution for a functionally graded hollow cylinder with arbitrary elastic property along the radial direction*”, *International Journal of Pressure Vessels and Piping* 191 (2021) 104301, <https://doi.org/10.1016/j.ijpvp.2021.104301>.
13. H.-L. Dai, T. Dai, H.Y. Zheng, “*Stress distributions in a rotating functionally graded piezoelectric hollow cylinder*”, *Meccanica* 47 (2012) 423–436, <https://doi.org/10.1007/s11012-011-9447-8>.
14. Z.S. Shao, G.W. Ma, “*Thermo-mechanical stresses in functionally graded circular hollow cylinder with linearly increasing boundary temperature*”, *Composite Structures* 83 (2008) 259–265, <https://doi.org/10.1016/j.compstruct.2007.04.011>.
15. M. Jabbari, S. Sohrabpour, M.R. Eslami, “*Mechanical and thermal stresses in a functionally graded hollow cylinder due to radially symmetric loads*”, *International Journal of Pressure Vessels and Piping* 79 (2002) 493–497, [https://doi.org/10.1016/S0308-0161\(02\)00043-1](https://doi.org/10.1016/S0308-0161(02)00043-1).
16. Z.S. Shao, “*Mechanical and thermal stresses of a functionally graded circular hollow cylinder with finite length*”, *International Journal of Pressure Vessels and Piping* 82 (2005) 155–163, <https://doi.org/10.1016/j.ijpvp.2004.09.007>.
17. X.L. Peng, X.F. Li, “*Thermoelastic analysis of a cylindrical vessel of functionally graded materials*”, *International Journal of Pressure Vessels and Piping* 87 (2010) 203–210, <https://doi.org/10.1016/j.ijpvp.2010.03.024>.

18. V.R. Manthena, G.D. Kedar, “*Transient thermal stress analysis of a functionally graded thick hollow cylinder with temperature-dependent material properties*”, *Journal of Thermal Stresses* 41 (2018) 568–582, <https://doi.org/10.1080/01495739.2017.1402669>.
19. I. Eshraghi, N. Soltani, S. Dag, “*Weight function method for transient thermomechanical fracture analysis of a functionally graded hollow cylinder possessing a circumferential crack*”, *Journal of Thermal Stresses* 39 (2016) 1182–1199, <https://doi.org/10.1080/01495739.2016.1215711>.
20. I. Eshraghi, N. Soltani, S. Dag, “*Hyperbolic heat conduction based weight function method for thermal fracture of functionally graded hollow cylinders*”, *International Journal of Pressure Vessels and Piping* 165 (2018) 249–262, <https://doi.org/10.1016/j.ijpvp.2018.07.008>.
21. M.R. Nami, H. Eskandari, “*Three-dimensional investigations of stress intensity factors in a thermo-mechanically loaded cracked FGM hollow cylinder*”, *International Journal of Pressure Vessels and Piping* 89 (2012) 222–229, <https://doi.org/10.1016/j.ijpvp.2011.11.004>.
22. P. Farahpour, V. Babaghasabha, M. Khadem, “*Stress intensity factor calculation for semi-elliptical cracks on functionally graded material coated cylinders*”, *Structural Engineering and Mechanics* 55 (2015) 1087–1097, <http://dx.doi.org/10.12989/sem.2015.55.6.1087>.
23. J.W. Fu, Z.T. Chen, L.F. Qian, “*Coupled thermoelastic analysis of a multi-layered hollow cylinder based on the C-T theory and its application on functionally graded materials*”, *Composite Structures* 131 (2015) 139–150, <https://doi.org/10.1016/j.compstruct.2015.04.053>.
24. M. Nikkhah, F. Honarvar, E. Dehghan, “*Elastodynamic solution for plane strain response of functionally graded thick hollow cylinders by analytical method*”, *Applied Mathematics and Mechanics (English Edition)* 32 (2011) 189–202, <https://dx.doi.org/10.1007/s10483-011-1405-9>.
25. S. Baba, I. Keles, “*A novel approach to forced vibration behavior of thick-walled cylinders*”, *International Journal of Pressure Vessels and Piping* 137 (2016) 22–27, <http://dx.doi.org/10.1016/j.ijpvp.2015.04.015>.

26. N. Zhang, Y. Zhang, D. Dai, “*Dynamic response of a functionally graded cylindrical tube with power-law varying properties due to SH-waves*”, *Waves in Random and Complex Media*, in press,
<https://doi.org/10.1080/17455030.2021.1948628>.
27. S.M. Hosseini, J. Sladek, V. Sladek, “*Meshless local Petrov-Galerkin method for coupled thermoelasticity analysis of a functionally graded thick hollow cylinder*”, *Engineering Analysis with Boundary Elements* 35 (2011) 827–835,
<https://doi.org/10.1016/j.enganabound.2011.02.001>.
28. M. Dorduncu, M.K. Apalak, H.P. Cherukuri, “*Elastic wave propagation in functionally graded circular cylinders*”, *Composites: Part B* 73 (2015) 35–48,
<http://dx.doi.org/10.1016/j.compositesb.2014.12.021>.
29. A. Sayyidmousavi, M. Foroutan, Z. Fawaz, “*Dynamic response and optimization of functionally graded porous nanocomposite cylinders using a meshfree method*”, *Polymer Composites* 42 (2021) 4227–4238,
<http://doi.org/10.1002/pc.26141>.
30. C. Xu, Z.-X. Yu, F. Du, “*Dynamic analysis of a thick hollow cylinder made of two-dimensional functionally graded material using time domain spectral element method*”, *Mechanics of Advanced Materials and Structures* 26 (2019) 1518–1535, <https://doi.org/10.1080/15376494.2018.1444224>.
31. M. Shakeri, M. Akhlaghi, S.M. Hoseini, “*Vibration and radial wave propagation velocity in functionally graded thick hollow cylinder*”, *Composite Structures* 76 (2006) 174–181,
<https://doi.org/10.1016/j.compstruct.2006.06.022>.
32. K. Asemi, M. Akhlaghi, M. Salehi, “*Dynamic analysis of thick short length FGM cylinders*”, *Meccanica* 47 (2012) 1441–1453,
<https://doi.org/10.1007/s11012-011-9527-9>.
33. F. Shahabian, S.M. Hosseini, “*Stochastic dynamic analysis of a functionally graded thick hollow cylinder with uncertain material properties subjected to shock loading*”, *Materials and Design* 31 (2010) 894–901.
<https://doi.org/10.1016/j.matdes.2009.07.040>.
34. V. Vullo, and F. Vivio, “*Rotors: Stress Analysis and Design*”, 1st Ed., Springer-Verlag, Italy, 2013.

35. A. Zenkour “*Analytical Solutions for Rotating Exponentially-Graded Annular Disks with Various Boundary Conditions*”, International Journal of Structural Stability and Dynamics, 5(4), 557-577 (2005).
36. H. Callioglu, N. Bektas and M. Sayer “*Stress Analysis of Functionally Graded Rotating Discs: Analytical and Numerical Solutions*”, Acta Mech. Sin., 27(6), 950-955 (2011).
37. A. Eraslan and E. Arslan “*Analytical and Numerical Solutions to a Rotating FGM Disk*”, Journal of Multidisciplinary Engineering Science and Technology, 2(10), 2843-2850 (2015).
38. V. Yildirim “*Analytic Solutions to Power-Law Graded Hyperbolic Rotating Discs Subjected to Different Boundary Conditions*”, International Journal Of Engineering & Applied Sciences, 8(1), 38-52 (2016).
39. Zheng et al. “*Stress Analysis in Functionally Graded Rotating Disks with Non-Uniform Thickness and Variable Angular Velocity*”, International Journal of Mechanical Sciences, 119, 283-293 (2016).
40. Costabel et al. “*Time-dependent problems with the boundary integral equation method*”, Encyclopedia of computational mechanics. NJ: John Wiley; 703-721 (2004).
41. Becker.A. “*The Boundary Element Method in Engineering: A Complete Course*”, McGraw Hill International Limited, UK, 1992.
42. Nardini D, Brebbia C. “*New approach to free vibration analysis using boundary elements*”, In: Brebbia CA, editor. Boundary element methods in engineering. Southampton and Boston: Springer-Verlag, Berlin and Computational Mechanics Publications; 312-326 (1982).
43. Katsikadelis J. “*The Boundary Element Method for Engineers and Scientists: Theory and Applications*”, 2nd Ed., UK, 2016.
44. G.D. Hatzigeorgiou, D.E. Beskos, “*Dynamic elastoplastic analysis of 3-D structures by the domain/boundary element method*”, Computers & Structures 80 (2002) 339–347.
[https://doi.org/10.1016/S0045-7949\(01\)00176-6](https://doi.org/10.1016/S0045-7949(01)00176-6).

45. G.D. Hatzigeorgiou, D.E. Beskos, “*Transient dynamic response of 3-D elastoplastic structures by the D/BEM*”, in: D.E. Beskos, C.A. Brebbia (Eds.), Transactions on Modelling and Simulation, Boundary Elements XXIII, Vol. 28, 2001, pp. 129–137.
<https://www.witpress.com/Secure/elibrary/papers/BE01/BE01011FU.pdf>.
46. J.A.M. Carrer, W.J. Mansur, “*Alternative time-marching schemes for elastodynamic analysis with the domain boundary element method formulation*”, Computational Mechanics 34 (2004) 387–399.
<https://doi.org/10.1007/s00466-004-0582-0>.
47. J.A.M. Carrer, S.A. Fleischfresser, L.F.T. Garcia, W.J. Mansur, “*Dynamic analysis of Timoshenko beams by the boundary element method*”, Engineering Analysis with Boundary Elements 37 (2013) 1602–1616.
<https://doi.org/10.1016/j.enganabound.2013.08.007>.
48. J.A.M. Carrer, R.M. Corrêa, W.J. Mansur, R.F. Scuciato, “*Dynamic analysis of continuous beams by the boundary element method*”, Engineering Analysis with Boundary Elements 104 (2019) 80–93.
<https://doi.org/10.1016/j.enganabound.2019.03.015>.
49. I. Eshraghi, S. Dag, “*Domain-boundary element method for elastodynamics of functionally graded Timoshenko beams*”, Computers & Structures 195 (2018) 113–125.
<https://doi.org/10.1016/j.compstruc.2017.10.007>
50. Eshraghi, S. Dag, “*Forced vibrations of functionally graded annular and circular plates by domain-boundary element method*”, Z. Angew. Math. Mech. 100 (2020) e201900048.
<https://doi.org/10.1002/zamm.201900048>.
51. Z. Ahmed, I. Eshraghi, S. Dag, “*Domain-boundary element method for forced vibrations of fiber-reinforced laminated beams*”, International Journal for Computational Methods in Engineering Science and Mechanics 21 (2020) 141–158.
<https://doi.org/10.1080/15502287.2020.1772905>.

52. I. Eshraghi, S. Dag, “*Transient dynamic analysis of functionally graded micro-beams considering small-scale effects*”, Arch. Mech. 73 (2021) 303–337.
<https://doi.org/10.24423/aom.3786>.
53. A. Kurusn, M. Topcu and T. Tetik “*Stress Analysis of Functionally Graded Disc under Thermal and Mechanical Loads*”, Procedia Engineering, 10, 2949-2954 (2011).
54. N. Bektas and M. Akca “*Stress Analysis of Functionally Graded Discs under Mechanical and Thermal Loads: Analytical and Numerical Solutions*”, Sci Eng Compos Mater, 19(4), 361-371 (2012).
55. Y. Ootao and Y. Tanigawa “*Transient Thermoelastic Analysis for a Multilayered Hollow Circular Disk with Piecewise Power Law Nonhomogeneity*”, Journal of Thermal Stresses, 35, 75-90 (2012).
56. A. Bagri and M. Eslami “*Generalized Coupled Thermoelasticity of Functionally Graded Annular Disk Considering Lord-Shulman Theory*”, Composite Structures, 83, 168-179 (2008).
57. I. Keles, N. Tutuncu, “*Exact analysis of axisymmetric dynamic response of functionally graded cylinders or (disks) and spheres*”, Journal of Applied Mechanics: ASME 78 (2011).

APPENDIX

The entries of the matrix \mathbf{S}^{ij} are defined as follows:

$$h_1^{kj} = h_{1A}^{kj} - h_{1B}^{kj}, \quad (135)$$

$$h_2^{kj} = h_{2B}^{kj} - h_{2A}^{kj}, \quad (136)$$

$$h_3^{kj} = h_{3A}^{kj} - h_{3B}^{kj}, \quad (137)$$

$$h_{1A}^{kj} = \frac{\xi_k^{1-a_2}}{2a_1 l^2} \left(\frac{r^{\bar{n}+a_2+3}}{\bar{n}+a_2+3} - \frac{r^{\bar{n}+a_2+2} (r_2^j + r_3^j)}{\bar{n}+a_2+2} + \frac{r^{\bar{n}+a_2+1} r_2^j r_3^j}{\bar{n}+a_2+1} \right) \bigg|_{r_1^j}^{r_3^j}, \quad (138)$$

$$h_{1B}^{kj} = \frac{\xi_k^{1-a_3}}{2a_1 l^2} \left(\frac{r^{\bar{n}+a_3+3}}{\bar{n}+a_3+3} - \frac{r^{\bar{n}+a_3+2} (r_2^j + r_3^j)}{\bar{n}+a_3+2} + \frac{r^{\bar{n}+a_3+1} r_2^j r_3^j}{\bar{n}+a_3+1} \right) \bigg|_{r_1^j}^{r_3^j}, \quad (139)$$

$$h_{2A}^{kj} = \frac{\xi_k^{1-a_2}}{a_1 l^2} \left(\frac{r^{\bar{n}+a_2+3}}{\bar{n}+a_2+3} - \frac{r^{\bar{n}+a_2+2} (r_1^j + r_3^j)}{\bar{n}+a_2+2} + \frac{r^{\bar{n}+a_2+1} r_1^j r_3^j}{\bar{n}+a_2+1} \right) \bigg|_{r_1^j}^{r_3^j}, \quad (140)$$

$$h_{2B}^{kj} = \frac{\xi_k^{1-a_3}}{a_1 l^2} \left(\frac{r^{\bar{n}+a_3+3}}{\bar{n}+a_3+3} - \frac{r^{\bar{n}+a_3+2} (r_1^j + r_3^j)}{\bar{n}+a_3+2} + \frac{r^{\bar{n}+a_3+1} r_1^j r_3^j}{\bar{n}+a_3+1} \right) \bigg|_{r_1^j}^{r_3^j}, \quad (141)$$

$$h_{3A}^{kj} = \frac{\xi_k^{1-a_2}}{2a_1 l^2} \left(\frac{r^{\bar{n}+a_2+3}}{\bar{n}+a_2+3} - \frac{r^{\bar{n}+a_2+2} (r_1^j + r_2^j)}{\bar{n}+a_2+2} + \frac{r^{\bar{n}+a_2+1} r_1^j r_2^j}{\bar{n}+a_2+1} \right) \bigg|_{r_1^j}^{r_3^j}, \quad (142)$$

$$h_{3B}^{kj} = \frac{\xi_k^{1-a_3}}{2a_1 l^2} \left(\frac{r^{\bar{n}+a_3+3}}{\bar{n}+a_3+3} - \frac{r^{\bar{n}+a_3+2} (r_1^j + r_2^j)}{\bar{n}+a_3+2} + \frac{r^{\bar{n}+a_3+1} r_1^j r_2^j}{\bar{n}+a_3+1} \right) \bigg|_{r_1^j}^{r_3^j}, \quad (143)$$

$$\bar{n} = n_2 - n_1, \quad (144)$$

$$a_2 = \frac{-n_1 + a_1}{2}, \quad (145)$$

$$a_3 = \frac{-n_1 - a_1}{2}. \quad (146)$$

The terms in the entries of the matrices \mathbf{G}^{ij} are of the forms

$$m_1^{kj} = m_{1A}^{kj} - m_{1B}^{kj}, \quad (147)$$

$$m_2^{kj} = m_{2B}^{kj} - m_{2A}^{kj}, \quad (148)$$

$$m_3^{kj} = m_{3A}^{kj} - m_{3B}^{kj}, \quad (149)$$

$$b_1^{kj} = a_2 m_{1A}^{kj} - a_3 m_{1B}^{kj}, \quad (150)$$

$$b_2^{kj} = a_3 m_{2B}^{kj} - a_2 m_{2A}^{kj}, \quad (151)$$

$$b_3^{kj} = a_2 m_{3A}^{kj} - a_3 m_{3B}^{kj}, \quad (152)$$

$$m_{1A}^{kj} = \frac{\xi_k^{1-a_2}}{2a_1 l^2} \left(\frac{r^{a_2+1}}{a_2+1} - \frac{r^{a_2} (r_2^j + r_3^j)}{a_2} + \frac{r^{a_2-1} r_2^j r_3^j}{a_2-1} \right) \bigg|_{r_1^j}^{r_3^j}, \quad (153)$$

$$m_{1B}^{kj} = \frac{\xi_k^{1-a_3}}{2a_1 l^2} \left(\frac{r^{a_3+1}}{a_3+1} - \frac{r^{a_3} (r_2^j + r_3^j)}{a_3} + \frac{r^{a_3-1} r_2^j r_3^j}{a_3-1} \right) \bigg|_{r_1^j}^{r_3^j}, \quad (154)$$

$$m_{2A}^{kj} = \frac{\xi_k^{1-a_2}}{a_1 l^2} \left(\frac{r^{a_2+1}}{a_2+1} - \frac{r^{a_2} (r_1^j + r_3^j)}{a_2} + \frac{r^{a_2-1} r_1^j r_3^j}{a_2-1} \right) \bigg|_{r_1^j}^{r_3^j}, \quad (155)$$

$$m_{2B}^{kj} = \frac{\xi_k^{1-a_3}}{a_1 l^2} \left(\frac{r^{a_3+1}}{a_3+1} - \frac{r^{a_3} (r_1^j + r_3^j)}{a_3} + \frac{r^{a_3-1} r_1^j r_3^j}{a_3-1} \right) \bigg|_{r_1^j}^{r_3^j}, \quad (156)$$

$$m_{3A}^{kj} = \frac{\xi_k^{1-a_2}}{2a_1 l^2} \left(\frac{r^{a_2+1}}{a_2+1} - \frac{r^{a_2} (r_1^j + r_2^j)}{a_2} + \frac{r^{a_2-1} r_1^j r_2^j}{a_2-1} \right) \bigg|_{r_1^j}^{r_3^j}, \quad (157)$$

$$m_{3B}^{kj} = \frac{\xi_k^{1-a_3}}{2a_1 l^2} \left(\frac{r^{a_3+1}}{a_3+1} - \frac{r^{a_3} (r_1^j + r_2^j)}{a_3} + \frac{r^{a_3-1} r_1^j r_2^j}{a_3-1} \right) \Bigg|_{r_1^j}^{r_3^j}. \quad (158)$$

CURRICULUM VITAE

Surname, Name: Abeidi, Abdelrahim

EDUCATION

Degree	Institution	Year of Graduation
MSc	Polytechnic of Turin	2006
MEng	Garyounis University	1994
BSc	Garyuonis University	1992
High School	Shuhadaa Yanayer	1987

FOREIGN LANGUAGES

Arabic - Native

English – Professional

Italian – Full professional

Turkish – Limited working proficiency

PUBLICATIONS

Serkan Dag, Abdelrahim Abeidi, *“Computational Elastodynamics of Functionally Graded Thick-Walled Cylinders and Annular Coatings Subjected to Pressure Shocks”*, International Journal of pressure Vessels and Piping. Oct 10, 2022.

N. Bosso, Antonio Gugliotta, Abdelrahim Abeidi, *“Influence of Vehicle Dynamics on Wear of Railway Wheel Profiles”*, International Journal of Applied Engineering, Jun 1, 2018.

N. Bosso, Antonio Gugliotta, Abdelrahim Abeidi, *“Effect of Vehicle Dynamics on Wear Simulation of Railway Wheel Profiles”*, Current Problems in Rail Vehicles / Prorail 2007, Oct 19, 2007.

Aurelio Soma, N. Bosso, A. Gugliotta, Abdelrahim Abeidi, *“Numerical Simulation of Wear in Railway Wheel Profiles”*, Dynamic Systems and Controls, Symposium on Design and Analysis of Advanced Structures, and Tribology / ASME, Jul 7, 2006.

HOBBIES

Reading and Swimming